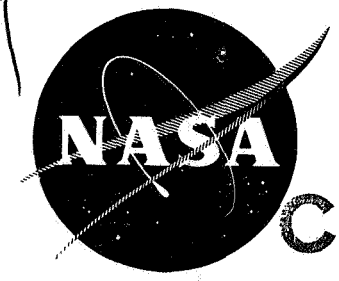

NASA CR-72537
SRI PROJECT PMD 7359

MECHANISMS AND KINETICS OF NICKEL CHROMITE AND COBALT CHROMITE SPINEL FORMATION

by

J. S. ARMIJO

Approved by: D. L. DOUGLASS, PROJECT LEADER

STANFORD RESEARCH INSTITUTE

Prepared for

NATIONAL AERONAUTICS AND SPACE ADMINISTRATION

NASA Lewis Research Center
Contract NAS 3-11165
Fredric H. Harf, Project Manager
Carl E. Lowell, Research Advisor

NOTICE

This report was prepared as an account of Government-sponsored work. Neither the United States, nor the National Aeronautics and Space Administration (NASA), nor any person acting on behalf of NASA:

A. Makes any warranty or representation, expressed or implied, with respect to the accuracy, completeness, or usefulness of the information contained in this report, or that the use of any information, apparatus, method, or process disclosed in this report may not infringe privately-owned rights; or

B. Assumes any liabilities with respect to the use of, or for damages resulting from the use of, any information, apparatus, method or process disclosed in this report.

As used above, "person acting on behalf of NASA" includes any employee of such contractor, to the extent that such employee or contract of NASA or employee of such contractor prepares, disseminates, or provides access to any information pursuant to his employment or contract with NASA, or his employment with such contractor.

Requests for copies of this report should be referred to:

National Aeronautics and Space Administration
Scientific and Technical Information Facility
P. O. Box 33
College Park, Maryland 20740

NASA CR-72537
SRI PROJECT PMD 7359

Final Report: Task 2

MECHANISMS AND KINETICS OF NICKEL CHROMITE AND COBALT CHROMITE SPINEL FORMATION

by

J. S. ARMIJO

Approved by: D. L. DOUGLASS, PROJECT LEADER

STANFORD RESEARCH INSTITUTE
Menlo Park, California 94025

Prepared for

NATIONAL AERONAUTICS AND SPACE ADMINISTRATION

May 1969

CONTRACT NAS 3-11165

NASA Lewis Research Center
Cleveland, Ohio

Fredric H. Harf, Project Manager
Carl E. Lowell, Research Advisor
Materials and Structures Division

ABSTRACT

The mechanisms and kinetics of nickel chromite and cobalt chromite formation were studied using dense polycrystals and single crystals of NiO, CoO, and Cr_2O_3. The influence of time, temperature, oxide purity and oxide structure on spinel structures and formation rates were determined. Experiments were performed by reacting pure Cr_2O_3 pellets with pure, manganese-doped, and silicon-doped pellets of NiO and CoO. All reactions were done in air for times ranging from 24 to 640 hours, and at temperatures from 1200 to 1500^{o}C.

ACKNOWLEDGMENTS

The author wishes to express his sincere appreciation to the following persons who contributed to the successful completion of this study:

Dr. D. L. Douglass for his encouragement and many valuable contributions;

Drs. Milton A. Volpe of the Argonne National Laboratory and Charles Sahaghian of the Air Force Cambridge Research Laboratories for their generous donations of oxide single crystals;

Mr. Dante Petro for his able metallographic assistance.

The financial support of the National Aeronautics and Space Administration's Contracts NASr-49(28) and NAS 3-11165, is gratefully acknowledged.

TABLE OF CONTENTS

LIST OF ILLUSTRATIONS

LIST OF TABLES

SUMMARY

The following effects were observed in both nickel chromite and cobalt chromite studies. Thin inert markers that were initially at the NiO, CoO/Cr_2O_3 interface were found buried in the NiO, CoO after the reaction. Precipitation of $NiCr_2O_4$ in CoO was observed on both sides of the buried markers. These effects are the result of chromium dissolution in the monoxides at the reaction temperature and precipitation on subsequent cooling. It was concluded that the markers remain stationary during the reactions, and that the spinel layers migrate toward the Cr_2O_3 half of the reaction couple by a mechanism of countercurrent diffusion of Ni^{2+}, Co^{2+}, and Cr^{3+} in NiO, CoO.

The rates of nickel chromite formation in dense, crack-free specimens are two orders of magnitude smaller than the rates of formation in porous specimens, or at surfaces of dense specimens. These solid state reaction rates are controlled by the rate of chromium dissolution in the nickel oxide, while the surface reaction rates are controlled by a combination of vapor transport of reactants and oxygen, and diffusion of Ni^{2+} and Cr^{3+} through the spinel. When chromium oxide dissolution is accounted for (analytically), the mechanism of solid state spinel formation is found to be countercurrent diffusion of Ni^{2+} and Cr^{3+} through the spinel layer. This mechanism was confirmed when a chromium saturated nickel oxide pellet was reacted with chromium oxide, and the platinum marker was found buried in the spinel.

The rates of cobalt chromite formation is dense, crack-free specimens and at specimen surfaces are identical. If dissolution effects are accounted for analytically, the markers are found to be at the $CoO/CoCr_2O_4$ interface. This marker position confirms the unidirectional diffusion of Co^{2+} and O^{2-} through the spinel layer as the reaction mechanism.

All measured rates were found to agree well with theoretical rates calculated from the Wagner-Schmalzried model and available thermodynamic and kinetic data. It was concluded, however, that these agreements must be viewed with caution because of variability in diffusion data.

Additions of manganese or silicon impurities to NiO do not affect the rates of nickel chromite growth, although manganese enrichment of the chromite layer is observed with Mn-doped specimens, and formation of two-phase $NiCr_2O_4$ + Cr_2O_3 reaction layers is observed with Si-doped specimens. Additions of manganese to CoO reduce the rates of cobalt chromite formation, while additions of silicon increase the rates. The slower spinel formation rates with manganese-doped CoO is tentatively attributed to higher rates of chromium dissolution in the cobalt oxide, or slower rates of cobalt diffusion through the spinel. The accelerated rate of cobalt chromite formation from Si-doped cobalt oxide is attributed to counter-current diffusion of Co^{2+} and Cr^{3+} through a continuous Co_2SiO_4 phase to form large $CoCr_2O_4$ crystals in the reaction layer.

I INTRODUCTION

Spinels are a class of ionic compounds formed from strongly electro-positive metal ions and strongly electronegative nonmetal ions. These compounds commonly exist as oxides, sulfides, or iodides, are distinguished from other ionic compounds by their crystallographic structure, and are technologically important as computer memory cores and as protective scales formed during the oxidation of high-temperature alloys.

To aid in the design of future alloys for high-temperature service, it is necessary to know the mechanisms by which oxide spinels form, the rates at which they form and the influence of common alloy impurities on both their rates and mechanisms of formation. This type of information cannot readily be obtained by oxidation experiments in binary or higher-order alloys, because a variety of complex reactions can occur which complicate interpretation. The simplest and most direct method for studying oxide spinel formation is the isothermal reaction of pure or impure binary oxides to form the ternary spinel.

The particular spinels studied in this work are nickel chromite ($NiCr_2O_4$) and cobalt chromite ($CoCr_2O_4$). These spinels were chosen for study because they are common oxidation products of a variety of widely used alloys, and are partially responsible for the oxidation resistance of nickel-chromium and cobalt-chromium binary alloys, nickel-chromium based and cobalt-chromium based superalloys, and austenitic stainless steels.

In the review section, the pertinent theoretical and experimental literature on spinel formation is discussed. This review emphasizes the sophisticated theoretical treatments that are directly applicable to studies of the mechanisms and kinetics of spinel formation. The review also presents a variety of experimental studies of oxide spinel

formation, and emphasizes the experimental complications in the determinations of reaction mechanisms for oxide spinels in general and for nickel and cobalt chromites in particular.

In the experimental portion of this work, the mechanisms and rates of nickel chromite and cobalt chromite formation are studied by reacting dense, high-purity, manganese-doped, and silicon-doped nickel and cobalt oxides with dense, high-purity chromium oxide. The objectives of this work are: first, to determine the mechanisms and rates of nickel chromite and cobalt chromite formation from dense, high-purity oxides and, second, to determine the mechanisms and rates of nickel chromite and cobalt chromite formation from dense, manganese-doped, and silicon-doped nickel and cobalt oxides. None of these experimental variables have been studied previously. Previous kinetic studies of nickel chromite and cobalt chromite formation have been limited to low density oxides ($\leq$ 80% of theoretical density) in which vapor transport effects through oxide pores complicated interpretation. Further, there is only limited information[1] on the influence of impurities on spinel formation. The impurities for these studies (Si and Mn) were chosen on the basis of previous studies by Hickman and Gulbransen[2] and Douglass[3] in which these impurities strongly affected oxidation rates of Ni-Cr and Fe-Ni-Cr alloys by preventing or enhancing the formation of spinels.

In the results and discussion sections, the mechanisms and rates of spinel formation from pure and doped oxides are compared with the mechanisms and rates determined in previous studies and with theoretically determined reaction rates. These results are discussed in terms of the rate-controlling mechanisms for spinel formation, and conclusions are presented in the final section.

The basic objectives of this work were to obtain data which would enable an evaluation to be made of the role of spinels as constituents of oxide scales in the oxidation behavior of complex alloys. Because the work to be reported is so extensive, there will be no attempt to relate these data to actual oxidation behavior. A separate report concerning the oxidation behavior of Ni-20Cr and Co-20Cr doped with either silicon or manganese will consider the role that spinels play in the oxidation behavior.

II REVIEW

Stoichiometric formulas of spinels can be AB_2X_4, A_2BX_4, or A_3X_4. The first formula represents the normal spinel structure in which divalent cation A is in a tetrahedral site, trivalent cation B is in an octahedral site, and divalent anion X is in a normal anion site. A may also be a tetravalent cation and B a divalent cation. The first combination is therefore known as a normal 2-3 spinel, while the second is known as a normal 2-4 spinel. The second formula represents an inverse spinel, the A cations being in octahedral sites and the B cation in a tetrahedral site. In the inverse spinel the cations may also take a 2-4 combination in which the A cations are divalent and the B cation is tetravalent. The third formula represents the special case in which the spinel is formed from single element cations which exist in two ionization states in the crystal.

The possible spinel chemical compositions are shown in Table 1. Close inspection of this Table reveals that the nomenclature is not entirely consistent with the ionization states; i.e., the normal 2-4 spinel should probably be called a normal 4-2 spinel.

Table 1

SPINEL NOMENCLATURE

Nomenclature		Formula	Ionization State		
Normal	2-3	AB_2X_4	A^{2+}	B^{3+}	X^{2-}
Normal	2-4	AB_2X_4	A^{4+}	B^{2+}	X^{2-}
Inverse	2-3	A_2BX_4	A^{3+}	B^{2+}	X^{2-}
Inverse	2-4	A_2BX_4	A^{2+}	B^{4+}	X^{2-}
		A_3X_4	A^{2+}	A^{3+}	X^{2-}

A. Cation Diffusion in Spinel Structures

The spinel crystal is cubic, and its unit cell consists of 32 anions packed in a nearly face-centered-cubic lattice. A schematic representation of one eighth of the spinel unit cell is shown in Fig. 1. This packing results in the formation of 64 tetrahedral sites (interstitial sites equidistant from four nearest neighbor anions) and 32 octahedral sites (interstitial sites equidistant from six nearest neighbor anions). Of those available, only 8 of the tetrahedral and 16 of the octahedral sites are occupied in the spinel unit cell.

As is evident from Fig. 1, each occupied octahedral site has 12 nearest neighbor octahedral sites (6 of which may be occupied) and 8 nearest neighbor tetrahedral sites (none of which may be occupied). Conversely, each occupied tetrahedral site has 6 nearest neighbor tetrahedral sites (none occupied and 4 nearest neighbor octahedral sites (none occupied).[4]

Diffusion of cations in spinel structures may be by any of three mechanisms: vacancy diffusion, in which a cation simply exchanges places with a vacant octahedral site; interstitial diffusion in which a cation in a tetrahedral site can displace an ion in an adjacent octahedral site into a tetrahedral site; and voidal diffusion in which cations move from one normally unoccupied tetrahedral site to a normally unoccupied octahedral site.[5] Qualitative examples of possible cation diffusion paths in a normal 2-3 spinel can be seen in Fig. 1. A B^{3+} cation moving directly from an octahedral lattice position to an adjacent octahedral lattice position must pass between two X^{2+} anions at their point of closest approach (path 1, Fig 1). An alternative diffusion path is for the B^{3+} cation to move from its octahedral site to an adjacent unoccupied tetrahedtral site and thence to another octahedral site (path 2), thus minimizing the strain energy for transport along path 1. Similarly the direct diffusion path of the A^{2+} cation

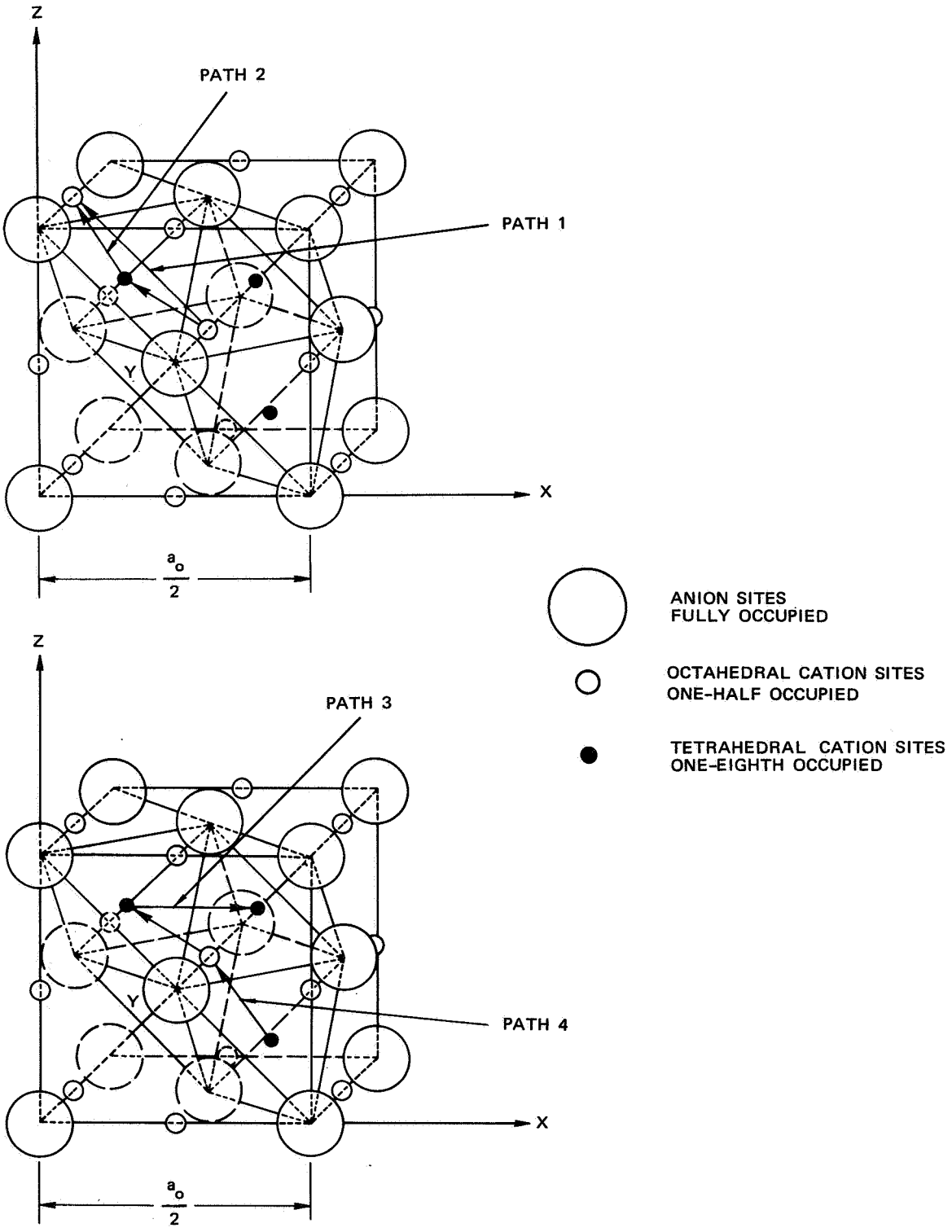

FIGURE 1 SCHEMATIC REPRESENTATION OF ONE-EIGHTH OF SPINEL UNIT CELL. For clarity, only three tetrahedral sites are shown.

from one tetrahedral site to an adjacent tetrahedral site (path 3) requires the cation to pass between two anions at their point of closest approach. However, the series of jumps that take the A^{2+} ion from its tetrahedral site through an adjacent octahedral site and then to a tetrahedral site (path 4) requires less strain energy than the direct tetrahedral-tetrahedral jump.

It is difficult to determine whether octahedral-octahedral or octahedral-tetrahedral paths are favored for cation diffusion in spinels. Studies of the preference energies for cation occupation of octahedral or tetrahedral sites have been made by Goodenough[6] and reviewed by Dils.[7] Briefly, these studies have shown that many transition metal ions have strong preference for octahedral rather than tetrahedral coordination. For example, ions such as Mn^{3+}, Cr^{3+}, and Ni^{2+} have octahedral site preference energies of 1.37, 1.97, and 1.22 eV, while ions such as Co^{2+} and Mn^{2+} have site preference energies of 0.19 and 0.37 eV. Therefore, the former ions are biased toward octahedral-octahedral jumps, while the latter could readily take octahedral-tetrahedral diffusion paths.

Published measurements of cation diffusion in oxide spinels[8-16] are shown in Table 2. The reliability of some of these data, however, is open to question, because of the poor reproducibility of the measurements. For example, the measured diffusion rates for Zn^{2+} in zinc ferrite differ by 4 orders of magnitude, and measured activation energies for Cr^{3+} diffusion in nickel chromite differ by 27 kcal/mole. It is evident, therefore, that these data must be used carefully. It will be shown later in this section that special criteria must be met before diffusion measurements of ternary systems will produce meaningful data. Only those diffusion data that meet these criteria will be used in the interpretation of experimental results obtained in this work.

Table 2

PRE-EXPONENTIALS AND ACTIVATION ENERGIES FOR CATION DIFFUSION IN OXIDE SPINELS

Spinel	A^{2+} D_0, cm^2/sec	A^{2+} Q, kcal/mole	Reference	B^3 D_0, cm^2/sec	B^3 Q, kcal/mole	Reference
$ZnCr_2O_4$	60	85	9	9	81	9
$CoCr_2O_4$	10^{-3}	51	8	2	70	8
	80	90	10	300	85	10*
$NiCr_2O_4$	1.5×10^{-3}	61.4	11	0.75	73	9
	0.85	75	12, 9	200**	89**	10*
$CaFe_2O_4$	30	86	13	3.2	72	13
				0.4	72	12
$ZnFe_2O_4$	10^3	86	14	10^3	82.	15
	8.8×10^{-2}	86	12	8.5×10^2	82.	12
$NiAl_2O_4$	2.9×10^{-5}	53.3	16	2.9×10^{-5}	53.3 (Fe)	11*
				1.17×10^{-3}	50.0 (Cr)	11*

* Preferred data; T, P, p_{O_2}, and a_{AO} or $a_{B_2O_3}$ fixed during measurement.
**Note error in Table 1, reference 10. Pre-exponential and activation energy have been recalculated from original data, Fig. 5 of reference 10.

B. Defect Equilibria

The defect equilibria of ternary ionic crystals (of which spinels are a special case) have been studied in detail by Schmalzried and Wagner[17] and by Schmalzried.[18] The importance of these studies to the interpretation of spinel formation experiments warrants a summary of their approaches and conclusions.

A ternary ionic crystal consists of one phase and three components. To define the thermodynamic state of the crystal we must fix four state variables in accordance with the phase rule. If four of the state variables are not fixed, the state is not defined, and measurements of reaction rates, diffusivities, and conductivities are equally undefined. It is for this reason that many of the diffusion data for spinel systems are only of qualitative value, since only T, P, and p_{O_2} were fixed. In ternary systems it is generally convenient (theoretically) to fix the thermodynamic activity of one of the cations in addition to T, P, and p_{O_2} The experimental methods by which the fourth state property is fixed, however, are very dependent on the particular system and measurement of interest.

The defect notations of Kroger and Vink[19] are given below. This notation uses dots to indicate excess positive charges, and primes to indicate excess negative charges related to the nominal electrostatic charges of the normal lattice constituents.

A_A cation A on its normal lattice site

B_B cation B on its normal lattice site

X_X anion X on its normal site

$A_i^{\bullet\bullet}$ divalent cation A on an interstitial site

$B_i^{\bullet\bullet\bullet}$ trivalent cation B on an interstitial site

X_i'' divalent anion X on an interstitial site

$V_X^{\bullet\bullet}$ anion vacancy in normal X site

A_B' cation A on normal B site (defect has a negative charge)

$B_A^{\cdot}$ cation B on a normal A site (defect has a positive charge)

e' excess electron

$h^{\cdot}$ electron hole

Concentrations are noted in parentheses, and are in units of number of defects per lattice molecule. For example, the notation (A_B') represents the number of A cations on normal B sites per molecule of AB_2X_4.

To relate the defect equilibria to the stoichiometry of the spinel it is first necessary to write its stoichiometric formula as

$$(1 + \alpha)\ AX + (1 + \beta)B_2X_3 = A(1 + \alpha)\ B_2(1 + \alpha)X\ (4 + \alpha + 3\beta) \qquad (1)$$

With this notation, the stoichiometry of the crystal is defined by

$$\frac{(1 + \beta)}{(1 + \alpha)} \equiv 1 + y \qquad (2)$$

where $y \simeq 0$ defines a stoichiometric spinel

$y > 0$ defines spinel containing excess B_2X_3

$y < 0$ defines a spinel containing excess AX

The following major assumptions are then made in order to relate the stoichiometry parameter (y) to the possible types of defects in the spinel;

1. Negligible electronic disorder exists in the spinel.

2. Cations may not substitute on normal anion lattice sites.

By writing a series of mass balance equations for cations and anions, and site balance equations for cation and anion sites, the possible defect pairs in the spinel crystal can be related to the stoichiometry parameter (y) as shown in Table 3. If the anion defect

Table 3

POSSIBLE DEFECT PAIRS IN SPINEL CRYSTALS[18]

Stoichiometry	Defect Pairs
$y \simeq 0$ ideal	$(A_i^{\bullet\bullet}, V_A'')$; $(B_i^{\bullet\bullet\bullet}, V_B''')$; $(A_B', B_A^{\bullet})$; $(V_X^{\bullet\bullet}, X_i'')$
$y > 0$ excess B_2X_3	$(B_i^{\bullet\bullet\bullet}, V_A'')$; $(B_i^{\bullet\bullet\bullet}, X_i'')$; $(V_A'', B_A^{\bullet})$; $(V_A'', V_X^{\bullet\bullet})$; $(V_B''', B_A^{\bullet})$; $(B_A^{\bullet}, X_i'')$
$y < 0$ excess AX	$(A_i^{\bullet\bullet}, V_B''')$; $(A_i^{\bullet\bullet}, A_B')$; $(A_i^{\bullet\bullet}, X_i'')$; $(B_i^{\bullet\bullet\bullet}, A_B')$; $(V_B''', V_X^{\bullet\bullet})$; $(A_B', V_X^{\bullet\bullet})$

concentrations are small in comparison to the cation defect concentrations, the number of possible defect pairs is significantly reduced. The defect concentrations of Table 4 are therefore determined from Table 3 by assuming low anion defect concentrations and accounting for electroneutrality in the spinel. Having the data of Table 4, it is then necessary to have a basis for deciding which of the defect pairs controls the properties of the spinel, i.e., which defects exist in greatest concentrations.

Schmalzried has determined a series of numerical coefficients that are characteristic of the defects in a spinel, by combining the mass and site balance equations mentioned previously with a series of equilibrium defect equations of the form:

$$A_A = A_i^{\bullet\bullet} + V_A''; \quad K_1 = \frac{(V_A'')(A_i^{\bullet\bullet})}{(A_A)} \tag{3}$$

where K_1 the equilibrium constant for equation 3, is based on low concentrations of noninteracting defects. From these equations and

Table 4

CATION DEFECT CONCENTRATION RELATIONS FOR AB_2X_4

Stoichiometry				
$y \simeq 0$ ideal	$(A_i^{\bullet\bullet}) = (V_A'')$;	$(B_i^{\bullet\bullet\bullet}) = (V_B''')$;	$(A_B') = (B_A^{\bullet})$	
$y > 0$ excess B_2X_3	$3(B_i^{\bullet\bullet\bullet}) = 2(V_A'')$;	$2(V_A'') = (B_A^{\bullet})$;	$2(V_B''') = (B_A^{\bullet})$	
$y < 0$ excess Ax	$2(A_i^{\bullet\bullet}) = 3(V_B''')$;	$2(A_i^{\bullet\bullet}) = (A_B')$;	$3(B_i^{\bullet\bullet\bullet}) = (A_B')$	

the integrated Gibbs-Duhem equation for the spinel, it is possible to relate the activity of a_{AX} to the concentration of the defect (i) by equations of the form

$$d\ \ell n\ (i) = n_i\ d\ \ell n\ a_{AX} \tag{4}$$

where n_i is a numerical coefficient that characterizes the defect. The values of n_i for various cation defects are given in Table 5. The characteristic cation defect coefficients of Table 5 must then be related to a measurable property of the spinel in order to determine the defect structure experimentally. Schmalzried has shown that the self-diffusion coefficients of ions in spinel crystals are related to activities by the equation:

$$D_j\ (a'_{AX})/D_j(a''_{AX}) = (a'_{AX}/a''_{AX})^{n_i} \tag{5}$$

where $D_j(a'_{AX})$ is the self-diffusion coefficient of ion j in the spinel, which is in equilibrium with AX of activity a'_{AX}

$D_j(a''_{AX})$ is the self diffusion coefficient of ion j in the spinel, which is in equilibrium with AX of activity a''_{AX}

n_i is the chracteristic defect coefficient

Table 5

CHARACTERISTIC COEFFICIENT OF CATION DEFECT PAIRS[18] IN AB_2X_4

Defect Pairs	$n_A = \frac{\partial \ln (A_i^{\bullet\bullet})}{\partial \ln a_{AX}}$	$n_B = \frac{\partial \ln (B_i^{\bullet\bullet\bullet})}{\partial \ln a_{AX}}$
$A_i^{\bullet\bullet}$, V_B'''	4/5 (0.8)	-4/5 (-0.8)
$A_i^{\bullet\bullet}$, A_B'	4/3 (1.33)	0
$B_i^{\bullet\bullet\bullet}$, A_B'	2	1
$A_i^{\bullet\bullet}$, V_A''	0	-2
A_B', $B_A^{\bullet}$	4	4
$B_i^{\bullet\bullet\bullet}$, V_B'''	4/3 (1.33)	0
$B_i^{\bullet\bullet\bullet}$, V_A''	4/5 (0.8)	-4/5 (-0.8)
$B_A^{\bullet}$, V_B'''	2	1
$B_A^{\bullet}$, V_A''	4/3	0

It is experimentally simple to measure diffusion coefficients at fixed T, P, p_{X_2} with specimens in equilibrium with either pure AX or pure B_2X_3. Since the activities of the two assumed components in equilibrium with the spinel are related by the integrated form of the Gibbs-Duhem equation,

$$a_{AX} \cdot a_{B_2X_3} = \exp [\Delta G^0/RT] \tag{6}$$

equation 5 is simplified to

$$\frac{D_j \ (a_{AX} = 1)}{D_j \ (a_{B_2X_3} = 1)} = \exp [n_i \ \Delta G^0/RT] \tag{7}$$

or

$$n_i = \frac{RT}{\Delta G^0} \ln \left[\frac{D_j \ (a_{AX} = 1)}{D_j \ (a_{B_2X_3} = 1)}\right] \tag{8}$$

where ΔG^0 is free of energy of formation of the spinel when reactants and products are in their standard state.

Measurements of the ratios of diffusion coefficients of cations in spinels at fixed values of T, P, p_{X_2} and a_{AX} have been made for a variety of spinels including nickel chromite and cobalt chromite.[18] These data are shown in Table 6, along with the experimentally determined values of n_i and probable disorder types. As the Table shows, Schmalzried has interpreted the values of n_i to mean that nickel and cobalt chromite have excess interstitial nickel and cobalt ions, respectively, which are compensated for by chromium vacancies. Conversely, cobalt aluminate contains interstitial aluminum ions and cobalt vacancies.

Comparison of the experimentally determined values of n_i with the theoretical values in Table 5 reveals that the probable rate-controlling defects in nickel and cobalt chromite spinels could also be interstitial chromium and nickel/cobalt vacancies, respectively, as well as the defects proposed by Schmalzried.

Schmalzried has presented no argument to defend his choice of probable defects in these systems. However, this approach has narrowed the number of possible defect types that control transport reactions in cobalt and nickel chromite spinels from a total of 16 possibilities to 2 possibilities, namely $(A_i^{\bullet\bullet}) = 3/2\ (V_B'''')$ or $(B_i^{\bullet\bullet\bullet}) = 2/3\ (V_A'')$. Each of these probable defect pairs has the same value of the characteristic defect coefficient ($n_A = 4/5$); this value will be used in the calculations of the theoretical parabolic reaction rate constants for nickel chromite and cobalt chromite formation.

C. Theoretical Models of Spinel Formation

For the purposes of this study the reaction system is defined as follows. The starting oxides AO and B_2O_3 are placed in contact along a planar interface. As the reaction

$$AO + B_2O_3 \rightarrow AB_2O_4 \qquad (9)$$

Table 6

EXPERIMENTALLY DETERMINED DIFFUSION-CONTROLLING DEFECTS IN OXIDE SPINELS[18]

Spinel	Temp, °C	Cation	a'_{AO}/a''_{AO}	D'/D''	n_i	Probable Defects
$CoCr_2O_4$	1200	Co^{60}	10	2-3	+ 0.40	$(Co_i^{\bullet\bullet\bullet}) \simeq 3/2\ (V_{Cr}^{'''})$
$CoCr_2O_4$	1200	Cr^{51}	10	0.3-0.4	$\sim$ -0.45	$(Co_i^{\bullet\bullet}) \simeq 3/2\ (V_{Cr}^{'''})$
$NiCr_2O_4$	1200	Cr^{51}	8	0.2	$\sim$ -0.77	$(Ni_i^{\bullet\bullet}) \simeq 3/2\ (V_{Cr}^{'''})$
$CoAl_2O_4$	1200	Co^{60}	5	0.2	$\sim$ -1.0	$(Al_i^{\bullet\bullet\bullet}) \simeq 2/3\ (V_{Co}^{''})$

proceeds, a layer of spinel forms between the starting oxides. For the initial discussion it will be assumed that all oxides are of theoretical density, that electroneutrality is maintained, and that nonequilibrium defects, such as dislocations and grain boundaries, do not influence the spinel formation rates. With these restrictions, it is apparent that the spinel growth rate will be diffusion limited, since the chemical reaction is rapid in comparison with transport through the oxide.

If the mechanism is diffusion controlled, then the rate of thickening of the spinel layer ($d(\Delta x)/dt$) will be inversely proportional to the thickness (Δx). Stated explicitly,

$$\frac{d(\Delta x)}{dt} = \frac{k}{x} \tag{10}$$

Integration and rearrangement yields

$$\Delta x^2 = 2k_p t \tag{11}$$

where k_p is the parabolic rate constant for the formation of a spinel layer of thickness Δx during time t.

With the given restrictions, it is evident that the mechanism that controls the rate constant can readily be determined by appropriate marker measurements, and, once the mechanism is determined a theoretical value for the rate constant can be calculated and compared with the experimental rate constant from equation 11.

The possible mechanisms are shown schematically in Fig. 2. Mechanism 1 represents diffusion of doubly ionized cations and anions through the spinel layer and reaction at the spinel/B_2O_3 interface. In this mechanism, any markers at the original (AO/B_2O_3 interface will be found at the AO/spinel interface after the reaction. It is evident that this mechanism is independent of the oxygen activity in the surrounding gas atmosphere. Since it is commonly thought that anion

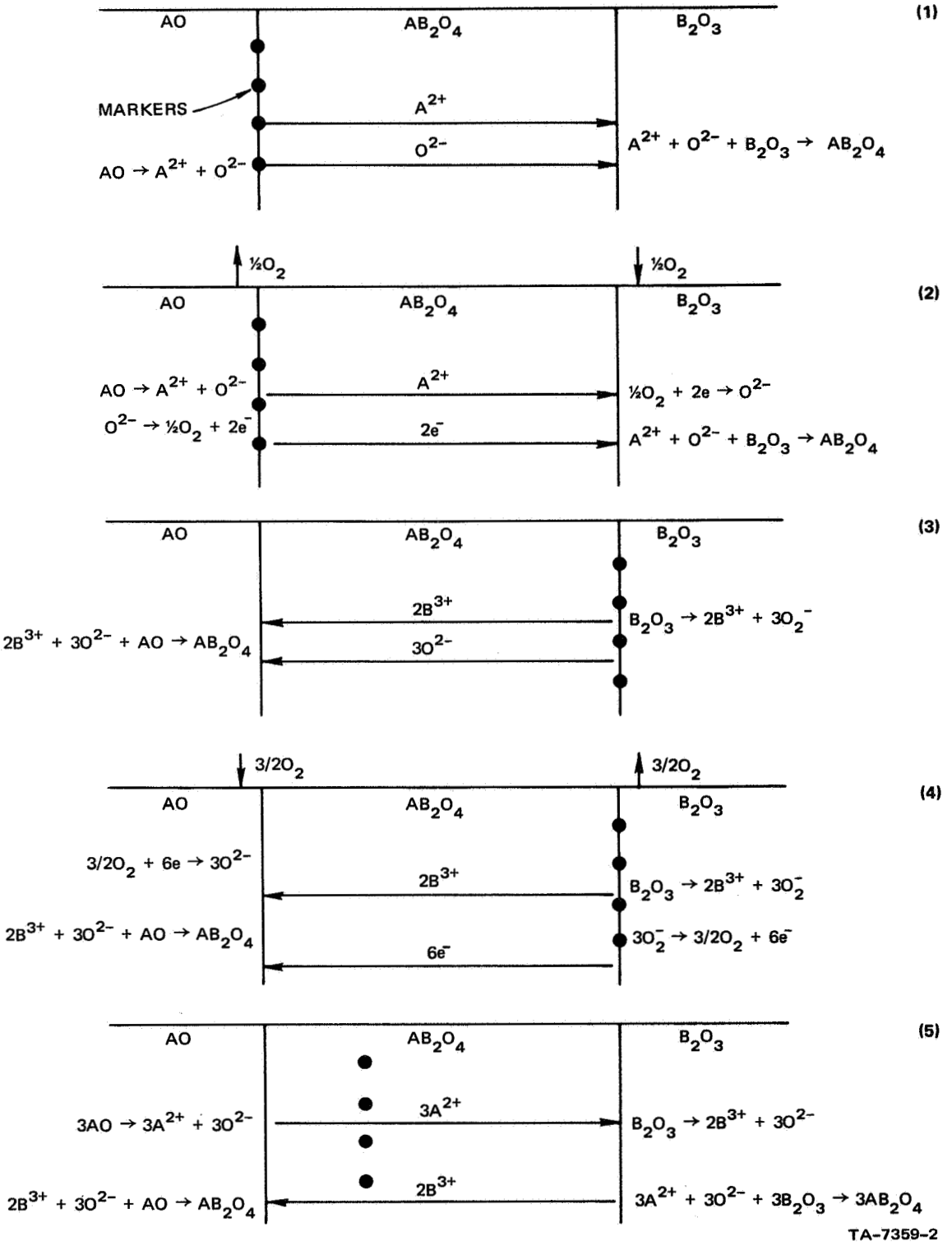

FIGURE 2 EXAMPLES OF POSSIBLE SPINEL REACTION MECHANISMS: (1) Divalent cation and anion diffusion; (2) Divalent cation and electron diffusion; (3) Trivalent cation and divalent anion diffusion; (4) Trivalent cation and electron diffusion; (5) Countercurrent cation diffusion.

diffusion through the spinel layer is slow with respect to cation diffusion, mechanisms such as 2 have been developed in which oxygen follows a short-circuit path through the gas phase while divalent cations and electrons diffuse through the spinel layer.[21,22,26]

The reaction sequence is: (a) dissociation of the A^{2+} and O^{2-} ions in AO, (b) reaction of O^{2-} anions to form oxygen gas at the specimen surface and excess electrons in the AO, (c) simultaneous transport of oxygen through the gas phase and A^{2+} and excess electrons through the spinel layer, (d) ionization of oxygen with excess electrons at the B_2O_3 surface, and (e) reaction of A^{2+} and O^{2-} with B_2O_3 to form spinel. Mechanism 2 will leave the marker at the same location as mechanism 1, but it can operate only when there is a sufficient oxygen partial pressure in the gas phase, and when there is a possible path for oxygen, i.e., when the reaction product doesn't physically isolate the reactants. It is evident that mechanism 2 avoids the problem of slow anion diffusion in the spinel by the substitution of anion diffusion in the starting oxides (which could be as slow).

Mechanisms 3 and 4 in Fig. 2 are analogous to 1 and 2, respectively. In 3 and 4 the trivalent cations are moving, and thus the marker at the original AO/B_2O_3 interface will be found at the spinel/B_2O_3 interface after the reaction.

Mechanism 5, often called the Wagner mechanism, represents inverse cation diffusion through the spinel layer. This mechanism completely avoids the need for anion transport through the spinel layer, through the starting oxides, or through the gas phase. The sequence of reactions is as follows: (a) simultaneous dissociation of 3AO to form $3A^{2+}$ and $3O^{2-}$, and B_2O_3 to form $2B^{3+}$ and $3O^{2-}$; (b) simultaneous countercurrent diffusion of $3A^{2+}$ and $2B^{3+}$ ions across the spinel, leaving excess anions in the starting oxides (since both starting oxides are in equilibrium with the same gas phase, there is no oxygen activity gradient across the spinel and hence no anion diffusion);

(c) reaction of the $2B^{3+}$ ions with the excess oxygen anions and AO to form AB_2O_4 and reaction of the $3A^{2+}$ ions with excess oxygen anions and B_2O_3 to form $3AB_2O_4$. This reaction mechanism is such that one AB_2O_4 molecule forms on the AO side of the original interface (as defined by the marker position) for every three AB_2O_4 molecules that form on the B_2O_3 side. Thus the marker is buried within the spinel layer, such that the theoretical ratio of spinel thickness on the AO side to spinel thickness on the B_2O_3 side is 1/3.

D. The Wagner-Schmalzried Theory

It is apparent that the simple mechanisms described in Fig 2 should be amenable to theoretical calculations which develop explicit relations between known kinetic and thermodynamic properties of the spinel and its parabolic growth rate constant. Such treatments have been made initially by Wagner[20] and expanded by Schmalzried.[21,22] The basic assumptions in this treatment are:

(a) The reaction layer is dense, and does not contain nonequilibrium defects such as dislocations or grain boundaries.

(b) Interface reactions are fast in comparison with ion transport through the spinel.

(c) Diffusing species are coupled only by the requirements of local equilibrium and electroneutrality, and otherwise move independently.

(d) Thermodynamic equilibrium exists at phase boundaries.

In these treatments, the authors have chosen to emphasize ionic rather than defect fluxes in their evaluation of spinel reaction rates, and to relate the ionic diffusivities to the characteristic coefficients of the predominant defect equilibria in the spinel. The three principal spinel formation mechanisms that must be considered are inverse cation diffusion ($D_{A^{2+}}$ and $D_{B^{3+}} \gg D_{O^{2-}}$), divalent cation and anion diffusion (($D_{A^{2+}}$ and $D_{O^{2-}} \gg D_{B^{3+}}$), and trivalent cation and divalent

anion diffusion ($D_{B^{3+}}$ and $D_{O^{2-}} \gg D_{A^{2+}}$). Only the first mechanism (inverse cation diffusion) will be described in detail, since the steps in the derivation of the other mechanisms will be similar.

The flux of ions $\tilde{j}_i$ (in equivalents) across the spinel layer is given by

$$\tilde{j}_i = \frac{D_i \tilde{C}_i z_i}{RT} \cdot \frac{d\tilde{\eta}_i}{dx} \qquad (12)$$

Where D_i is the diffusion coefficient of ion i, $\tilde{C}_i$ is the equivalent concentration of i ions per unit volume, z_i is the valence (absolute value) of ion i, and $d\tilde{\eta}_i/dx$ is the electrochemical potential gradient per equivalent of ion i across the spinel layer. The use of the equivalent rather than mole or mole fraction is required for this treatment, since the diffusing species are ions. The equivalent is determined by the product of the molar concentration and the absolute charge of the ion. Thus, 1 mole of spinel AB_2O_4, which contains 1 mole of A^{2+} ions, 2 moles of B^{3+} ions, and 4 moles of O^{2-} ions, contains 2 equivalents of A^{2+} ions, 6 equivalents of B^{3+} ions, and 8 equivalents of O^{2-} ions. In the inverse cation diffusion mechanism, the equivalent fluxes of ions diffusing across the spinel layer are equal because of electroneutrality requirements, or

$$\tilde{j}_{A^{2+}} = -\tilde{j}_{B^{3+}} = \tilde{j} \qquad (13)$$

Thus* $$\tilde{j}_A = -\frac{D_A \tilde{C}_A z_A}{RT} \cdot \frac{d\tilde{\eta}_A}{dx} = \tilde{j} \qquad (14)$$

and $$\tilde{j}_B = -\frac{D_B \tilde{C}_B z_B}{RT} \cdot \frac{d\tilde{\eta}_B}{dx} = \tilde{j} \qquad (15)$$

Rearranging and combining equations 14 and 15 yields

$$\tilde{j} = \left[\frac{D_A \tilde{C}_A z_A \cdot D_B \tilde{C}_B z_B}{D_A \tilde{C}_A z_A + D_B \tilde{C}_B z_B}\right] \cdot \frac{1}{RT}\left(\frac{d\tilde{\eta}_A}{dx} - \frac{d\tilde{\eta}_B}{dx}\right) \qquad (16)$$

---

* The charge notations on the ions has been removed for simplification and clarity; all A and B notations are for A^{2+} and B^{3+} ions, respectively.

Assuming that the spinel is an intermediate phase in a quasi-binary oxide system composed of AO and B_2O_3 allows the use of the Gibbs-Duhem equation to relate the chemical potential gradients of AO and B_2O_3. Writing the chemical potentials of the individual oxides in the system as the sum of electrochemical potentials of the ions yield

$$\mu_{AO} = \tilde{\eta}_A + \tilde{\eta}_O \tag{17}$$

$$\mu_{B_2O_3} = 2\tilde{\eta}_B + 3\tilde{\eta}_O \tag{18}$$

where equations 17 and 18 are written for molar concentrations. Eliminating $\tilde{\eta}_O$ from equations 17 and 18 and simplifying yields

$$3\mu_{AO} - \mu_{B_2O_3} = 3\tilde{\eta}_A - 2\tilde{\eta}_B \tag{19}$$

Differentiating with respect to x yields

$$3\frac{d\mu_{AO}}{dx} - \frac{d\mu_{B_2O_3}}{dx} = 3\frac{d\tilde{\eta}_A}{dx} - 2\frac{d\tilde{\eta}_B}{dx} \tag{20}$$

Substituting the Gibbs-Duhem relation,

$$d\mu_{AO} = -d\mu_{B_2O_3} \tag{21}$$

into equation 20 and simplifying yields

$$4\left(\frac{d\mu_{AO}}{dx}\right) = 3\left(\frac{d\tilde{\eta}_A}{dx}\right) - 2\left(\frac{d\tilde{\eta}_B}{dx}\right) \text{ (in moles)} \tag{22}$$

$$4\left(\frac{d\tilde{\mu}_{AO}}{dx}\right) = 3\left(\frac{d\tilde{\eta}_A}{dx} - \frac{d\tilde{\eta}_B}{dx}\right) \text{ (in equivalents)} \tag{23}$$

where $d\tilde{\mu}_{AO}/dx$ is the chemical potential per equivalent of AO.

Substituting equation 23 into equation 16 yields

$$\tilde{j} = \left[\frac{D_A \tilde{C}_A z_A \cdot D_B \tilde{C}_B z_B}{D_A \tilde{C}_A z_A + D_B \tilde{C}_B z_B}\right] \cdot \frac{4}{3RT}\left(\frac{d\mu_{AO}}{dx}\right) \tag{24}$$

the equivalent flux per unit time ($\dot{n}$) across the total reaction layer of thickness Δx and cross section q is given by integration of equation 24 to yield

$$\dot{n} = \frac{q}{\Delta x}\left\{\left[\frac{-D_A \tilde{C}_A z_A \cdot D_B \tilde{C}_B z_B}{-D_A \tilde{C}_A z_A + D_B \tilde{C}_B z_B}\right] \cdot \frac{4}{3RD}\left(\tilde{\mu}'_{AO} - \tilde{\mu}''_{AO}\right)\right\} \qquad (25)$$

Where $\tilde{\mu}'_{AO}$ and $\tilde{\mu}''_{AO}$ are the chemical potentials per equivalent on the AO and B_2O_3 sides, respectively, of the spinel layer. The difference between $\tilde{\mu}'_{AO}$ and $\tilde{\mu}''_{AO}$ is the free energy of formation of AB_2O_4 per equivalent. The quantity in brackets represents the average values of the diffusion coefficients, and equivalent concentrations of ions across the spinel layer.

Now the product of the spinel growth rate $d(\Delta x/dt)$ and the cross section area q is equal to the product of the flux of equivalents ($\dot{n}$) per unit time and the volume of spinel formed per equivalent ($\tilde{V}$). Stated explicitly,*

$$q \cdot \frac{d(\Delta x)}{dt} = \dot{n}\tilde{V} \qquad (26)$$

Substitution of equation 26 into 25 and simplification yields

$$\frac{d(\Delta x)}{dt} = \frac{\tilde{V}}{\Delta x}\left\{\left[\frac{-D_A \tilde{C}_A z_A \cdot D_B \tilde{C}_B z_B}{-D_A \tilde{C}_A z_A + D_B \tilde{C}_B z_B}\right] \cdot \frac{4}{3RT}\left(\tilde{\mu}'_{AO} - \tilde{\mu}''_{AO}\right)\right\}$$

or

$$\frac{d(\Delta x)}{dt} = \frac{\tilde{V}}{\Delta x} K \qquad (27)$$

where K is equal to the quantity in brackets and is known as the rational reaction constant. Integrating equation 27 yields the simple parabolic equation

$$\Delta x^2 = 2\tilde{V}Kt \qquad (28)$$

---

* The error in this equation given by Morkel and Schmalzried[10] has been corrected here.

From comparison with equation 11, it is evident that the simple parabolic reaction rate constant (k_p) for the inverse cation diffusion mechanism is given by

$$k_p = \tilde{V} K = \tilde{V} \left\{ \left[\frac{D_A \tilde{C}_A z_A \cdot D_B \tilde{C}_B z_B}{D_A \tilde{C}_A z_A + D_B \tilde{C}_B z_B} \right] \cdot \frac{4}{3} \left(\tilde{\mu}'_{AO} - \tilde{\mu}''_{AO} \right) \right\} \qquad (29)$$

Similar relations can be developed for other mechanisms such as unidirectional divalent anion and divalent cation diffusion

$$k_p = \tilde{V} K = \tilde{V} \left\{ \left[\frac{D_A \tilde{C}_A z_A \cdot D_O \tilde{C}_O z_O}{D_A \tilde{C}_A z_A + D_O \tilde{C}_O z_O} \right] \cdot \frac{1}{RT} \left(\tilde{\mu}'_{AO} - \tilde{\mu}''_{AO} \right) \right\} \qquad (30)$$

and unidirectional divalent anion and trivalent cation diffusion

$$k_p = \tilde{V} K = \tilde{V} \left\{ \left[\frac{D_B \tilde{C}_B z_B \cdot D_O \tilde{C}_O z_O}{D_B \tilde{C}_B z_B + D_O \tilde{C}_O z_O} \right] \cdot \frac{1}{3RT} \left(\tilde{\mu}'_{AO} - \tilde{\mu}''_{AO} \right) \right\} \qquad (31)$$

Inspection of equations 29, 30, and 31 shows that the equations can be greatly simplified if the component diffusion coefficients for each mechanism are sufficiently different. For example, if $D_A \ll D_B$ the reaction rate of equation 29 is controlled by diffusion of A^{2+} cations, and 29 is simplified to

$$k_p = \frac{4 \tilde{V} \bar{D}_A \tilde{C}_A z_A}{3RT} \left(\tilde{\mu}'_{AO} - \tilde{\mu}''_{AO} \right) . \qquad (32)$$

Other equations similar to 32 can be developed from equations 29 to 31. To evaluate the average value of the component diffusion coefficient for equation 32, Schmalzried and Wagner[20-22] have used the expression

$$\bar{D}_A = \frac{\int_{\tilde{\mu}''_{AO}}^{\tilde{\mu}'_{AO}} D_A \cdot d\mu_{AO}}{\int_{\tilde{\mu}''_{AO}}^{\tilde{\mu}'_{AO}} d\mu_{AO}} \qquad (33)$$

Changing the limits of the dividend and integrating the divisor yields

$$\bar{D}_A = \frac{RT\int_{a''_{AO}}^{a'_{AO}} D_A \cdot d\,\ell n\, a_{AO}}{\left(\tilde{\mu}'_{AO} - \tilde{\mu}''_{AO}\right)} \tag{34}$$

Substituting 34 into 32 and simplifying yields the expression

$$k_p = \frac{4}{3}\,\tilde{V}\,\tilde{C}_A\,z_A \cdot \int_{a''_{AO}}^{a'_{AO}} D_A\, d\,\ell n\, a_{AO} \tag{35}$$

To integrate equation 35, a relation between D_A and a_{AO} must be used. Such relation has been developed by Schmalzried and Wagner[17,21] in which the component diffusion D_A is related to the activity a_{AO} by a dimensionless factor n_A (described in the previous section), which is the characteristic coefficient of the defect equalibria controlling the diffusion mechanism. Explicitly this relation is:

$$D_A = D_A(a_{AO} = 1) \cdot (a_{AO})^{n_A} = D_A(a_{B_2O_3} = 1) \cdot (a_{B_2O_3})^{-n_A} \tag{36}$$

where the expression $D_A(a_{AO} = 1)$ represents the diffusion coefficient in the spinel adjacent to (and in equilibrium with) AO. Substituting 36 into 35 yields

$$k_p = \frac{4}{3}\,\tilde{V}\,\tilde{C}_A\,z_A\,D_A(a_{AO} = 1) \cdot \int_{a''_{AO}}^{a'_{AO}} (a_{AO})^{n_A}\,\frac{1}{a_{AO}}\,d(a_{AO}) \tag{37}$$

Integrating 37 and simplifying yields

$$k_p = \frac{4}{3}\,\tilde{V}\,\tilde{C}_A\,z_A\,D_A(a_{AO} = 1)\left[\frac{(a_{AO})^{n_A}}{n_A}\right]_{a''_{AO}}^{a'_{AO}} \tag{38}$$

Since $a'_{AO} = 1$ and $a''_{AO} = \exp(\Delta G^0/RT)$, equation 38 becomes

$$k_p = \frac{4}{3n_A}\,\tilde{V}\,\tilde{C}_A\,z_A\,D_A(a_{AO} = 1) \cdot [1 - \exp(n_A\,\Delta G^0/RT)] \tag{39}$$

Equation 39 relates the parabolic rate constant (which can be measured experimentally) with $\tilde{V}$, the volume of spinel formed per equivalent of A^{2+}; z_A, the absolute charge of cation A; $\tilde{C}_A$, the average concentration of A^{2+} in the spinel layer in equivalents per unit volume; $D_A(a_{AO} = 1)$, the diffusion coefficient of A^{2+} in spinel in equilibrium with AO; and ΔG^0, the free energy of formation of the spinel from its pure component oxides.

Measured values of the parameters required for the solution of equation 39 are available for a number of oxide spinels. These include diffusion coefficients,[8-16] defect coefficients,[17,18] and free energies of formation of spinels.[23]

E. Experimental Studies of Oxide Spinel Formation

A variety of experimental approaches have been used to elucidate the mechanisms by which oxide spinels form. Some approaches have resolved doubts concerning the controlling mechanisms, and others have raised doubts. In this section two oxide spinel systems studied will be reviewed. These are the aluminates and the chromites.

The studies on these two systems illustrate the experimental techniques used to determine the reaction mechanism, and also illustrate the conflicting results when more than one technique is applied to a given spinel. In addition, these studies show that a special technique which unambiguously confirms a given reaction mechanism in aluminates does not provide such confirmations in chromites.

1. Aluminates

The various features of aluminate formation studies are summarized in Table 7. Of particular importance in this table are the critical experiments on which the various authors based their conclusions. One of the earliest studies on aluminate systems was the work of Bengston and Jagitsch.[24] In these studies, pellets of zinc aluminate were

Table 7

SUMMARY OF ALUMINATE SPINEL FORMATION STUDIES

System	Critical Experiment	Indicated Mechanism	Remarks	Reference
$ZnAl_2O_4$	Reaction of ZnO, $ZnAl_2O_4$, and Al_2O_3 pellets in air; Pt markers at interface	Zn^{2+} → O^{2-} →	Markers at $ZnO/ZnAl_2O_4$ interface after reaction	Bengston and Jagitsch[24]
$ZnAl_2O_4$	Reaction of ZnO and Al_2O_3 pellets in air; Pt markers at interface	Zn^{2+} → O^{2-} →	Markers at ZnO/Al_2O_4 interface after reaction	Lindner and Akerstrom[9]
$NiAl_2O_4$	Reaction of NiO and Al_2O_3 pellets in air; Pt markers at interface	Ni^{2+} → O^{2-} →	Markers at $NiO/NiAl_2O_4$ interface after reaction	Lindner and Akerstrom[9]
$NiAl_2O_4$	Reaction of NiO and Al_2O_3 pellets in air; Pt markers at interface	Ni^{2+} → O^{2-} →	Markers at $NiO/NiAl_2O_4$ interface after reaction	Pettit et al.[25]
$NiAl_2O_4$	Reaction of NiO and Al_2O_3 Pellets in air and in argon	Ni^{2+} → Al^{3+} ←	Rate constants independent of oxygen partial pressure	Pettit et al.[25]
$NiAl_2O_4$	Reaction of NiO and Al_2O_3 pellets in air; chemical etching of spinel layer	Ni^{2+} → Al^{3+} ←	Porosity within spinel layer acts as "natural" marker; location of pores consistent with inverse cation diffusion	Pettit et al.[25]
$NiAl_2O_4$	Reaction of NiO polycrystals with Al_2O_3 single crystals in air	Ni^{2+} → Al^{3+} ←	Single crystal spinel layer in contact with Al_2O_3, polycrystal spinel layer in contact with NiO; ratio of single crystals and polycrystal spinel thicknesses consistent with inverse cation diffusion	Pettit et al.[25] Sockel[26]

Table 7, Concluded

System	Critical Experiment	Indicated Mechanism	Remarks	Reference
$MgAl_2O_4$	Reaction of Al_2O_3 pellets with MgO vapor in hydrogen, markers at oxide vapor interface	$Mg^{2+} \rightarrow$ $Al^{3+} \leftarrow$	Markers generally buried in spinel layer, but sometimes at spinel/vapor interface	Carter[27]
$CoAl_2O_4$	Reaction of CoO and Al_2O_3 pellets in air and in nitrogen; Pt markers at interface	$Co^{2+} \rightarrow$ $O^{2-} \rightarrow$	Markers at $CoO/CoAl_2O_4$ interface; reaction constants for air and nitrogen experiments the same	Schmalzried[21]
$CoAl_2O_4$	Reaction of CoO polycrystals with Al_2O_3 single crystal in air	$Co^{2+} \rightarrow$ $Al^{3+} \leftarrow$	Single crystal spinel layer in contact with Al_2O_3, polycrystal spinel layer in contact with CoO; ratio of polycrystal and single crystal spinel layers consistent with inverse cation diffusion	Sockel[26]

placed between pellets of zinc oxide and aluminum oxide. In another experiment, platinum markers were placed at the zinc oxide/alumina interface, and the assemblies were reacted in air at temperatures between 1250 and 1380°C. After the reactions, the individual pellets were separated and weighed. The platinum markers were found at zinc oxide/aluminate interface after the reaction, thus indicating that transport of Zn^{2+} and O^{2-} through the spinel was the controlling mechanism. In addition, the aluminum oxide pellets gained weight, while the zinc oxide pellets lost weight, thus providing further support for the proposed mechanism.

This experiment was essentially repeated by Lindner and Akerstrom.[9] Platinum markers placed between zinc oxide and alumina were found at the zinc oxide/spinel interface after the reaction. Lindner and Akerstrom[9] also performed the same experiment with nickel oxide and aluminum oxide and found the marker at the nickel oxide/spinel interface after the reaction. They concluded that the reaction mechanism was transport of Ni^{2+} and O^{2-} through the growing spinel layer.

These conclusions on the reaction mechanisms of zinc aluminate and nickel aluminate were criticized by Schmalzried[21] because the experimental procedures used did not exclude possible transport of oxygen through the vapor phase. Since the specimens used were porous, Schmalzried suggested that the reaction mechanism was more likely solid-state transport of Zn^{2+} and electrons through the spinel, and oxygen transport through the gas phase (see mechanism , in Fig. 2). Later work by Pettit et al.[25] and by Sockel[26] supported Schmalzried's arguments.

Pettit et al.[25] performed a series of critical experiments. In the first, they placed platinum markers at the initial aluminum oxide/nickel oxide interface and found the markers at the nickel oxide/nickel aluminate interface after reaction in air (in agreement with earlier experiments).

They assumed that the markers had moved during the experiment. Pettit et al.[25] then measured the parabolic rate constants for nickel aluminate formation in air and in argon. They found the reaction rates to be identical in both gases thus supporting the mechanism of inverse cation diffusion (mechanism 5 in Fig. 2). On etching the specimens, they also found a duplex spinel structure consisting of equiaxed crystals adjacent to the nickel oxide, and columnar crystals adjacent to the aluminum oxide. These layers were separated within the spinel by a line of pores such that the thickness ratio of the equiaxed to columnar grains was approximately 1:3. The experiment was repeated with a single crystal of nickel oxide and a polycrystal of aluminum oxide and the 1:3 thickness ratio of single crystal to polycrystal spinel was again observed (further proof that the Wagner method was operative). Pettit et al.[25] therefore concluded that the pores dividing the duplex spinel microstructure were "natural markers" which remained at the initial interface during the reaction, and that the spinel formation mechanism was countercurrent diffusion of Ni^{2+} and Al^{3+}. By comparing theoretically and experimentally determined parabolic reaction rate constants, they further concluded that the diffusion of Al^{3+} through the spinel layer controlled the reaction rate.

The experiments of Sockel[26] were similar to those of Pettit et al. and provided further proof of the inverse cation diffusion mechanism. Sockel reported that the reactions of single crystals of aluminum oxide and polycrystalline nickel oxide produced the same structure reported by Pettit et al. However, when Sockel reacted single crystalline nickel oxide and aluminum oxide, the expected single crystal spinel layer was not found.

The layer again consisted of 1/4 polycrystalline spinel adjacent to the nickel oxide and 3/4 single crystalline spinel adjacent to the aluminum oxide. This unexpected behavior was explained on the basis of vapor phase transport of nickel oxide from the single crystal nickel

oxide to the growing spinel layer, and countercurrent diffusion of Ni^{2+} and Al^{3+} through the spinel itself.

Carter[27] studied the reaction of alumina and magnesia in hydrogen atmospheres. In these studies, molybdenum markers that were originally at the aluminum oxide surface were generally (but not always) found buried in the spinel layer after reaction. Carter did not fully explain the erratic marker behavior, but his conclusion that the reaction mechanism was countercurrent diffusion of Mg^{2+} and Al^{3+} through the spinel was well supported. Indeed, it would be difficult to postulate any other mechanism operating in a closed hydrogen system at temperatures of 1800 to 1900°C.

The mechanisms of cobalt aluminate formation have been studied by Schmalzried[21] and Sockel.[26] In Schmalzried's experiments, polycrystals of cobalt oxide and aluminum oxide were reacted in air and in nitrogen. Platinum markers which were initially at the cobalt oxide/aluminum oxide interface were found at the cobalt oxide/spinel interface after reactions in either gas. Furthermore, measured reaction rate constants in the two gases were not significantly different. In view of these data, Schmalzried concluded that equidirectional transport of Co^{2+} and O^{2-} through the spinel layer could be the spinel growth mechanism.

In Sockels[26] thesis, the reaction of polycrystalline cobalt/oxide with single crystal aluminum oxide resulted in the formation of a duplex spinel layer, one fourth of which was polycrystalline, and three fourths of which was single crystalline. This experiment supported the Wagner mechanism of inverse cation diffusion of Co^{2+} and Al^{3+} through the spinel layer and explained the insensitivity of the reaction rate constants to the reaction gas observed by Schmalzried.[21] On comparison of the measured and theoretical reaction rates for the cobalt aluminate system, Schmalzried[29] later concluded that the mechanism of spinel formation in cobalt aluminate is inverse diffusion of Co^{2+} and Al^{3+}

through the cobalt aluminate layer and that the overall rate is controlled by the slowly diffusing Al^{3+} ions. He assumed that his initial marker experiments were affected by vapor phase transport of the cobalt oxide to the reaction interface. By this mechanism, the spinel layer could grow under the marker and leave it at the cobalt oxide/spinel interface after the reaction.

These studies have shown that inverse cation diffusion is the mechanism of formation of nickel, cobalt, and magnesium aluminates. The mechanism of formation of zinc aluminate is open to question in view of the confusing behavior of markers in these systems. Further, it appears that the diffusion of Al^{3+} is the rate controlling step in the formation of nickel and cobalt aluminates.

2. Chromites

Chromite spinel formation studies are summarized in Table 8. Hauffe and Pschera[28] studied the formation of nickel chromite by using the experimental arrangement proposed by Wagner.[20] Two pellets of nickel chromite were placed between nickel oxide and chromium oxide pellets and reacted at 1100°C. After the reaction the pellets were separated and weighed (presumably with no loss). Hauffe and Pschera observed that nickel oxide pellets adjacent to the nickel chromite pellets gained weight, while the nickel chromite pellets lost the same amount of weight. Nickel chromite pellets adjacent to the chromium oxide did not change weight, but the chromium oxide pellets lost weight. They interpreted these weight losses to mean that vaporization of chromium oxide from the pure pellets and from spinel occurred, and that this vapor phase transported to the nickel oxide pellets to form a new spinel layer. They provided further evidence of vapor phase transport from the spinel to the NiO by separating the two pellets by a 0.25 mm platinum ring before reaction. The weight changes in this experiment were the same as those in which no spacer was present. Therefore, the influence of vapor phase transport of some "Cr_2O_3 gas" species on the

Table 8

SUMMARY OF SPINEL FORMATION STUDIES

System	Critical Experiment	Indicated Mechanism	Remarks	Reference
$NiCr_2O_4$	Reaction of NiO, $NiCr_2O_4$, and Cr_2O_4 pellets in air measurements of weight change	Vapor phase transport of Cr_2O_3, $Ni^{2+} \rightarrow$ $Cr^{3+} \leftarrow$ assumed in solid state	NiO pellets increased in weight, adjacent $NiCr_2O_4$ pellets decreased in weight, Cr_2O_3 pellets decreased in weight, adjacent $NiCr_2O_4$ pellets increased in weight	Hauffe and Pschera[28]
$NiCr_2O_4$	Reaction of NiO and Cr_2O_3 pellets in air; measurements of rate constants and diffusion coefficients	$Ni^{2+} \rightarrow$ $Cr^{3+} \leftarrow$	Measured parabolic rate constant compared with theoretical value determined from Wagner theory and measured diffusion coefficients; Pt markers attacked	Lindner and Akerstrom[9]
$NiCr_2O_4$	Reaction of polycrystalline Cr_2O_3 and single crystal NiO	$Ni^{2+} \rightarrow$ $Cr^{3+} \leftarrow$	Measured parabolic rate constant compared with theoretical value determined from Wagner theory and known diffusion data	Sockel[26]
$NiCr_2O_4$	Reaction of polycrystalline Cr_2O_3 and single crystal NiO in air	$Ni^{2+} \rightarrow$ $Cr^{3+} \leftarrow$	Single crystal spinel formed, not bonded to Cr_2O_3 structure does not support the indicated mechanism	Sockel[26]
$CoCr_2O_4$	Reaction of CoO and Cr_2O_3 pellets in air; Pt markers at interface	$Co^2 \rightarrow$ $2e^- \rightarrow$ $O_2 \rightarrow$ gas phase	Markers found at $CoO/CoCr_2O_4$ interface after reaction	Schmalzried[21]

Table 8, Concluded

System	Critical Experiment	Indicated Mechanism	Remarks	Reference
$CoCr_2O_4$	Reaction of CoO and Cr_2O_3 pellets in N_2; Pt markers at interface	$Co^{2+} \rightarrow$ $Cr^{3+} \leftarrow$	Markers dissolved; parabolic rate constant in N_2 was 2-3 times smaller than in air, but was still greater than theoretical value for Wagner mechanism	Schmalzried[21]
$CoCr_2O_4$	Reaction of polycrystalline Cr_2O_3 and single crystal CoO in air	$Co^{2+} \rightarrow$ $2h^{\bullet} \leftarrow$ $O_2 \rightarrow$ gas phase	Polycrystalline spinel layer formed; CoO single crystal and spinel layer exhibited porosity after experiment; markers not discussed; structure supports the proposed mechanism	Sockel[26]
$ZnCr_2O_4$	Zn^2 and Cr^3 diffusion through spinel measured and compared with $ZnCr_2O_4$ formation rates	$Zn^{2+} \rightarrow$ $Cr^{3+} \leftarrow$	Activation energies for Cr^{3+} and Zn^{2+} diffusion through the spinel layer were identical to activation energy for spinel growth	Lindner and Akerstrom[9]
$MgCr_2O_4$	Reacted MgO single crystals with Cr_2O_3 polycrystals in air	$Mg^{2+} \rightarrow$ $Cr^{3+} \leftarrow$ vapor phase transport of Cr_2O_3 to spinel surface	Single crystal spinel layer formed, bonded to MgO; structure does not confirm the indicated mechanism	Sockel[26]

transfer of chromium from the spinel pellet to the nickel oxide pellet was demonstrated. Hauffe and Pschera concluded that vapor phase transport of chromium was characteristic of pellets in good contact or in poor contact. However, this conclusion should be viewed with caution, because the oxide pellets used by these authors were probably very porous. They presented no density measurements, but their pellet fabrication process (cold pressing and sintering for 2 hours at 1100°C) would not produce high pellet densities. Therefore, vapor phase transport would be expected in experiments with or without a spacer. Although Hauffe and Pschera did show that vapor transport could be important in the movement of chromium ions from chromium oxide to the spinel surface, they presented no data on the growth of the spinel layer itself, and simply assumed that the Wagner mechanism controlled its growth.

Lindner and Akerstrom[9,11,12] measured the diffusion coefficients of Ni^{2+} and Cr^{3+} in nickel chromite as well as the parabolic reaction rate constant. They found that the diffusivities of Ni^{2+} and Cr^{3+} were essentially the same. In addition, the theoretical diffusion coefficients (calculated from the reaction rate constant on the basis of inverse cation diffusion) were within a factor of 2 of the measured diffusion coefficients. On the basis of these results, they concluded that the Wagner mechanism controlled the spinel growth rate. Attempts to verify this mechanism with platinum marker experiments were unsuccessful because "the platinum markers were attacked by the oxides mainly chromium oxides."[9] No further explanations were made of the marker phenomenon. As with the specimens of Hauffe and Pschera,[28] the pellets used in these experiments were very porous. Lindner et al.[9] did not report the densities of the single oxide pellets used for spinel growth measurements, but they did report that the nickel chromite pellets used in their diffusion studies were about 55% of theoretical density. Consequently, the probability that vapor phase

transport influenced the diffusion measurements (particularly for Cr^{3+}) is high. The same can be said for the Cr^{3+} diffusion data of Morkel and Schmalzried,[10] in which the nickel chromite pellets were less than 70% of theoretical density.

Schmalzried[21] disagreed with the conclusions of Lindner et al.[9] that they had confirmed the controlling role of the Wagner mechanism in nickel chromite formation. He argued that the porosity of the starting oxides would allow transport of oxygen through the vapor phase, and transport of Ni^{2+} or Cr^{3+} and electrons through the spinel layer. This mechanism would result in the same theoretical parabolic rate constant as calculated by Lindner et al.,[9] because the diffusion coefficients of Ni^{2+} and Cr^{3+} are the same order of magnitude. Schmalzried concluded that further marker studies were necessary with the nickel chromite system. He attempted marker experiments with nickel chromite, but reported that the platinum wires dissolved during the high temperature reaction.[21]

Sockel[26] attempted to use the "natural marker" technique which had been successful in confirming the reaction mechanism in aluminates.[25,26] He reacted single crystals of NiO and polycrystals of chromium oxide. X-ray diffraction and optical studies of the nickel chromite reaction layer revealed that it was pore free and single crystalline. He further reported that the spinel layer was bonded to the nickel oxide. These results were insufficient to prove any mechanism.

Sockel also measured the parabolic rate constant for nickel chromite growth, and compared it with a theoretical value based on the Wagner mechanism. The two values were identical, and he concluded that the nickel chromite formation was controlled by inverse diffusion of Ni^{2+} and Cr^{3+}. No explanation of the single crystal structure of the spinel layer was given.

Schmalzried attempted to determine the mechanism of cobalt chromite spinel formation by reacting pellets of cobalt oxide and chromium oxide (with platinum markers at the reaction interfaces) in air and in oxygen-free nitrogen. After the reactions in air, the platinum markers were found at the cobalt oxide/cobalt chromite interface (thus indicating transport of Co^{2+} and electrons through the spinel, and oxygen through the gas phase). The platinum markers could not be found after the nitrogen experiments, and were presumed to have dissolved. The experimental reaction-rate constant for reactions in air compared reasonably well with the theoretical values (assuming the rate was controlled by Co^{2+} diffusion through the spinel layer). The experimental rate constant for spinel grown in nitrogen was 1/2 to 1/3 the constant measured for the air experiments, and about twice the theoretical value for inverse cation diffusion of Co^{2+} and Cr^{3+}. On this basis Schmalzried concluded that the growth of cobalt chromite in air is controlled by Co^{2+} and electron (or electron hole) diffusion through the spinel layer and oxygen transport through the gas phase. Support for the electronic contribution to this reaction mechanism was obtained by independent conductivity measurements.[29] At temperatures greater than 1000°C, cobalt chromite was shown to be a p-type conductor at high oxygen partial pressures ($>10^{-8}$) and an n-type conductor at low oxygen partial pressures ($\leq 10^{-8}$). Schmalzried also concluded that the reaction mechanism for cobalt chromite growth in an oxygen-free atmosphere would be countercurrent diffusion of Co^{2+} and Cr^{3+}.

Sockel[26] reacted single crystals of CoO with polycrystals of Cr_2O_3 in an attempt to define the reaction mechanism. The spinel layer (grown in air) was found to be a textured polycrystal bonded to the cobalt oxide single crystal. Sockel reported that the single crystal CoO and the polycrystalline spinel layer had a porous structure. He therefore concluded that the reaction mechanism consisted of countercurrent diffusion of Co^{2+} ions and electron holes through the spinel with concurrent vapor transport of oxygen

(through pores in the single crystal and spinel) to the CoO/Cr_2O_3 interface. He reported that the theoretical and experimental rate constants for this mechanism agreed within a factor of 2, and cited Schmalzried's[21] marker studies as confirmation of the mechanism.

Zinc chromite and magnesium chromite formation has been studied by Lindner and Akerstrom[9] and Sockel,[26] respectively. Lindner etal.[9] compared the activation energy for diffusion of Zn^{2+} and Cr^{3+} with the activation energy for spinel formation. Since these two values were identical, they concluded that the reaction mechanism was countercurrent cation diffusion. Sockel reacted single crystal MgO with polycrystalline chromium oxide. A dense single crystal spinel layer was formed which was bonded to the magnesium oxide but not the chromium oxide. The single-crystal spinel structure was explained on the basis of vapor phase transport of chromium oxide to the surface of the magnesium oxide, and epitaxial single crystal growth of magnesium chromite. The epitaxial growth of the spinel crystal continued by inverse cation diffusion.

In summary, it is apparent that inverse cation diffusion is favored by most authors as the mechanism by which chromite spinels form. Quite often, however, conflicting experimental results are rationalized away. For example, the single crystal/polycrystal reactions that convincingly support the Wagner mechanism in nickel aluminate and cobalt aluminate formation,[25,26] do not support this mechanism in nickel chromite, cobalt chromite, and magnesium chromite formation. The cobalt chromite spinel is totally polycrystalline, whereas the nickel and magnesium chromites are single crystals. If the Wagner mechanism (or the experimental adequacy of single crystal/polycrystal interface markers) applies, special arguments are needed to explain the epitaxial growth of nickel and magnesium chromites. In cobalt chromite formation, the polycrystalline structure of the spinel could be explained by vapor phase transport of chromium oxide to the cobalt oxide single crystal interface to form a polycrystalline cobalt

chromite, and countercurrent diffusion of Co^{2+} and Cr^{3+} thereafter. However, Schmalzried concludes that the structure results from countercurrent diffusion of Co^{2+} and electron holes with simultaneous oxygen transport through the gas phase. The probable explanation of many of these inconsistencies lies in the nucleation process of the spinel phase.[22] If nucleation processes are important, it seems clear that the use of single crystal/polycrystal interface markers will provide conclusive evidence of a given reaction mechanism only in very special circumstances. In the chromite systems, therefore, there is certainly room for further study with other experimental techniques. One feature that is definitely needed is the use of high density starting materials. Such materials will minimize vapor transport pheonomena and may provide new information on the reaction mechanisms in these systems.

III EXPERIMENTAL PROCEDURES

Because of the possible complications arising from vapor phase transport in porous oxides, it was decided that one of the major efforts of this work would be to utilize oxides of high density. In addition, since the influence of impurity additions was to be evaluated, it was necessary to utilize oxides of the highest purity in order to obtain reference data for comparison.

A. Oxide Preparation

Techniques for the preparation of high-purity oxides generally consist of purification and thermal decomposition of nitrates, sulfates, carbonates, hydroxides, or oxalates of the desired oxides.[30-34] Of the various methods reported, only the oxalate decomposition method of Brown[33,34] had been reported to yield calcium and magnesium oxides of high purity (99.999%) which would also sinter to high density after simple cold-pressing and sintering. Similar procedures were therefore used to prepare the high-purity and manganese-doped oxides used in this study. Only regeant grade chemicals, whose purity levels are shown in Table 9, were used to prepare the oxides. Approximately 2 gm mol wt of either nickel or cobalt-nitrate-hexahydrate were dissolved in 2.5 liters of boiling distilled water. A boiling solution of 3 gm mol wt of oxalic acid in 2 liters of distilled water was also prepared. The solutions were purified by pre-precipitation of the starting solutions followed by filtration. The oxalic acid was purified by adding 50 ml of the nitrate solution to the boiling oxalic acid to precipitate insoluble impurity oxalates along with the nickel or cobalt oxalates. The precipitate was allowed to settle, and the solution was filtered through a Whatman No. 54 filter paper. The nitrate solutions were purified in a similar manner by adding 50 ml of the purified oxalic acid solution to the boiling nitrates and filtering. The final oxalates were prepared by mixing the hot purified nitrate and oxalic acid solutions, filtering,

TABLE 9

PURITY LEVELS OF STARTING REGEANTS USED IN OXIDE PREPARATION

Compound	Source	Impurity levels, ppm by wt										Purity Level, %
		Cl	NH_4	SO_4	Pb	Cu	Fe	Zn	Co	Ni	Other	
$Ni(NO_3)_2.6H_2O$	J. T. Baker Chemical Co. Analyzed Reagent	5	200	20	1	15	10	50	100	-	400	99.9
$Co(NO_3)_2.6H_2O$	J. T. Baker Chemical Co. Analyzed Regeant	20	500	20	10	10	5	50		500	400	99.8
$Mn(NO_3)_2$ (52% Solution)	J. T. Baker Chemical Co. Analyzed Reagent	5	-	50	10	-	3	100	-	-	750	99.9
$HC_2O_4.2H_2O$	J. T. Baker Chemical Co. Analyzed Reagent	20	-	20	5	10	2	-	-	-	300	99.9
$Si(OC_2H_5)4$	Eastman Organic Chemicals	-	-	-	-	-	-	-	-	-	-	99.9
NH_4OH 30% Solution	Allied Chemical Co. Regeant Grade	5	-	1	5	-	1	-	-	-	20	99.99

multiple washing with boiling distilled water, and drying. Nickel manganese and cobalt manganese oxalates were prepared by adding manganese nitrate to the purified nickel or cobalt nitrate solutions and precipitating with purified oxalic acid. Oxides were then prepared by reacting 15 gm batches of the pure or manganese-doped oxalates for 30 min at 450°C in a flowing stream (50 ml/min) of oxygen.

Doping of the nickel and cobalt oxides with silicon oxide could not be done by the same method as the manganese oxide doping, because silicon nitrates are not available. Since it was necessary to have a uniform distribution of silicon in the oxides, a precipitation technique was desirable. Blending of oxides of nickel or cobalt with silicon oxide was undesirable because of the low (1 mole % SiO_2) doping levels required and because of the possibility of contamination. The method finally selected was a compromise between the precipitation and the powder blending techniques. Slurries of high-purity nickel or cobalt oxides (prepared by oxalate decomposition) were prepared using a 30% solution of reagent grade ammonium hydroxide. The oxides were kept in suspension by continuous stirring, and a 50% excess of the required amount of high-purity tetraethyl orthosilicate was added. Since the reaction of the orthosilicate with ammonia to form an insoluble ammonium silicate is very slow,* the reaction was allowed to proceed for 24 hours with continuous stirring. The slurries were then filtered through a Whatman No. 54 filter paper, washed with distilled water, and dried. In preliminary experiments it was observed that the filtrate contained some insoluble silicate in suspension. This observation indicated that the precipitate formed was very fine, and was likely to be uniformly distributed in the oxide. The

---

* In preliminary experiments with pure ammonium hydroxide and tetraethyl orthosilicate, no reaction product could be seen in solution for 2 hours after the initial mixing; 16 hours after mixing a white precipitate was clearly visible.

50% excess orthosilicate addition mentioned above was used to compensate for the silicate losses in the filtrate.

All chromium oxide used in these studies consisted of commercially available reagent grade Cr_2O_3. No doping experiments were made on the chromium oxides. Preliminary attempts to prepare chromium oxide by the precipitation of chromium hydroxide from purified chromium nitrate solution were successful. However, chemical analyses revealed little, if any, difference between the purity of the commercial powder and the powder prepared in the laboratory. Therefore, the commercial chromium oxide was used, since it was available in large quantities.

B. Pellet Preparation

Pellets of high-purity, manganese-doped, and silicon-doped nickel and cobalt oxides (1 in. diameter) were prepared by cold pressing (using distilled water as a binder) at 20,000 lb/in.^{2}, drying at 80°C, and firing in air at 1500°C for 250 to 350 hours. Contamination was minimized by firing each set of pellets in separate alumina furnace tubes, and by placing each pellet on a 0.125 mm thick platinum foil. After initial firing, groups of pellets of each type were equilibrated with air at 1200, 1300, and 1400°C in order to provide starting oxides for experiments to be made at such temperatures. The same precautions of firing in separate furnace tubes and use of platinum foil between the oxides and the alumina support plates were used in the equilibration procedures to minimize contamination.

Early experiments revealed that simple cold pressing and sintering procedures were not suitable for the preparation of high density chromium oxide pellets. For example, after sintering procedures similar to those used for the nickel and cobalt oxides, the chromium oxide pellets were very fragile and readily absorbed water. Consequently a hot pressing procedure was used. Pellets of chromium oxide (2 in. diameter) were prepared by hot-pressing for one hour at 1450°C. Hot pressing was done with induction-heated graphite dies at a pressure of 4000 lb/in.^{2}.

After pressing, the pellets were removed and fired for 250 to 350 hours at 1500°C. Groups of chromium oxide pellets were then equilibrated with air by firing for 100 hours at 1200, 1300, and 1400°C. The same precautions were taken to prevent the contamination of the chromium oxides as with the nickel and cobalt oxides. In addition to the studies using the polycrystalline oxides described, a limited number of experiments were made with single crystals of nickel oxide, cobalt oxide, and chromium oxide. These crystals (grown by the Verneuil process using arc-image furnaces) were obtained from sources listed in Table 10.

C. Spinel Reactions

The following procedures were closely followed for most spinel formation experiments. Those experiments in which the procedure varied will be described separately. Pellets for reaction at a given temperature were selected from groups that had previously been equilibrated at or near the desired temperature. Pellets were selected on the basis of density and freedom from obvious flaws, such as cracks. Pellets were then ground flat on a cast iron metallographic wheel using progressively finer diamond paste ranging from 30 to 1 μ. A final light polishing on a satin-covered wheel with 1 μ diamond paste completed the surface preparation. Pellets were then halved or quartered, as desired, to obtain several specimens.

Three types of markers were used in these studies: (a) thick platinum foils (6 μ by 1 mm by 1 cm), (b) thin platinum foils (1.5 μ by 1 mm by 1 cm), and (c) iridium powder approximately 0.1 to 1 μ diameter. Before reactions, the markers were carefully placed between the pellets, and their locations were indicated by notches on the pellets. This precaution was necessary, because the markers that extended beyond the pellet interfaces and that were exposed to the air were generally gone after the spinel reaction procedures. Consequently, without the notches it would have been difficult to mount the specimens properly to find the markers.

The assembled specimens with markers were then placed in silicon carbide heated muffle furnaces capable of temperatures to 1550°C. Platinum foils 0.125 mm thick were placed between the specimens and the alumina support plates in order to minimize contamination and sticking. Alumina blocks were then placed on top of each specimen to produce a compressive stress of approximately 1 kg/cm^2. The furnaces were then rapidly heated to the desired reaction temperature. In general the time required to reach the reaction temperature was less than 10 hours. Of this time, approximately 5-7 hours were required to reach the temperature of 1100°C. Since all experiments reported here were done at temperatures of 1200 to 1550°C for times ranging from 24 hours (at the highest temperatures) to 640 hours (at the lowest temperatures), this procedure was felt to be adequate and the heat-up time to be negligible. All experiments were done in air, and temperatures were measured with two Pt + Pt-10%Rh thermocouples obtained from separate sources. Temperatures measured with both thermocouples were always within ±5°C of each other, and the temperatures remained within ±10°C of the reported value during each experiment.

After the desired reaction time, the doors of the muffle furnace were opened and the specimens were moved to a cooler part of the furnace. The specimens were removed from the furnace after they had cooled to less than a red heat. The entire cooling process generally took about 1 hour. More rapid cooling resulted in fracture of the specimens by thermal shock. Some specimens were furnace cooled by simply shutting off the furnace power. In these operations, cooling to room temperature required times of approximately 48 hours. Furnace cooling to temperatures of 100°C, however, generally took about 6 hours.

In some of the short-time, high-temperature experiments, specimens were cut from pellets that had previously been reacted. These specimens therefore contained an initial thin spinel layer. Consequently, slightly different procedures were necessary to evaluate rate constants from the measured spinel thicknesses after the final firing. No previously bonded specimen was used for subsequent spinel reactions unless it was free from

cracks or flaws, had been fired at a temperature at least 200°C lower than the planned firing temperature, and contained a spinel layer that would be 2 to 3 times thinner than the estimated thickness produced by the high temperature reaction. The time required to form the thick high-temperature spinel layer was estimated from previous kinetic data.[9,21]

D. Metallographic Examination

After removal from the furnaces, the specimens were carefully mounted in either a cold-setting epoxy or a thermo-setting bakelite. Special grinding and polishing procedures were necessary in order to prepare a satisfactory surface. Because of the high hardness of the dense chromium oxide and the low hardness of the nickel and cobalt oxides, all grinding was done with 30 μ diamond on a cast iron grinding lap. Grinding with coarser silicon-carbide abrasives severely damaged the softer oxides. Final polishing was done with 6, 3, and 1 μ diamond compounds on a satin-covered brass wheel. The best specimen finishes were obtained by final polishing for 7 to 10 days on an automatic vibratory polisher with 1 μ diamond paste. Because of the large differences in hardness between the starting oxides, this procedure produced a certain amount of relief polishing, but the relief polishing did not prove to be a significant problem. The spinel thicknesses were measured with either a Unitron measuring microscope or a Leitz metallograph and filar eyepiece. The Unitron microscope (capable of readings to 2.5×10^{-4} cm) was used for measurements on thick spinel layers, while the Leitz metallograph with oil immersion lens and filar eyepiece (capable of readings to 7×10^{-6} cm) was used for the thin spinel layers. Both microscopes were calibrated with a Leitz standard.

E. X-ray and Electron Microprobe

The phases in the oxides prepared by the techniques described above were identified by standard X-ray diffraction techniques.

Electron microprobe studies were made to determine the distribution of elements in the starting oxides and in the spinels grown from these oxides. Two different instruments were used. One instrument, whose design and construction has previously been described,[35] was used for the point counting data reported. A Materials Analysis Model 400S microprobe was used for scanning, electron backscatter photographs, and X-ray image photographs. All microprobe data were taken using beam diameters ranging from 1 to 10 μ and accelerating voltages of 20 to 25 kv. Internal standard (from the unreacted nickel, cobalt, and chromium oxides and from the nickel and cobalt chromites formed by reaction) were used to convert the intensity data to composition data. No other corrections were made.

IV RESULTS

A. Compositions, Densities, and Structures of Starting Oxides

The compositions and densities of the oxides used are shown in Table 10. The oxides prepared by oxalate precipitation and decomposition were of somewhat higher purity than commercial reagent grade oxides. Oxides prepared by the oxalate procedure were approximately 99.98% pure (in contrast to the 99.999% purity reported by Brown[33,34] for calcium and magnesium oxides prepared by a similar method), while oxides obtained from commercial sources were approximately 99.9% pure. The major impurities (which were not deliberately added) in the nickel and cobalt oxides were cobalt and nickel, respectively. The resultant manganese oxide dopant concentrations in both the nickel and cobalt oxides were very close to the desired 1 mole % values. The resultant silicon oxide concentrations, however, were approximately 50% higher than the desired 1 mole %. This higher concentration resulted from the addition of the 50% excess tetraethyl orthosilicate in the silicate precipitation procedure. Apparently the amount of silicate lost in the filtration step was insignificant and need not have been compensated.

The densities* of all the nickel oxides prepared by cold pressing and firing ranged from 92 to 97% of theoretical density. These values were based on a theoretical density of 6.808 for nickel oxide. However, the measured density of flaw-free single crystal nickel oxide was found to be only 98% of this theoretical value. Consequently the densities listed in Table 10 for the nickel oxides can be considered minimum values, since the use of the measured single crystal density of 6.67 would increase the relative densities of all pellets by 1 to 2 %.

---

* All densities were measured by pycnometric techniques; distilled water was used as the immersion medium.

TABLE 10

PURITIES AND DENSITIES OF STARTING OXIDES

Material	Source	Metallic Impurity Concentrations,* ppm by wt							Dopant, mole %	Purity Level, wt %	Average Density	
		Co	Ni	Si	Mn	Cu	Fe	Co + Zn + Mg + Cd			gm/cm^3	% theoret.**
NiO, regeant grade	J. T. Baker Chemical Co. "Analyzed Reagent"	450	M	ND	ND	30	50	470	None	99.90	6.38	94
NiO, high purity	Prepared by oxalate precipitation	100	M	ND	ND	30	ND	50	None	99.98	6.45	95
NiO-1MnO	Prepared by oxalate precipitation	100	M	ND	7200	10	ND	50	0.97 MnO	98.26	6.40	94
NiO-1SiO_2	Prepared by oxalate precipitation	100	M	3500	ND	20	ND	50	1.45 SiO_2	98.63	6.49	95.5
NiO, single crystal	Argonne National Lab. Argonne, Ill.	190	M	10	30	30	60	60	None	99.96	6.67	98
CoO, high purity	Prepared by oxalate precipitation	M	400	ND	100	ND	ND	100	None	99.94	5.90	91
CoO-1MnO	Prepared by oxalate precipitation	M	400	ND	8400	ND	ND	100	1.14 MnO	98.11	5.94	92
CoO-1SiO_2	Prepared by oxalate precipitation	M	300	5650	50	ND	ND	200	1.51 SiO_2	98.38	5.84	91
CoO, single crystal	Argonne National Lab. Argonne, Ill.	M	600	ND	ND	ND	ND	200	None	99.92	6.47	99.8
Cr_2O_3, reagent grade	Fisher Scientific Co. "Certified Reagent"	ND	ND	250	ND	20	250	200	None	99.93	5.15	99
Cr_2O_3, single crystal	Adolph Meller Co. P. O. Box 6001 Providence, R. I.	ND	ND	150	ND	50	300	300	None	99.9	5.20	100

* ND, not detected; M, major constituent. Determined by spectrographic analysis.

** Based on the following theoretical densities: NiO, 6.808 gm/cm^3; CoO, 6.49 gm/cm^3; Cr_2O_3, 5.202 gm/cm^3.

Similar comments cannot be made for the cobalt oxides, which have only 91-92% of the theoretical density of CoO ($p = 6.49\ gm/cm^3$). A flaw-free single crystal of CoO was 99.8% dense. The amount of precipitation of Co_3O_4 ($\rho = 6.08\ gm/cm^3$) from the monoxide during cooling was far greater in the pressed and sintered polycrystals than in the single crystals. Consequently the relative densities given in Table 10 for the cobalt oxides are conservative and represent minimum values.

The densities obtained with hot pressed chromium oxide were always within 98% of theoretical density. In addition, the densities of the outside surfaces of these pellets were higher than the overall density. In general, all spinel reactions were made with chromium oxides approaching 100% of theoretical density. This statement is supported by the microstructure of the hot pressed and equilibrated Cr_2O_3 shown in Figure 3. It should be emphasized here that the dense equiaxed structure of this (and other) oxides is evident only after prolonged and careful polishing. Rapid polishing will create as much surface damage as it removes, thus obscuring the true structure of the oxides.

The structures of the pure and the manganese-doped nickel oxides cannot be seen in the polished specimens, since the materials are optically isotropic. Consequently, it was necessary to etch the nickel oxide with boiling nitric acid to reveal the grain structure shown in Fig. 4a. Unfortunately, this procedure produces etch-pitting and faceting of the individual grains. A second method of revealing the structure of the nickel oxide consists of diffusing chromium into the nickel oxide at high temperatures (1300-1550°C), then furnace cooling and polishing. This process precipitates nickel chromite spinel in a Widmanstatten pattern in each grain of the nickel oxide. The individual nickel oxide grains shown in Figure 4b are thus revealed by the differences in orientation of the spinel precipitates. A confirmation of these statements will be presented in a later section of this dissertation. It is evident by both techniques that the nickel oxide is

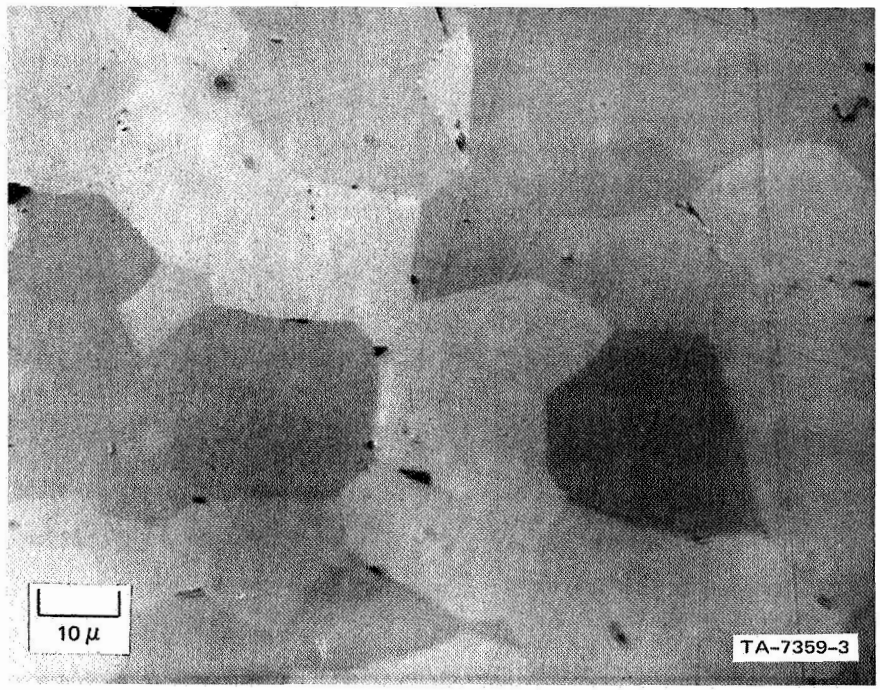

FIGURE 3 STRUCTURE OF HOT-PRESSED AND HEAT-TREATED CHROMIUM OXIDE

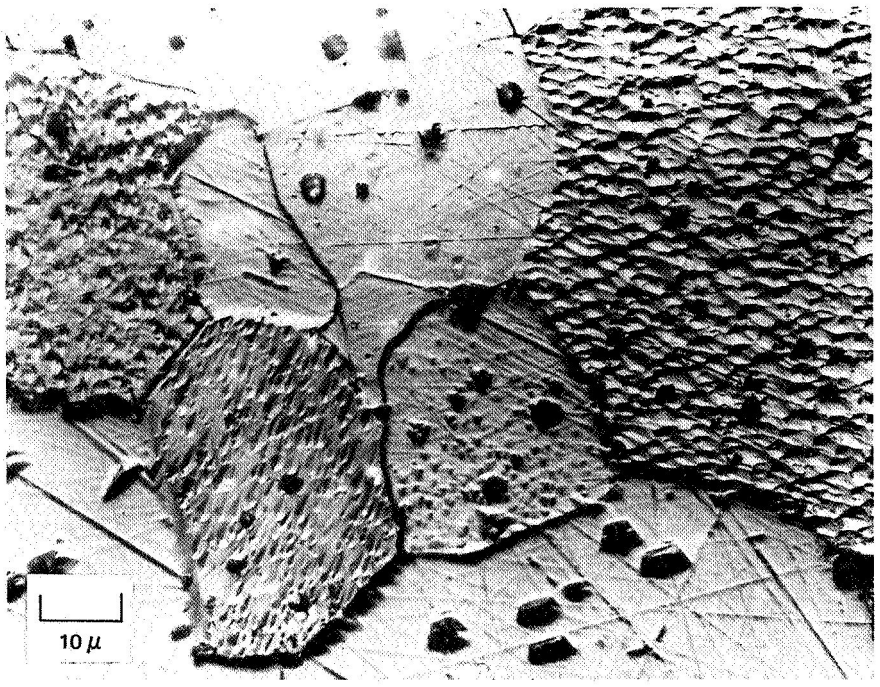

(a)

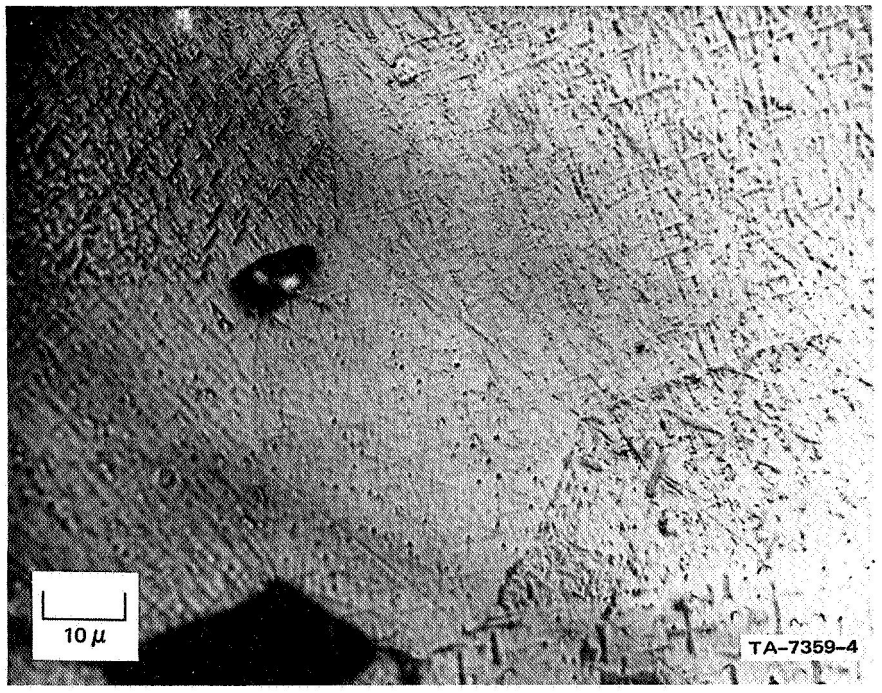

(b)

FIGURE 4 STRUCTURE OF NICKEL OXIDE: (a) Cold-pressed and sintered high purity NiO; pitted and faceted structure results from etching in boiling nitric acid. (b) Doped with chromium oxide during spinel formation; the precipitates are nickel chromite, and emphasize the dense structure.

reasonably dense. The structure of the nickel oxide doped with 1.5 mole % silicon oxide is shown in Fig. 5. The electron backscatter micrograph shows that the silica additions produce precipitation of a second phase in the nickel oxide. X-ray diffraction measurements of the polished pellets confirmed that the second phase is nickel silicate (Ni_2SiO_4). Electron microprobe measurements using Si Kα X-ray images (Fig. 5b) showed that most if not all of the silicon is concentrated in the silicate phase.

The microstructure of the pure or the manganese-doped cobalt oxide was revealed in the as-polished condition by the precipitation of the cobalt spinel, Co_3O_4 (Fig. 6a). Precipitation of the spinel occurs along high angle grain boundaries, sub-grain boundaries, and sometimes within the grains as Widmanstatten platelets. There was no observed precipitation of manganese in the doped cobalt oxides, and none was expected in view of the mutual solubilities of manganese and cobalt oxides. The microstructure of the silica-doped cobalt oxide (Fig. 6b) consisted of large grains of dense CoO containing precipitates of Co_3O_4 in the grain boundaries and within the grains, and a silicate phase in the grain boundaries. X-ray diffraction measurements revealed the presence of cobalt silicate (Co_2SiO_4), CoO, and Co_3O_4 in these oxides. Electron microprobe measurements utilizing electron backscatter images (Fig. 7a,b) and Si Kα X-ray images confirmed that the grain boundary precipitates were silicates, and that little or no silicon remained in solid solution in the cobalt oxide.

B. Nickel-Chromite Formation From Pure Oxides

The observations to be discussed in this section apply to the spinel formation from the reaction of reagent-grade chromium oxide with both reagent-grade and high-purity nickel oxide. For ease of presentation, the surface effects and the internal effects will be described separately.

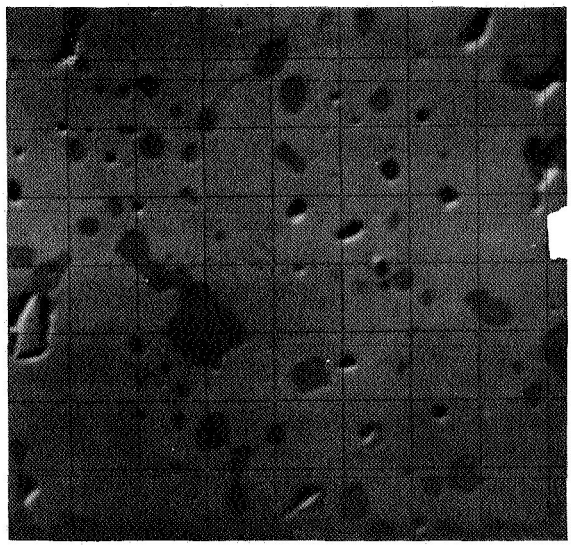

(a) ELECTRON BACKSCATTER IMAGE

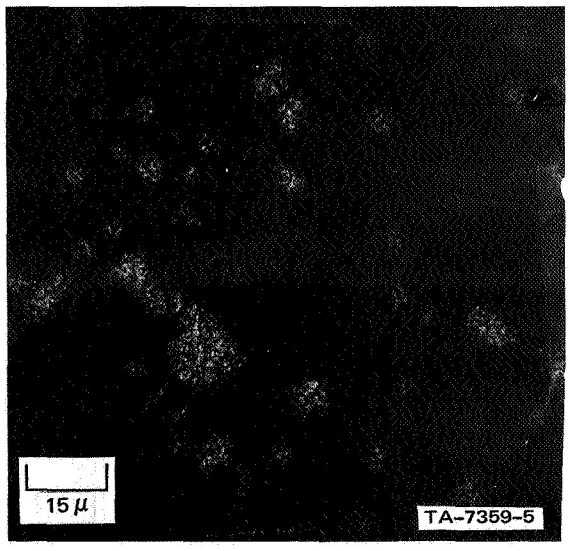

(b) Si Kα X-RAY IMAGE

FIGURE 5 STRUCTURE AND COMPOSITION OF NICKEL OXIDE DOPED WITH 1.5 MOLE % SILICON OXIDE. Second phase is Ni_2SiO_4.

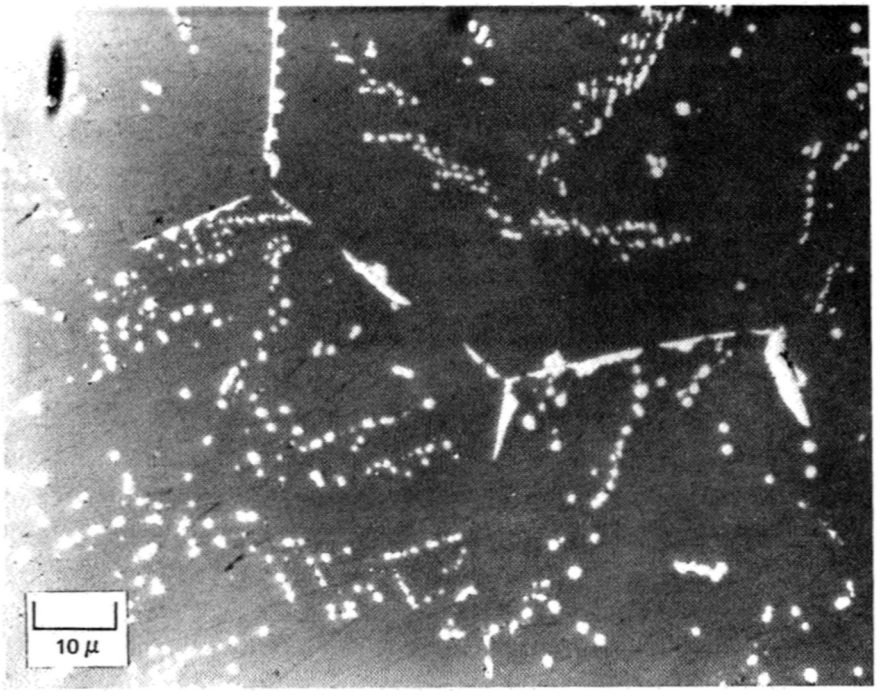

(a)

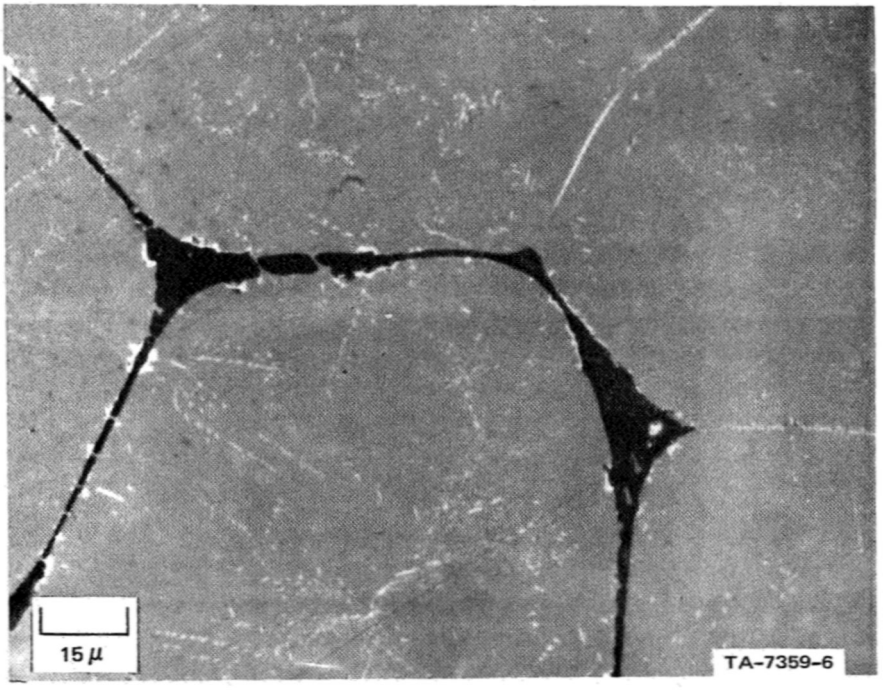

(b)

FIGURE 6 STRUCTURE OF HIGH-PURITY AND SILICON-DOPED COBALT OXIDE:
(a) High purity; grey matrix is CoO, white precipitate is Co_3O_4;
(b) Silicon-doped; grey matrix is CoO, dark grain boundary phase is Co_2SiO_4

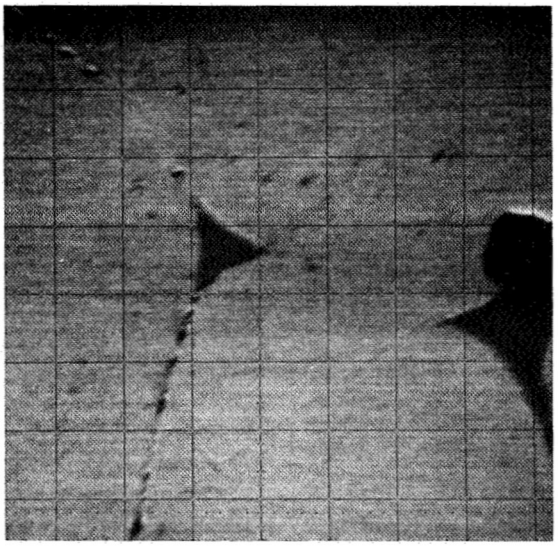

(a)

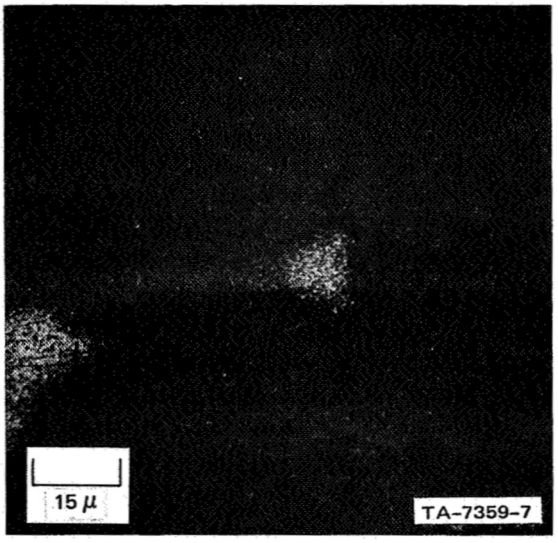

(b)

FIGURE 7 STRUCTURE OF $CoO\text{-}1SiO_2$ PELLET: (a) Electron backscatter image; (b) X-ray image photograph of Si Kα radiation from same area as in (a).

1. Surface Features

During early experiments, the chromium oxide pellets appeard to shrink during the spinel reaction anneals. Details of this shrinkage were determined by cutting pre-bonded pellets into small rectangular prisms and firing at temperatures from 1200 to 1500°C. All such specimens took the shape shown in Fig. 8a after firing, the most pronounced shape changes occurring at the highest temperatures and longest times. The initial shape of the specimen is shown by the dashed lines. The nickel oxide half of the specimen expanded, the maximum expansion occurring near the reaction interface. Some of this expansion, however, could be accounted for by surface formation of nickel chromite spinel on the nickel oxide from the vapor phase. This formation will be discussed in greater detail in a later section. As is shown, the chromium oxide half of the specimen underwent a severe non-uniform shrinkage, the maximum shrinkage occurring near the reaction interface.

Examination of the surface of the reaction interface in greater detail revealed the structures shown in Fig. 8b. The predominant features of the interface were the spinel crystals on the surface of the nickel oxide, and the small crystallites formed on the surface of the spinel. These crystallites were not strongly bonded to the spinel and could easily be brushed off. Examination at higher magnifications (Fig. 9b) showed prominent growth steps and fine cracks in the spinel crystals. This cracking was found to be a general occurrence in both the spinel phase and the chromium oxide phase. The crystallites formed on the surface of the spinel were small octahedrons (Fig. 9c) and were identified as nickel chromite by X-ray diffraction. In addition to these features, small crystallites, resembling etch pits (Fig. 9a), formed on the surfaces on the nickel oxide during the spinel reaction. These crystallites appeared to form preferentially on cube faces of the nickel oxide crystals, and along what appeared to be subgrain boundaries. The amount of crystallite formation on the nickel oxide decreased as the distance from the reaction interface increased.

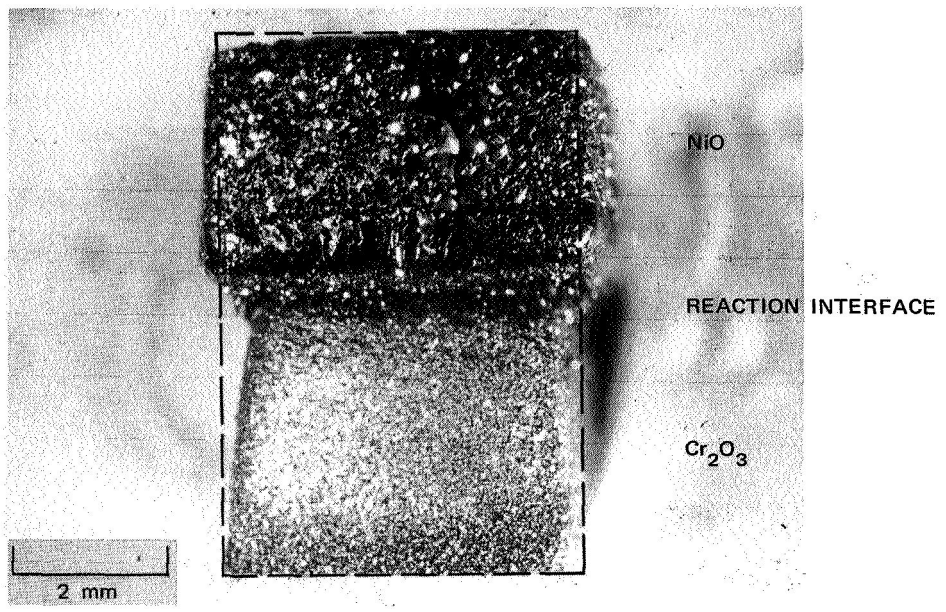

(a)

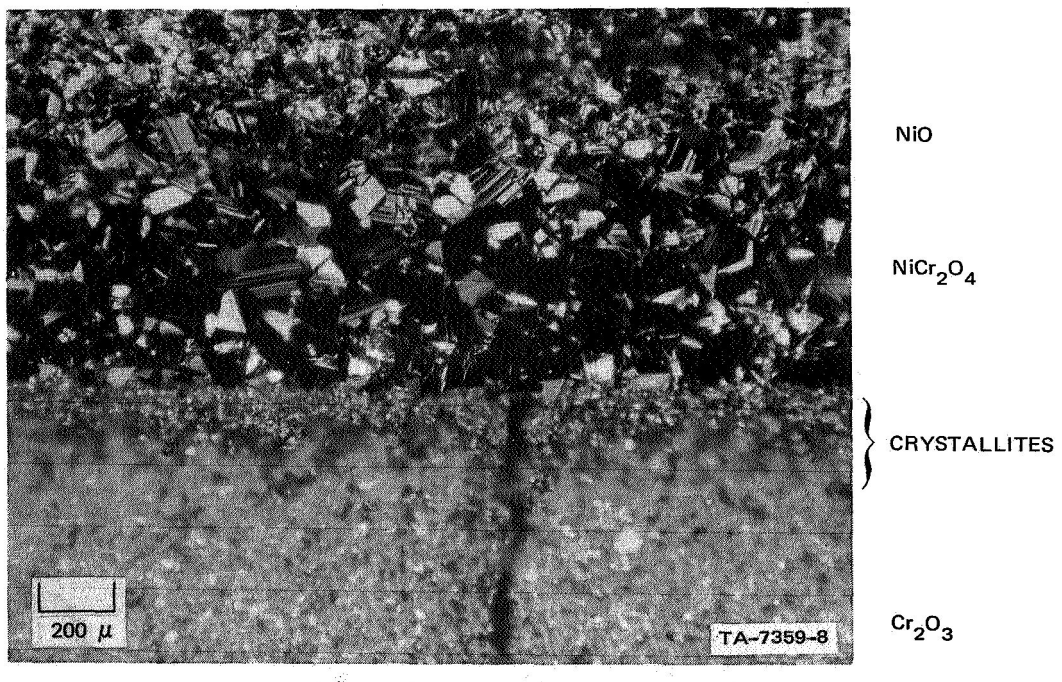

(b)

FIGURE 8 NICKEL OXIDE/CHROMIUM OXIDE DIFFUSION COUPLE: (a) Macrostructure showing non-uniform shrinkage of chromium oxide; (b) details of surface at reaction interface.

(a)

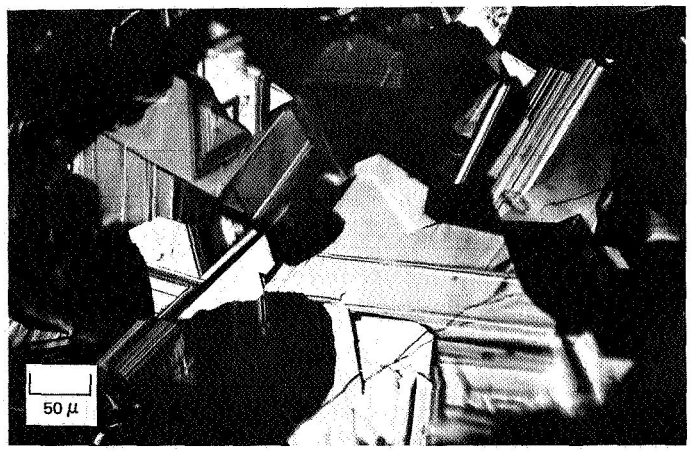

(b)

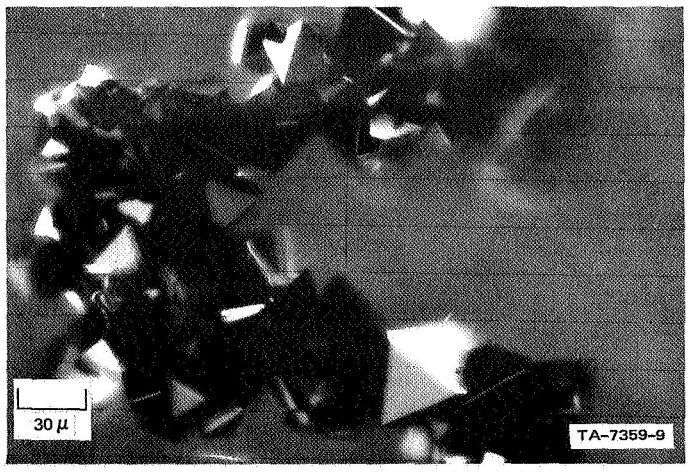

(c)

FIGURE 9 DETAILS OF THE NICKEL OXIDE/CHROMIUM OXIDE INTERFACE: (a) Nickel oxide crystals near reaction interface showing spinel nucleation; (b) surface structure of nickel chromite showing growth steps and cracks; (c) octahedral crystallites formed at the surface of the reaction interface.

Figure 10 shows that no such crystallite formation was ever observed on the surfaces of nickel oxides that had been fired in the absence of chromium oxide. These observations suggest that the crystallites on the surface of the nickel oxide may be the first stages of nickel chromite spinel formation by a solid NiO-"vapor" Cr_2O_3 mechanism. The spinel crystallites on the surface of the large-grained spinel probably form by a vapor phase reaction of both nickel and chromium oxides.

2. Internal Features

Characteristics of the internal features of nickel-chromite spinel formation are summarized schematically in Fig. 11, and examples of some of these features are shown in Figs. 12-15. The thickness of the spinel formed during a given diffusion anneal varied considerably depending on the location within the specimen. At the surface of the reaction interface (location A in Fig. 11), the spinel was very thick. This thick layer rapidly decreased to a very thin layer inside the dense, crack-free regions of the specimen (location B in Fig. 11). Thick spinel layers also formed at internal cracks exposed to air (location D). These internal layers could either be thicker or thinner than the surface layers, depending on the geometry of the crack. An example of the thickness of the surface and the internal spinel layers is shown in Fig. 12. Also shown in Fig. 12 is the cracking of the chromium oxide pellet near the reaction interface. Cracking of the specimens parallel to the reaction interface was also observed in the spinel and the nickel oxide, but the cracking of the dense chromium oxide was most common. This cracking did not extend across the specimen, and the pellets were generally well bonded. Only in one special experiment was easy separation of the reactants after the diffusion anneal observed, although easy separation has been described as a common occurrence by Hauffe and Pschera,[28] Schmalzried,[21] and Sockel.[26] The details of this experiment and its implications in the

REAGENT-GRADE
NiO

HIGH-PURITY
NiO

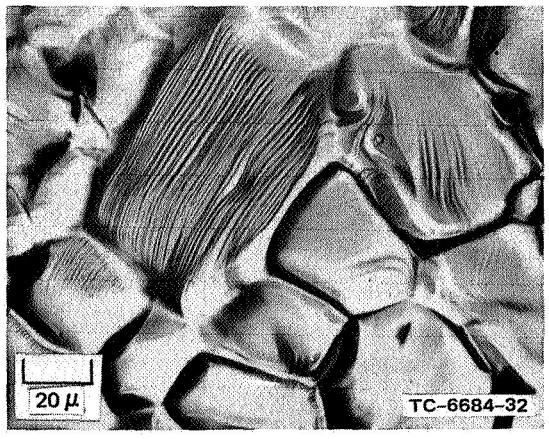

HIGH-PURITY
NiO – lm/o Mno

FIGURE 10 SURFACE STRUCTURES OF VARIOUS NICKEL OXIDE PELLETS AFTER FIRING

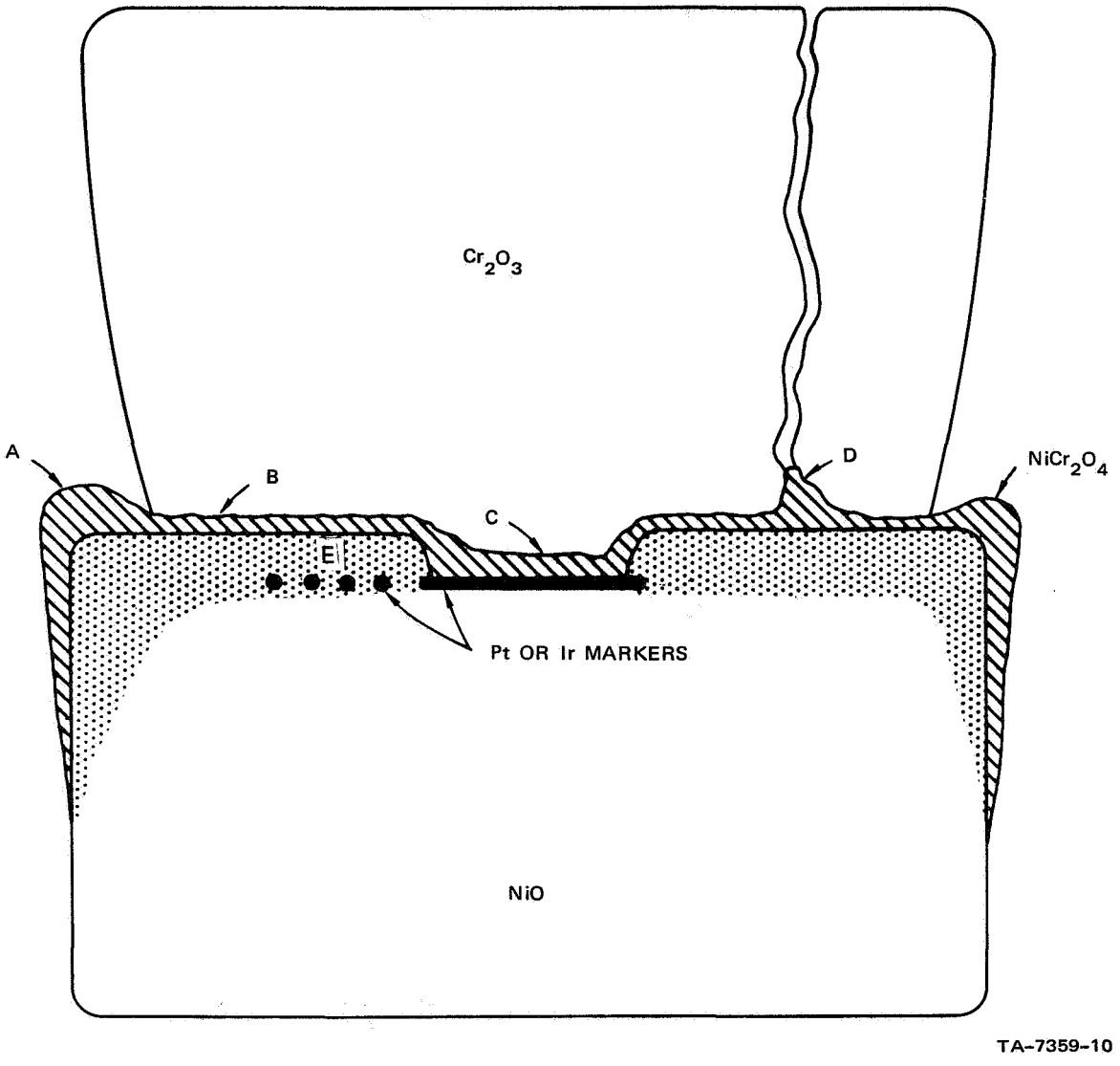

FIGURE 11 SCHEMATIC REPRESENTATION OF INTERNAL FEATURES OBSERVED IN NICKEL CHROMITE FORMATION FROM PURE OXIDES: (A) Spinel formed at corners of pellet exposed to air; (B) Spinel formed in dense, crack-free regions of pellets; (C) Spinel formed at "thick" marker; (D) Spinel formed internally but exposed to air by a crack; (E) Spinel precipitate in nickel oxide.

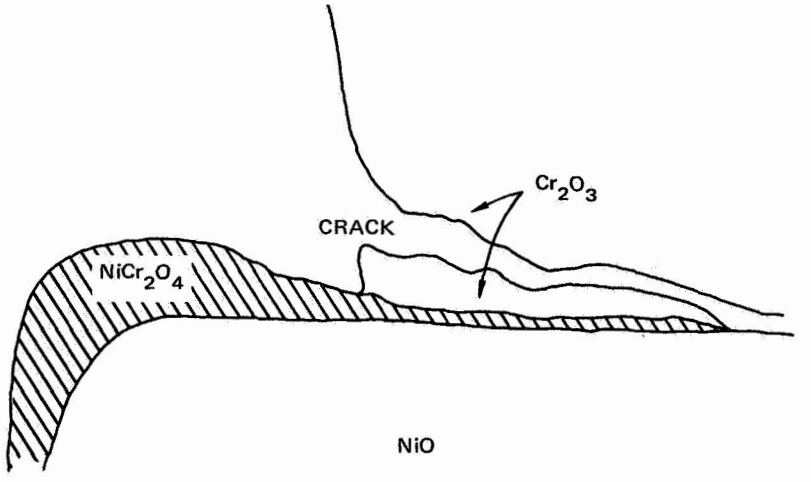

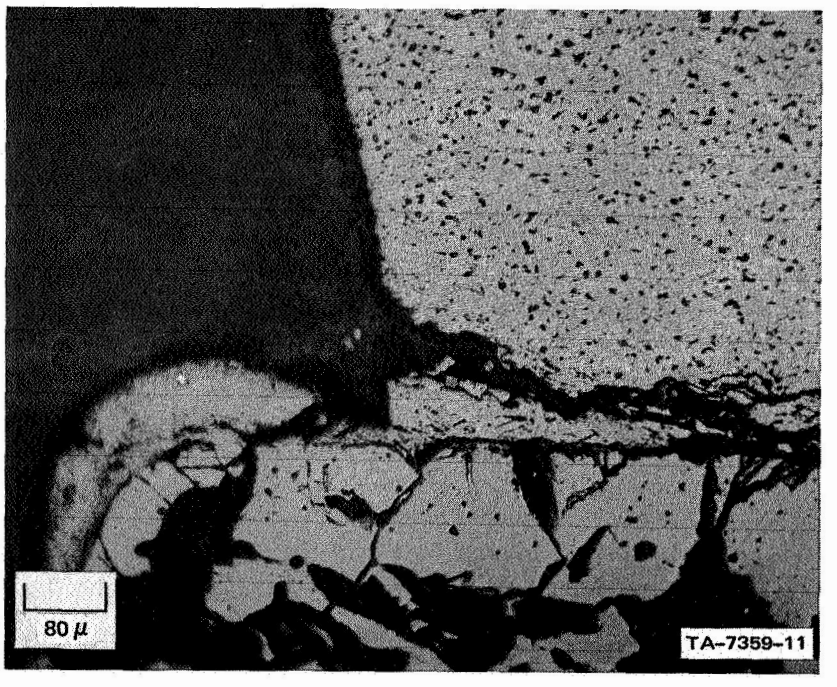

FIGURE 12 SURFACE AND INTERNAL NICKEL CHROMITE SPINEL FORMATION

mechanism of spinel formation will be given in a later section. Thick spinel layers also formed at thick (approximately 6 μ) platinum markers (location C). An example of thick spinel formation at such a marker and thin spinel formation from a region of the specimen that has no marker is shown in Fig. 13. The difference in the thickness of the spinel at these two locations is evident. The last predominant internal features (location E, Fig. 11) were found at the thin (1-2 μ) or discontinuous platinum or iridium powder markers. These thin markers were always buried within the nickel oxide. The depth to which the markers were buried increased with the time and temperature of exposure. The time dependence was parabolic, and the temperature dependence was Arrhenius in form. No differences were observed in the depths of the platinum and iridium markers after identical reactions. Examples of buried markers are shown in Fig. 14 for two separate specimens, one reacted for 64 hours at 1300°C, and the other for 88 hours at 1475°C. Also visible in the nickel oxide, both in specimens that contained markers (Fig. 14) and in specimens that did not contain markers (Fig. 13b), were very fine Widmanstatten precipitates. These precipitates extended well into the nickel oxide, and could be resolved on both sides of the markers. Examination of the marker regions in greater detail (Fig. 15) revealed that the precipitate size and orientation changed at the line of markers, and that a continuous grain boundary was formed at the marker line. This precipitation has not been reported previously. In addition to these features it was observed that noplanar diffusion interfaces formed between the spinel layer and the chromium oxide (Fig. 14a). However, the interface between the spinel and the nickel oxide was always planar (when complications arising from the presence of thick markers did not interfere). This nonplanar behavior of the diffusion interface at the chromium oxide/spinel interface was another feature that had not been reported previously.

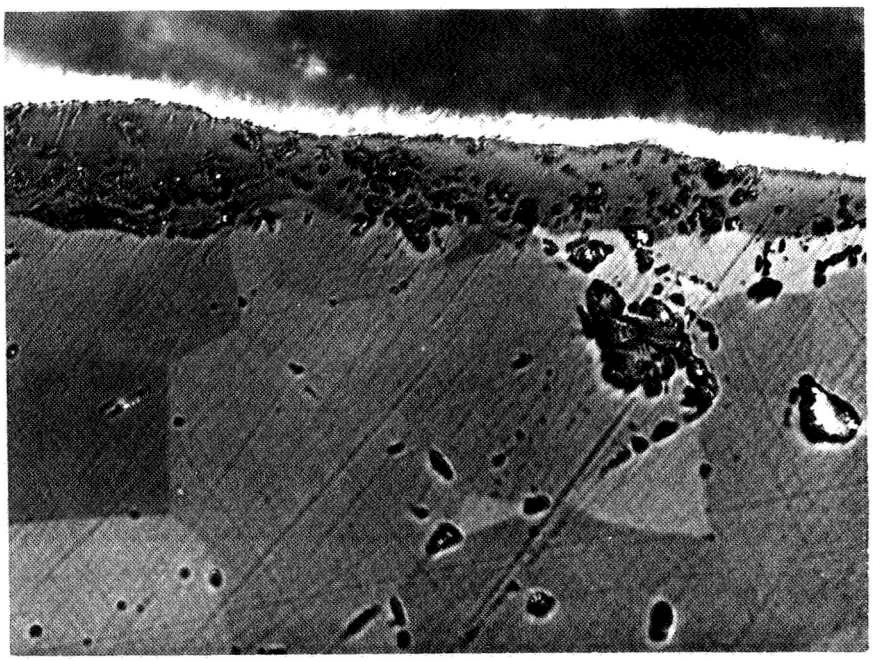

(a)

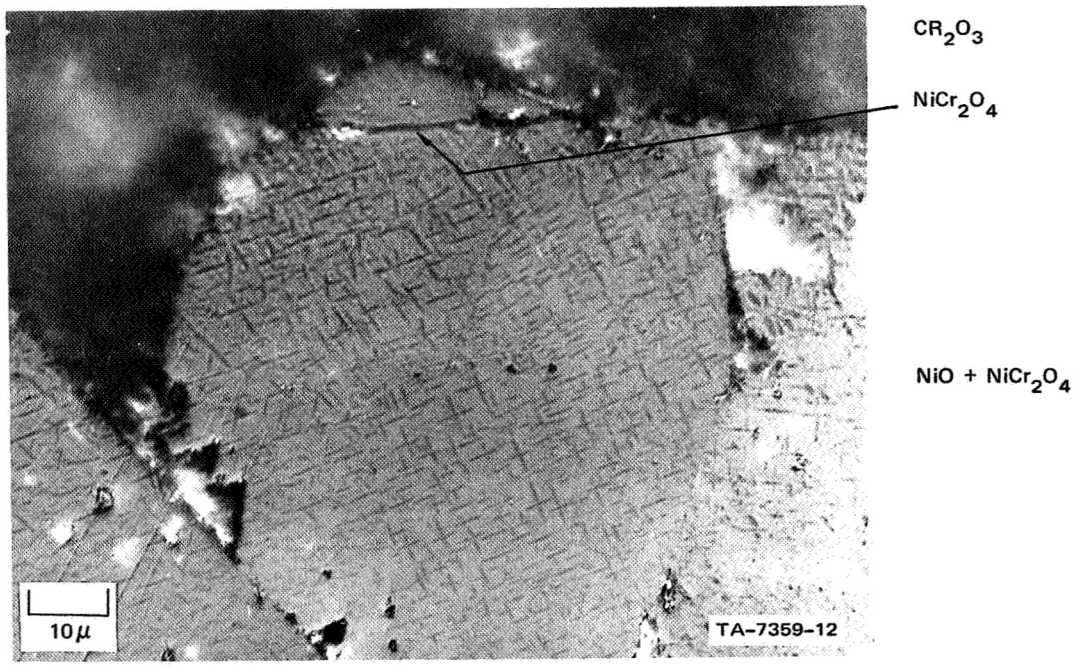

(b)

FIGURE 13 COMPARISON OF NICKEL CHROMITE LAYERS FORMED (a) AT THICK MARKERS AND (b) AT MARKER-FREE LOCATIONS. Note spinel precipitates in Ni-O.

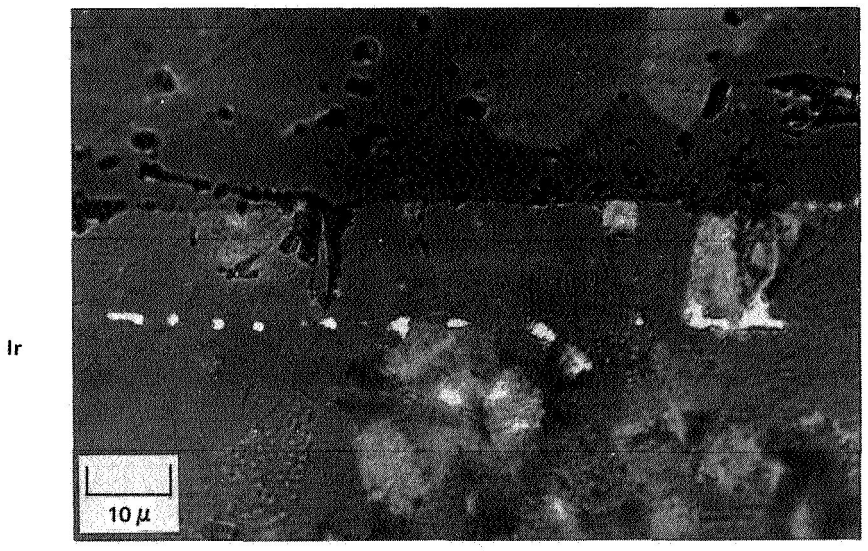

(a)

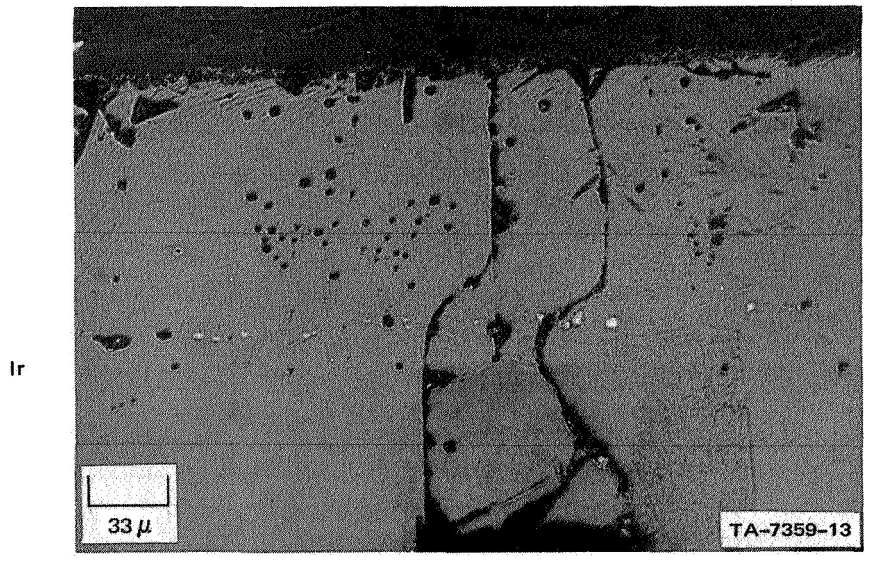

(b)

FIGURE 14 MARKER LOCATIONS IN NICKEL OXIDE REACTED (a) AT 1300°C AND (b) AT 1475°C

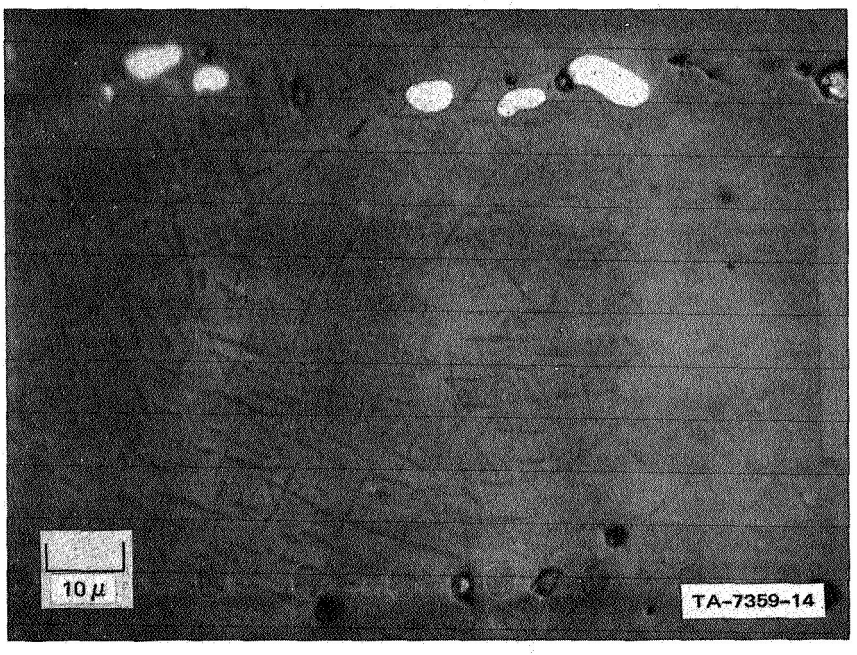

FIGURE 15 DETAILS OF PRECIPITATES AND BOUNDARY AT IRIDIUM MARKERS

All the above-mentioned features were observed in most of the specimens, and it was necessary to use techniques other than metallography to investigate the following questions before examining the kinetics or mechanism of nickel chromite spinel formation:

1. What were the precipitates that formed in the nickel oxide?

2. Why was the spinel layer that formed at the surface or at internal cracks orders of magnitude thicker than the spinel layer formed internally at dense, crack-free sites?

3. Why were thick spinel layers formed at thick markers?

4. Why were thin or discrete marker particles buried within the nickel oxide?

5. Why was the interface between the spinel and the chromium oxide nonplanar?

3. Phase Analysis and Precipitate Identification

The precipitates were identified by combining X-ray diffraction and metallographic techniques. A specimen that had been reacted and slowly cooled to room temperature (to accentuate the precipitation) was carefully ground parallel to the reaction interface. The ground face was examined by X-ray diffraction using Cr $K\alpha$ radiation. The NiO (111), Cr_2O_3 (104), and $NiCr_2O_4$ (220) reflections were measured after grinding. Approximately 10 to 20 μ of oxide were removed by each grinding step. The results of these measurements (Fig. 16) showed that the precipitates were nickel chromite spinel. The spinel precipitates could readily be detected at a distance of 80 μ from the dense spinel layer. Only nickel oxide and nickel chromite formation was detected at this distance, and no chromium oxide was detected until another 60 μ of oxide were removed.

This identification was somewhat ambiguous, in view of the possibility of grinding the specimen at an angle to the reaction

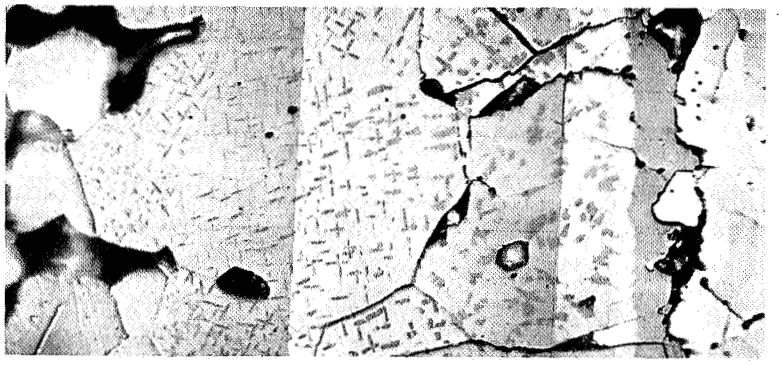

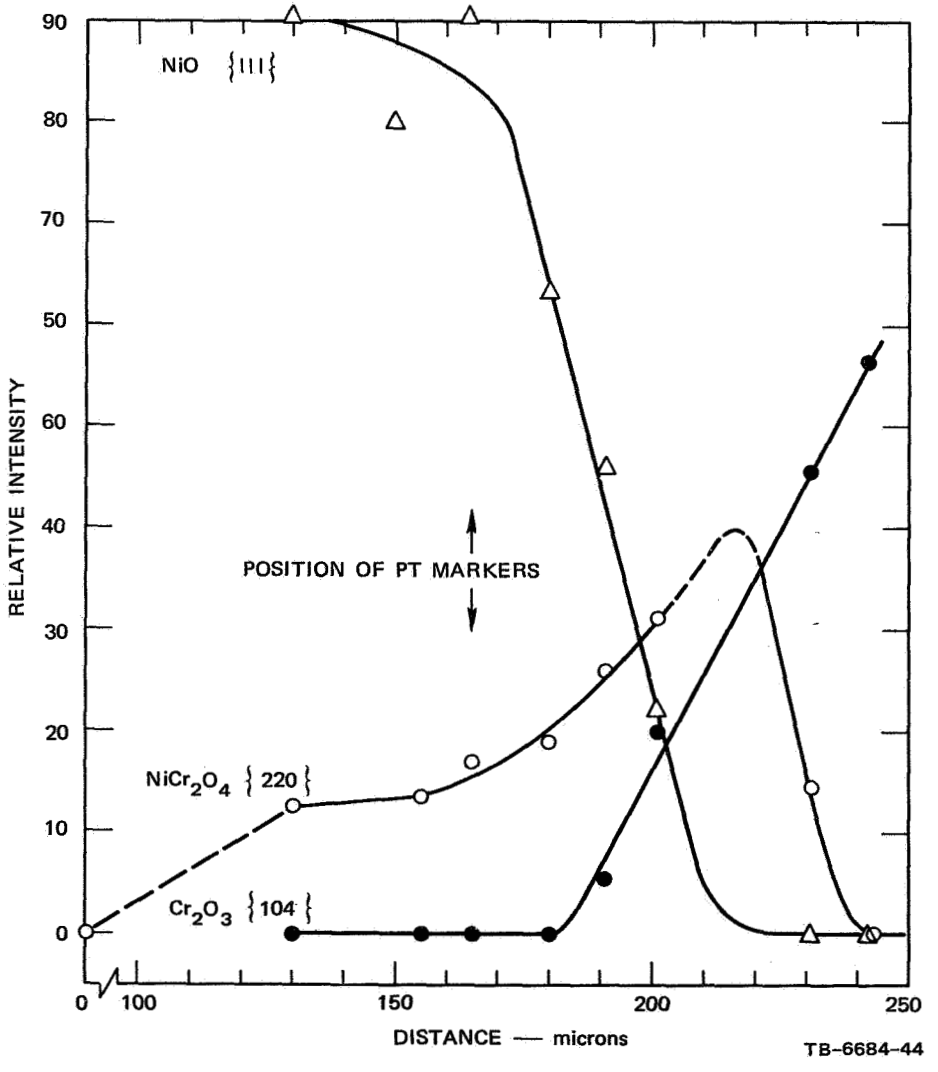

FIGURE 16 STRUCTURE AND PHASE ANALYSIS OF REACTION ZONE FORMED DURING SOLID STATE SPINEL FORMATION

interface and the possibility of detecting spinel radiation from beneath the surface of the specimen. This experiment, however, was later confirmed by the electron microprobe studies. All attempts to determine the reason for the difference in thickness between the spinel layers formed with access to air and the layers formed in crack-free regions of the specimen always led to the conclusion that two different mechanisms were responsible. The details of the reasoning leading to this conclusion are presented in the Discussion section.

4. Marker Behavior

The identification of the nickel chromite precipitate particles in the nickel oxide provided a reason for the formation of thick spinel layers at defect-free, thick markers and thin spinel layers away from the markers. Had the thin spinel layer been formed at the thick marker and the thick spinel layers at marker-free regions, a simple explanation could be proposed on the basis of inhibited diffusion of Ni^{2+} and Cr^{3+} through the marker. However, an alternate explanation had to be proposed and tested to explain the experimental observations. It was evident that the nickel chromite that formed in the nickel oxide was the result of dissolution of the spinel at the nickel oxide/spinel reaction interface. Consequently, if the rate of dissolution of the spinel layer by nickel oxide was the same order of magnitude as the rate of formation of the spinel layer at the interface, one would expect the resultant layer to be thin when no dissolution barriers were present, and thick when barriers were present.

To confirm this model, one would have to show that the amount of nickel chromite in the nickel oxide was less (indicating less dissolution of the spinel) at the the thick marker than the amount of nickel chromite at the marker-free region of the specimen. This confirmation was provided in part by the morphology of the reaction

interface at an imperfect platinum marker, and by the chromium and nickel concentration profiles at defected and defect-free regions of the marker. The structure and composition of the reaction interface at a defected thick platinum marker are shown in Fig. 17. The electron back-scatter image and the Ni $K\alpha$ X-ray image show the spinel layer to be very irregular at the spinel-chromium oxide interface. More important for the purposes of the present topic, both images show that two small defects in the marker have resulted in the formation of semi-circular intrusions of nickel oxide into the chromium oxide. X-ray image photographs using Pt $K\alpha$ and Cr $K\alpha$ radiation show that there has been little, if any, dissolution of the marker, and that the chromium oxide content in the instrusions has been greatly reduced. The structure of the defects alone shows that the spinel layer is being dissolved by the nickel oxide; however, the composition profiles add further evidence that the chromium content in the intrusion is greater than the chromium content at the defect-free region of the marker. The structure of the defect region of the platinum marker is shown in greater detail in Fig. 18, along with a chromium $K\alpha$ X-ray image and a model of the mechanism by which the semicircular intrusion formed. It is not immediately apparent from the X-ray image, but close inspection will show that there is a higher concentration of chromium in the nickel oxide at the intrusion than at the planar regions of the reaction interface. This higher chromium concentration is explained on the basis of a greater flux of chromium from the spinel into the nickel oxide at the intrustion than at the defect-free region of the sample. Consequently, since the rate of chromium diffusion in the nickel oxide at both locations will be essentially the same, chromium oxide will accumulate in the intrusion. Scanning across the specimen along paths A and B of Fig. 18 revealed the composition profiles shown in Fig. 19. It is evident from these profiles that the chromium concentration in the nickel oxide in the intrusion is significantly higher than the concentration of chromium in the

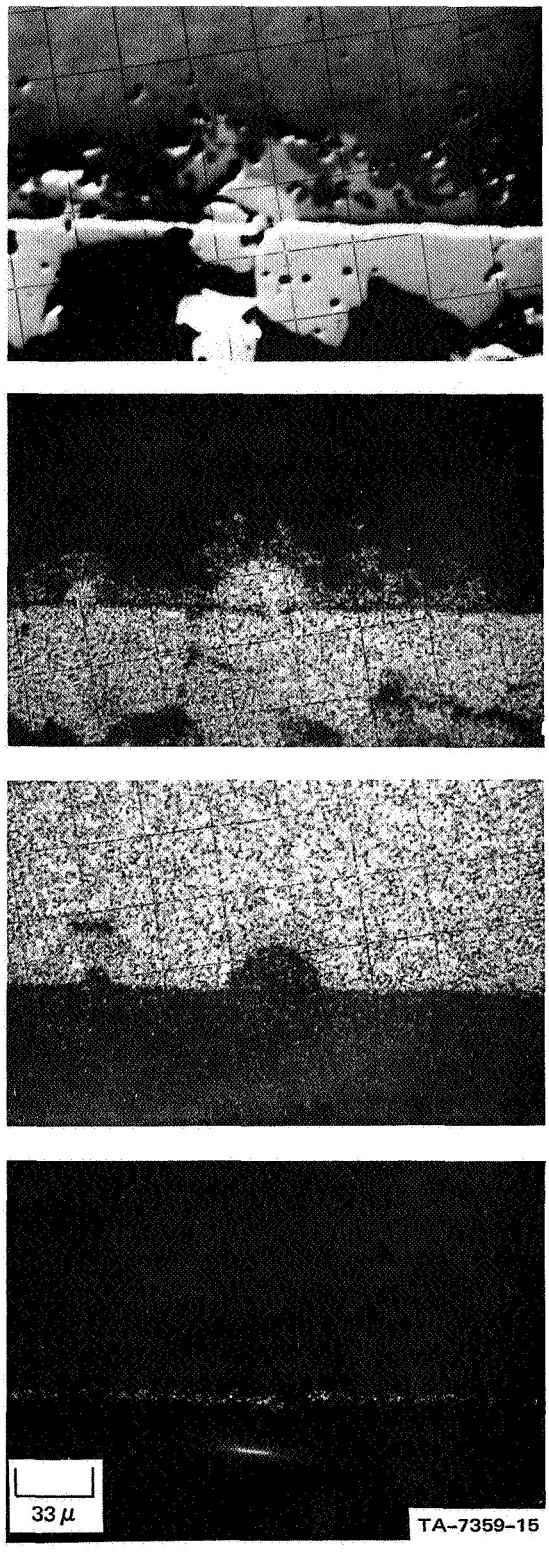

FIGURE 17 MORPHOLOGY AND COMPOSITION OF NICKEL OXIDE/CHROMIUM OXIDE REACTION INTERFACE AT DEFECTS IN THICK PLATINUM MARKERS

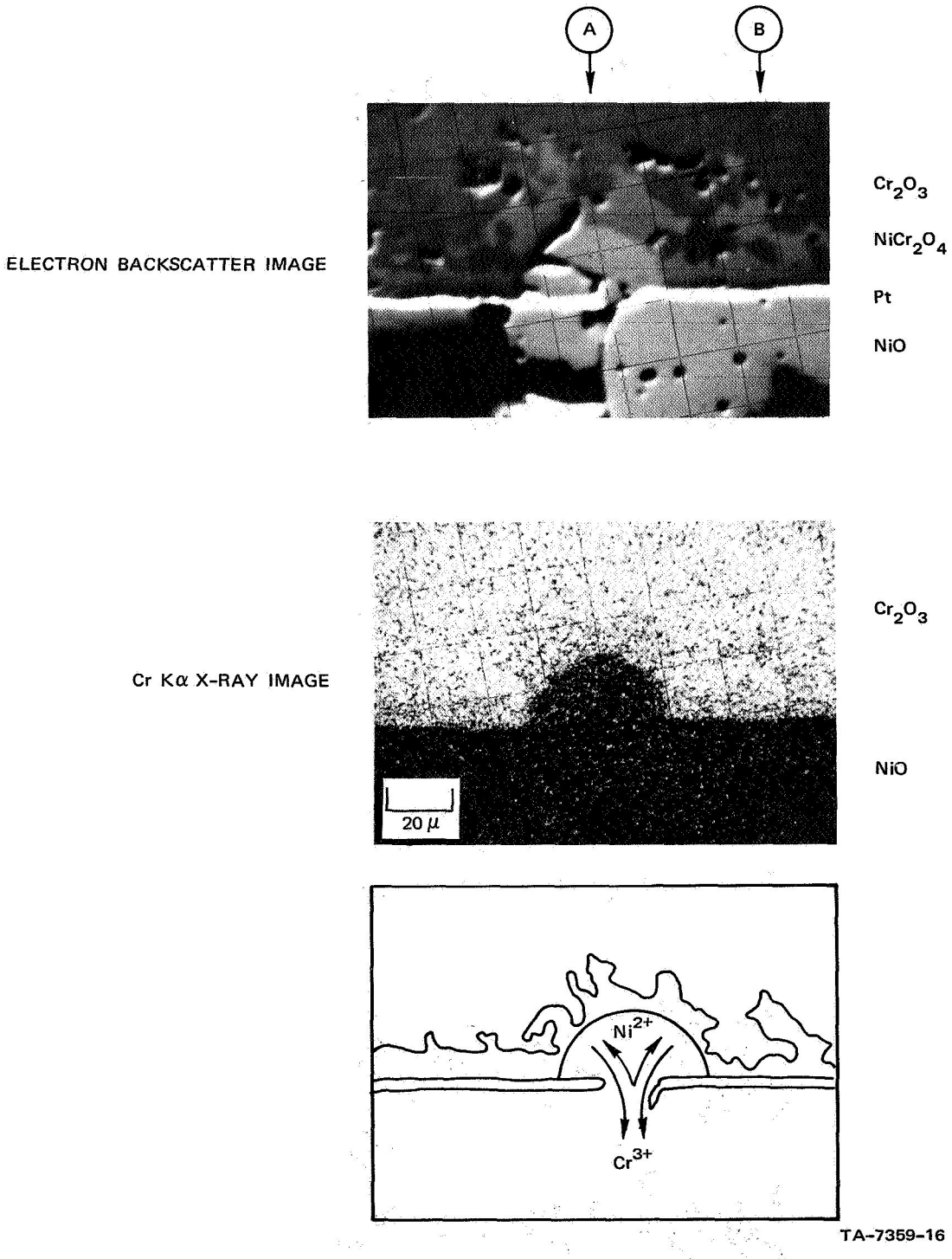

FIGURE 18 DETAILS OF STRUCTURE AT DEFECT IN PLATINUM MARKER. Chromium and nickel composition profile scans shown in Figure 19 were made at locations A and B.

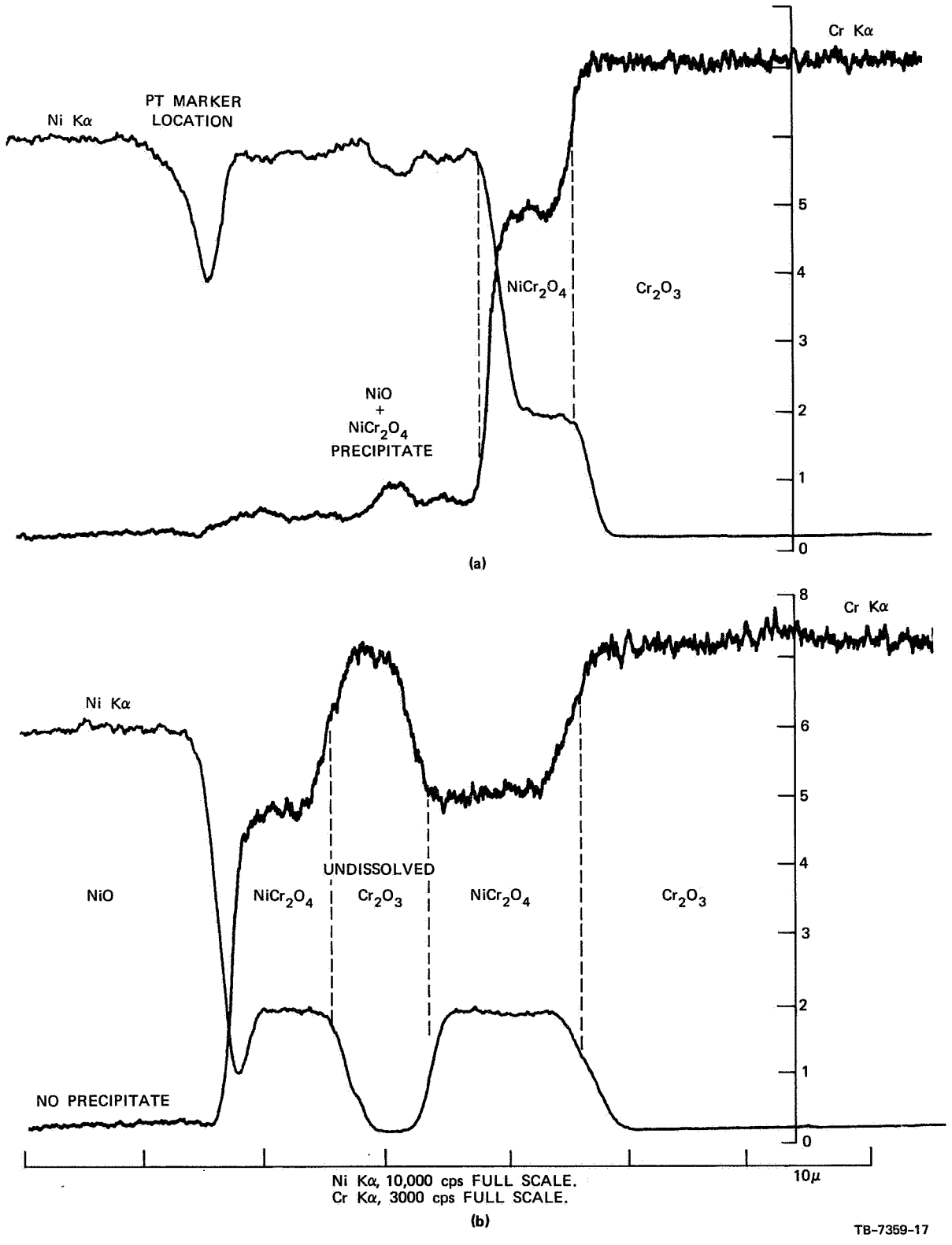

FIGURE 19 INFLUENCE OF THICK PLATINUM MARKER ON THE CONCENTRATION OF DISSOLVED CHROMIUM IN NICKEL OXIDE. (a) at marker defect (b) at continuous marker.

nickel oxide at the planar reaction interface. Consequently it can be concluded that the thick platinum markers cause the formation of thicker spinel layers because they are a barrier to chromium dissolution by the nickel oxide.

It can be argued that the example shown in Figs. 17 to 19 does not confirm the proposed barrier mechanism, since the geometry of the defect automatically reduces the cross-sectional area through which the dissolved chromium oxide must diffuse, and that the higher chromium concentration in the intrusion could be explained on the basis of geometry alone. Further, inspection of Figs. 17-19 shows that the thickness of the spinel at the intrusion is about the same as at the defect-free region. Both arguments are valid. However, the several examples of nickel chromite precipitation in the nickel oxide (which occurred at planar interfaces) already presented and electron microprobe data to be presented add to these results to confirm the dissolution barrier model.

The experiments shown in Figs. 17-19 also help explain the location of the thin and/or discontinuous markers in the nickel oxide (location E, Fig. 11). If the markers are discrete particles, they do not interfere with the spinel reaction and the spinel dissolution in the nickel oxide. Consequently, the simple interdiffusion reaction that would be expected if dissolution did not occur is replaced by a moving-boundary diffusion reaction, in which there is a flux of material into the spinel and a flux of the same order of magnitude into the nickel oxide. Consequently, the markers remain at the original interface, and the spinel/nickel oxide interface and the spinel/chromium oxide interface move toward the chromium oxide half of the diffusion couple. When thick platinum markers are used, spinel dissolution will occur only at defects (e.g., Fig. 17); consequently, the thick marker will remain at the original interface, while the regions of the specimen in which spinel dissolution is not blocked

will advance toward the chromium oxide. An example of this effect with thick markers is shown schematically in Fig. 11 and explicitly in Fig. 20, where the final interface has advanced away from the initial interface defined by the thick platinum marker. Although it is not clearly shown in Fig. 20, the spinel layer at the marker is at least 1 order of magnitude thicker than the spinel layer away from the marker. In addition to the evidence presented, some specimens have also shown regions in which platinum agglomeration occurred (leaving the markers buried in the nickel oxide), and some regions in which the agglomeration did not occur (leaving the markers at the spinel/nickel oxide interface). In these specimens, both the agglomerated and nonagglomerated markers were aligned. This effect (Fig. 11) is further evidence that neither the discontinuous nor the continuous markers move during the spinel reaction.

5. Single Crystal Experiments

Experiments with single crystals were performed for two major reasons: first, to clarify the reason for nonplanar diffusion interfaces between the spinel and the chromium oxide, and, second, to compare with the various observations of spinel formation from dense polycrystalline specimens.

As was shown previously, the reaction of the dense polycrystalline chromium and nickel oxides resulted in the formation of planar reaction interfaces between the spinel and the nickel oxide, but highly nonplanar reaction interfaces between the spinel and the chromium oxide (see Figs. 14-18). Careful metallographic examination of many specimens revealed that the irregular nature of the spinel/chromium oxide interface was often associated with grain boundaries in the chromium oxide. However, in a few instances preferential spinel growth into the chromium oxide occurred where no grain boundaries were apparent. Consequently, the reaction of single crystals

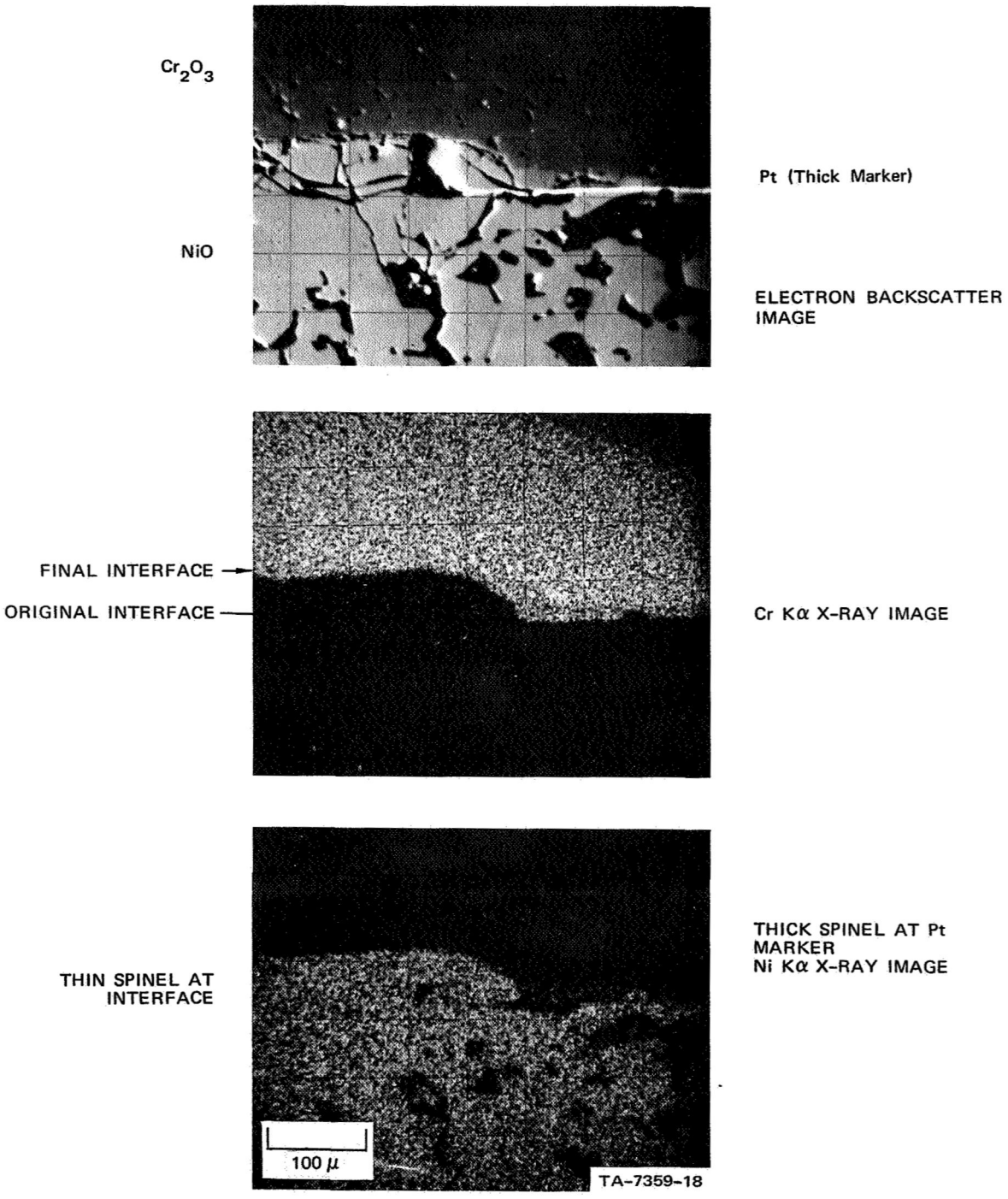

FIGURE 20 EXAMPLE OF MOVING INTERFACE DURING NICKEL CHROMITE FORMATION. The thick (~ 6 μ) platinum marker does not move during the reaction.

of chromium and nickel oxide would help determine whether the non-planar reaction interface was dependent only on the presence of grain boundaries.

In the first of the single crystal experiments, a single crystal of chromium oxide was reacted with a dense polycrystal of nickel oxide. The structure of the reaction interface at two locations (Fig. 21) was similar to that observed previously with polycrystalline diffusion couples. The central part of the diffusion couple contained a thin spinel layer between the single crystalline chromium oxide and the polycrystalline nickel oxide. Close inspection of the thin spinel layer in the center of the specimen also revealed that the reaction interfaces were not strictly planar, but this effect could be attributed to irregularities in the starting surfaces because the reaction layer itself was so thin. Precipitation of spinel in a Widmanstatten pattern was present in the nickel oxide. Toward the edge of the specimen and at a crack parallel to the reaction interface, the spinel layer was an order of magnitude thicker. In addition, the spinel/chromium oxide interface was very irregular (Fig. 21b). The irregularity of the spinel/chromium oxide interface at the thick spinel layer, however, was too prominent to be attributed to defects in the initial starting surfaces. This experiment therefore showed that the irregular reaction interface between the spinel layer and the chromium oxide pellet was not dependent on the presence of grain boundaries in the chromium oxide. However, it did appear that some access to air was necessary for the formation of the irregular interface.

The second single crystal experiment utilized single crystals of nickel oxide and chromium oxide. In this experiment, the thin spinel layer again formed (Fig. 22) between the starting oxides, and precipitation of nickel chromite spinel was clearly visible in the nickel oxide. In addition, the reaction interfaces between the spinel and both starting oxides were not strictly planar. In some local regions

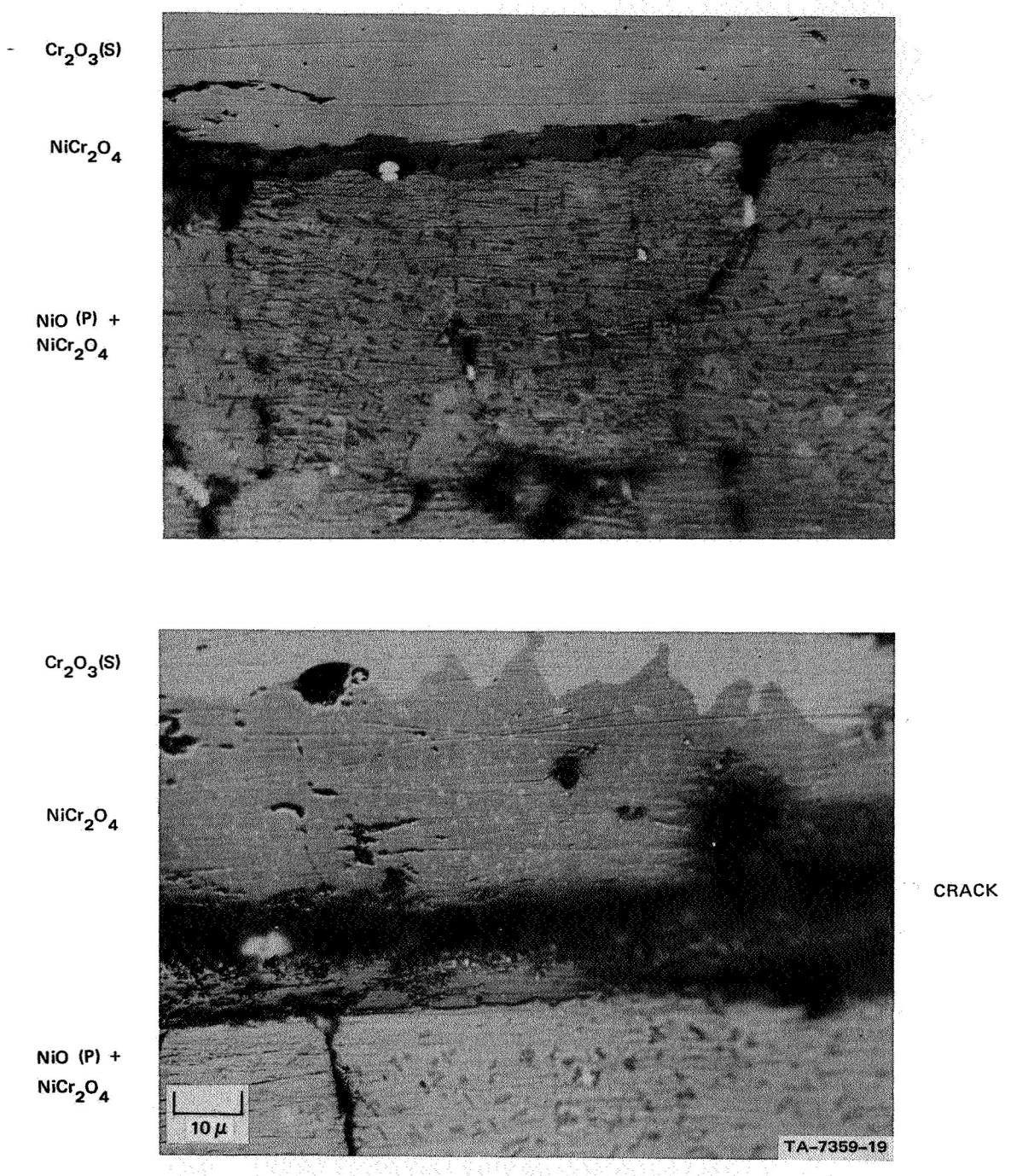

FIGURE 21 STRUCTURES OF SPINEL LAYERS FORMED BY THE REACTION OF SINGLE CRYSTAL CHROMIUM OXIDE AND POLYCRYSTALLINE NICKEL OXIDE: (a) At crack-free internal location, the layer is thin; (b) at cracked location the layer is thick.

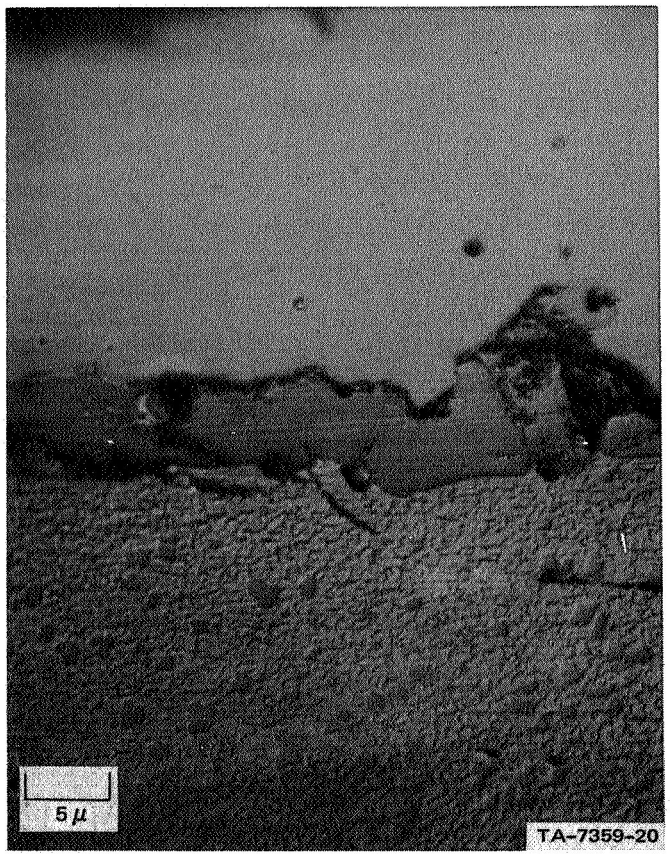

FIGURE 22 STRUCTURE OF NICKEL CHROMITE REACTION LAYER BETWEEN NICKEL OXIDE AND CHROMIUM OXIDE SINGLE CRYSTALS.

of the spinel layer, accelerated spinel penetration into the chromium oxide was observed (Fig. 22). These regions were often (but not always) associated with cracks in the spinel layer.

The single crystal experiments proved that the penetration of the chromium into the nickel oxide occurred by a solid state diffusion mechanism, and not by a vapor transport mechanism through pores (as was possible with the polycrystalline nickel oxide specimens). In addition, it was evident that this penetration occurred without the formation of porosity in either the nickel or chromium oxide single crystals. Further, the calculated parabolic reaction rate constants (described in a later section) were consistent with the rate constants derived from dense polycrystalline specimens. These observations therefore supported the conclusion that the results obtained with the polycrystalline specimens used in this study reflect the solid state spinel reaction mechanism. The lack of visible porosity in the single crystals allowed for the determination of a mass balance across the reaction interface. The composition gradients were required for this mass balance.

Electron microprobe measurements of the chromium $K\alpha$ radiation from the same area shown in Fig. 22 were made by point counting at 3 to 6 μ intervals using a beam diameter of $\sim$ 6 μ. The chromium $K\alpha$ X-ray intensity profile across the reaction interface (Fig. 23) showed in a quantitative manner the depth to which the chromium had penetrated into the nickel oxide. Measurable amounts of chromium could be detected at a distance of 625 μ from the spinel/nickel oxide interface. Figure 23 shows that the intensity-distance profile in the nickel oxide was very irregular, as would be expected from the presence of spinel precipitates in the single crystal nickel oxide. The spinel layer itself was too thin to be resolved by the point counting technique, however, the spinel intensity was calculated from comparison with the intensity data of Fig. 19, and the 6 μ spinel layer was

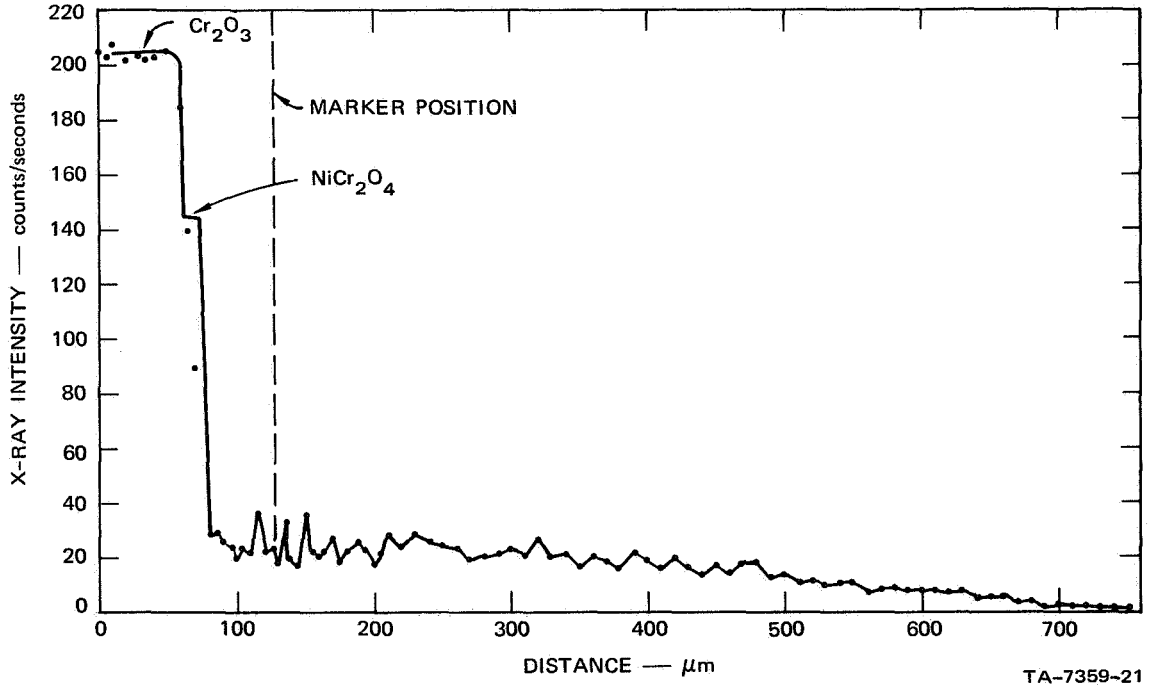

FIGURE 23 Cr Kα COMPOSITION PROFILE. Point count data show sufficient dissolved chromium in nickel oxide to account for marker position.

drawn accordingly. The position of the platinum marker in another area of the specimen is also shown, and will be used quantitatively in the discussion of the formation mechanism and in the formulation of the critical experiment described later.

As with the polycrystalline specimens, a thick spinel layer formed on the surface of the nickel oxide crystal that was exposed to air (location A in Fig. 11). This layer (Fig. 24) was dense and polycrystalline, and approximately one order of magnitude thicker than the internal spinel layer. An electron microprobe traverse of the specimen at this location was made to determine whether the depth of diffusion of the chromium into the nickel oxide was the same as that observed at the central part of the specimen. In addition, it was desirable to have a continuous scan in order to determine more detail of the penetration.

The scanning traverse shown in Fig. 25 was made with the MAC 400S microprobe. Measurements of the Cr Kα and Ni Kα intensities were made simultaneously using a 1 μ beam size. As can be seen from the intensity-distance profiles, there was one-to-one correspondence between the maxima and minima of the Cr and Ni Kα profiles, respectively. The intensity contours were more irregular than shown in the point counting traverse (because of the smaller beam size, and higher counting rate), but the depth of penetration was the same. Spinel precipitation was detectable as far as 575 μ from the spinel/nickel oxide interface. Evidence of dissolved chromium oxide in the nickel oxide is shown by the smooth, steadily decreasing Cr Kα profile from 575 to 750 μ. However, the corresponding increase in the Ni Kα intensity indicates that this may have resulted from instrumental drift. The solubility of chromium in the nickel oxide is very low at temperatures below 1000°C,[36] and it is probable that most of the chromium oxide precipitates as a spinel on cooling to room temperature. Rapid cooling experiments using chromium-oxide-doped nickel oxide powders would clarify this point.

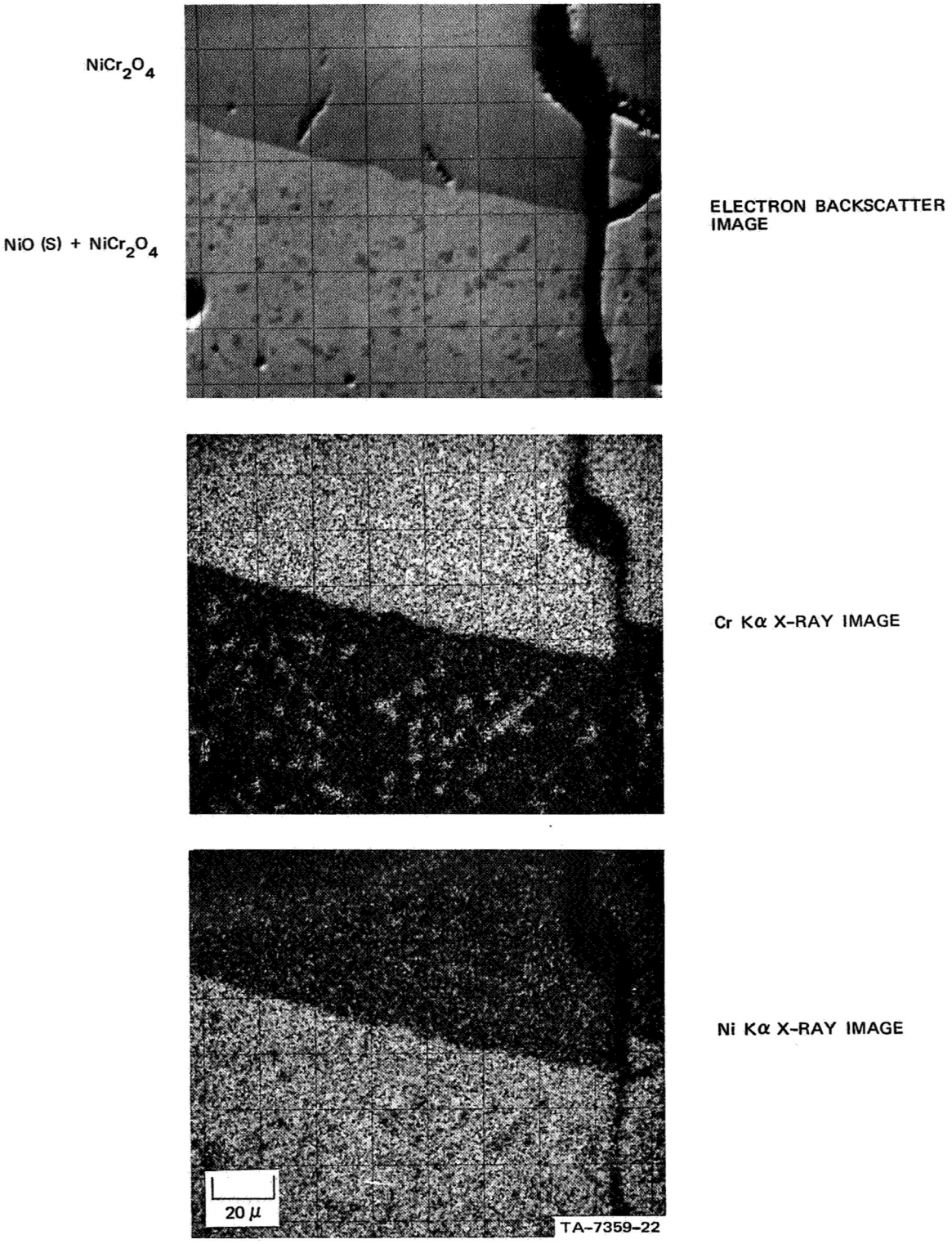

FIGURE 24 STRUCTURES AND COMPOSITIONS OF SPINEL/NICKEL OXIDE REACTION INTERFACE

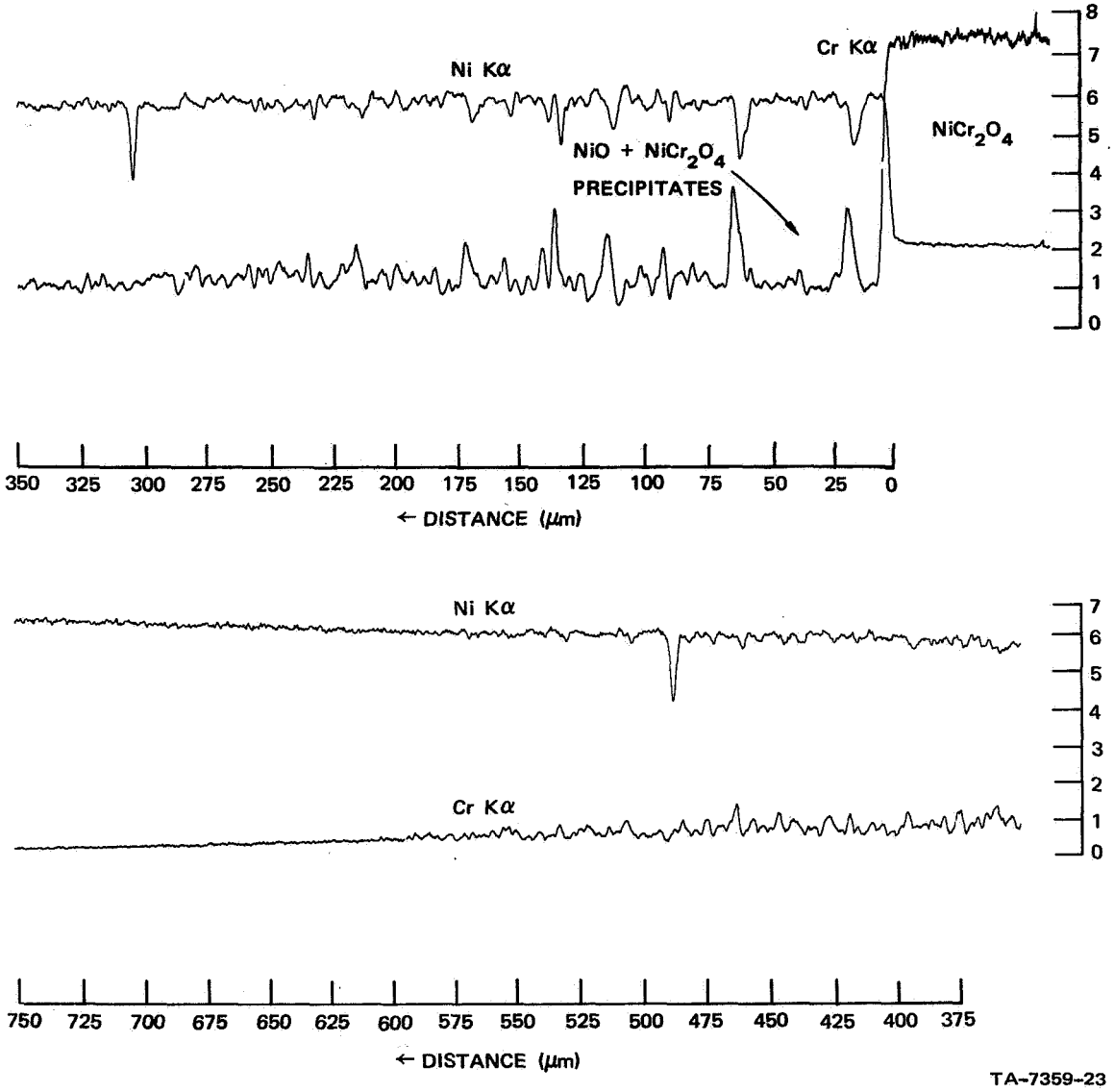

FIGURE 25 COMPOSITION PROFILES ACROSS NICKEL CHROMITE AND NICKEL OXIDE REACTION LAYERS. The chromium peaks in the nickel oxide prove the presence of nickel chromite precipitates. Ni Kα = 10,000 cps full scale, Cr Kα = 3,000 cps full scale.

In summary, the studies with single crystals only partially resolved the question of the nonplanar interface formation between the spinel and the chromium oxide. However, there appears to be enough evidence to indicate that the nonplanar interface occurs only when access to oxygen from the air is possible. This access will occur at cracks in the spinel layer, porosity in the starting oxides, or by oxygen diffusion along grain boundaries in the dense chromium oxide. The fact that the chromium penetration and spinel precipitation in the single crystalline nickel oxide were identical to those observed in the 95% dense polycrystalline nickel oxides proved that chromium penetration occurred by a solid-state diffusion mechanism and not by vapor transport along pores. The absence of porosity in either the nickel or chromium oxide single crystals after the spinel formation showed that a mass balance could be made and thus allow the determination of the mechanism of formation from the marker measurement. The analysis leading to this mechanism will be given in detail in a later section.

6. Vapor Transport Experiment

As was stated in the section III-C, spinel formation experiments were performed with the pellets loaded to a stress level of approximately 1 kg/cm^2. The objective of this load was to insure ideal contact between the starting oxides and thus minimize possible complications arising from vapor phase transport. Vapor phase transport of one or more of the reacting species has been widely reported in the literature[21,22,24-26,28] and has been used as a general explanation for the commonly observed phenomenon of easy separation of reactants after the spinel reaction. Schmalzried[22] has stated that this phenomenon results from the vapor transport of the more volatile species to the other reactant when non-ideal contact conditions exist between the two pellets. According to this mechanism, the more volatile species travels, via the gas phase, to the less volatile pellet and

reacts to form the spinel. Since there is never any solid contact, the pellets separate easily, and the spinel layer is bonded to the less volatile material. For example, in the formation of zinc aluminate, one would expect the spinel to stick to the aluminum oxide, while in the formation of magnesium chromite, one would expect the spinel to stick to the magnesium oxide. Extrapolating this generality to the nickel chromite system, one would expect the spinel to stick to the nickel oxide after an experiment in which non-ideal contact exists, because the vaporization rate of chromium oxide is greater than that of nickel oxide.[21] In the various experiments performed in the present study, the specimens were always firmly bonded after the reaction; small cracks were often present in the chromium oxide (Fig. 12) and in the spinel (Figs. 9b, 21), but only rarely in the nickel oxide.

An experiment in which contact was non-ideal was performed for comparison with the experiments in which ideal contact was assumed. The specimen assembly consisted of a flat-polished nickel oxide pellet separated from a flat-polished chromium oxide pellet by three 2 μ thick foil markers. No load other than the nickel oxide pellet was placed on the diffusion couple, and the resultant compressive stress level was of the order of 2 gm/cm^2. The experiment was performed at 1450^{0}C in order to produce a high vapor pressure of the chromium oxide, and thus assure non-ideal contact. After the diffusion anneal was completed (approximately 7 x 10^5 sec) the specimen was cooled to room temperature. Approximately 30 min were required to cool the specimen from the reaction temperature to room temperature. The specimen was then separated simply by lifting the nickel oxide pellet off the chromium oxide pellet.

The reaction surfaces of the two pellets were similar in appearance, and both showed traces of the former marker locations (Fig. 26). The surface of the nickel oxide pellet had depressions at the marker

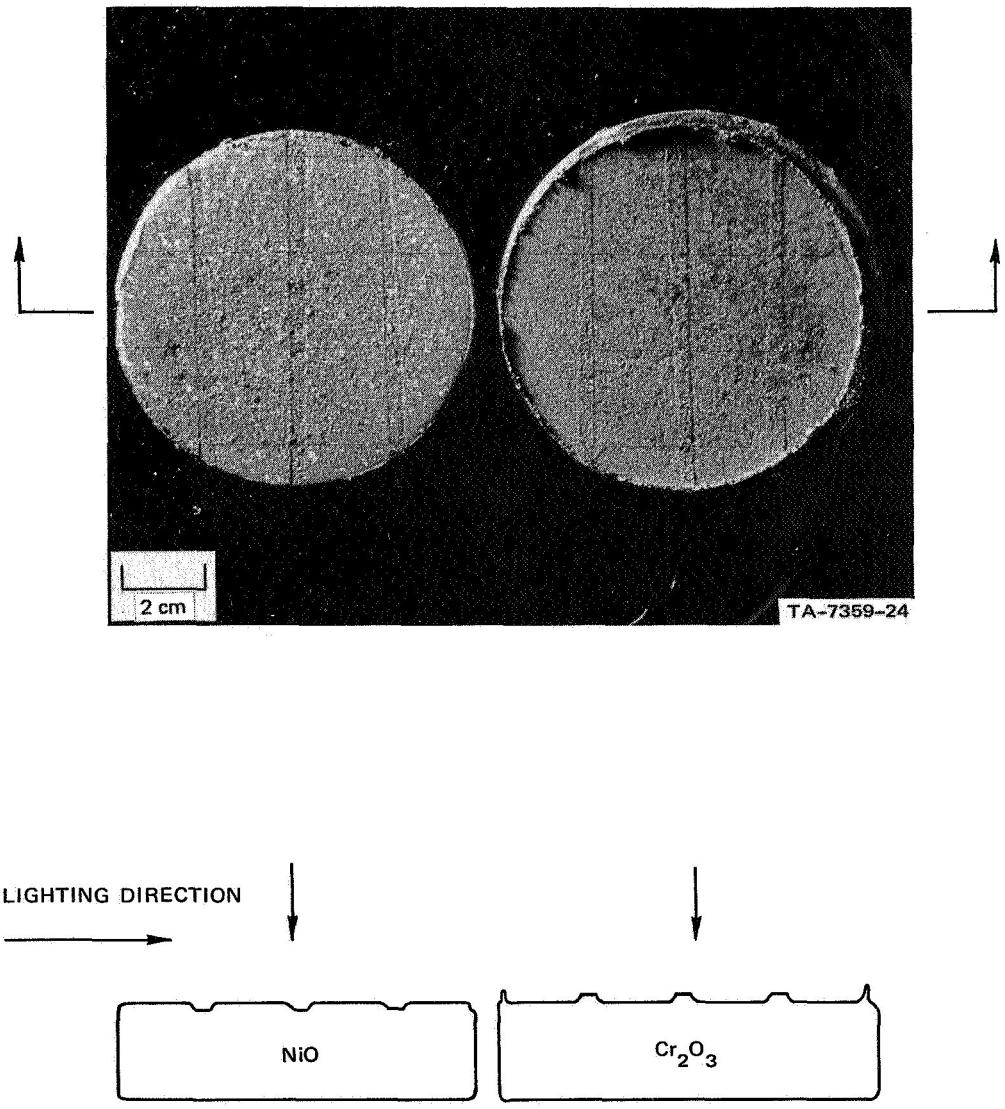

FIGURE 26 STRUCTURE OF SPECIMENS AFTER VAPOR-TRANSPORT EXPERIMENT

locations while the surface of the chromium oxide pellet was elevated at the marker location. From preliminary examination it appeared that the spinel had bonded to the chromium oxide. This was not expected in view of the generalization described above, and the easy separation of the pellets which indicated that non-ideal contact had been established. The markers themselves could not be seen, and were either buried in the spinel, in the nickel oxide, or at the spinel/chromium oxide interface.

Micrographic examination of the cross-sectioned pellets (Fig. 27) confirmed the bonding of the spinel to the chromium oxide, and revealed the platinum markers buried in the nickel oxide. Spinel precipitation was observed in some of the nickel oxide grains at the reaction interface, but the precipitation was very fine and difficult to resolve. The fine precipitate structure was probably caused by the very rapid cooling.

The spinel layer thickness on the chromium oxide was used to calculate a reaction rate constant, and this rate constant was consistent with the rate constants obtained at the same temperature using ideal contact. Therefore, the specimens were under ideal contact during the spinel reaction, even though they were very lightly loaded and they separated readily. If non-ideal contact had existed, the spinel should have formed on the nickel oxide (as it forms on the corners of nickel oxide specimens exposed to chromium oxide vapors and air). Since this structure did not occur, one can conclude that the easy separation of pellets does not necessarily provide any indication of the reaction mechanism. The easy separation could have been caused by interfacial cracking during cooling between the solidly bonded spinel and the nickel oxide layers. The absence of cracking of the chromium oxide indicated that the cooling strains were relieved by some other mechanism. Since vapor phase transport did not occur during this experiment, it appeared that the experimental observations should be

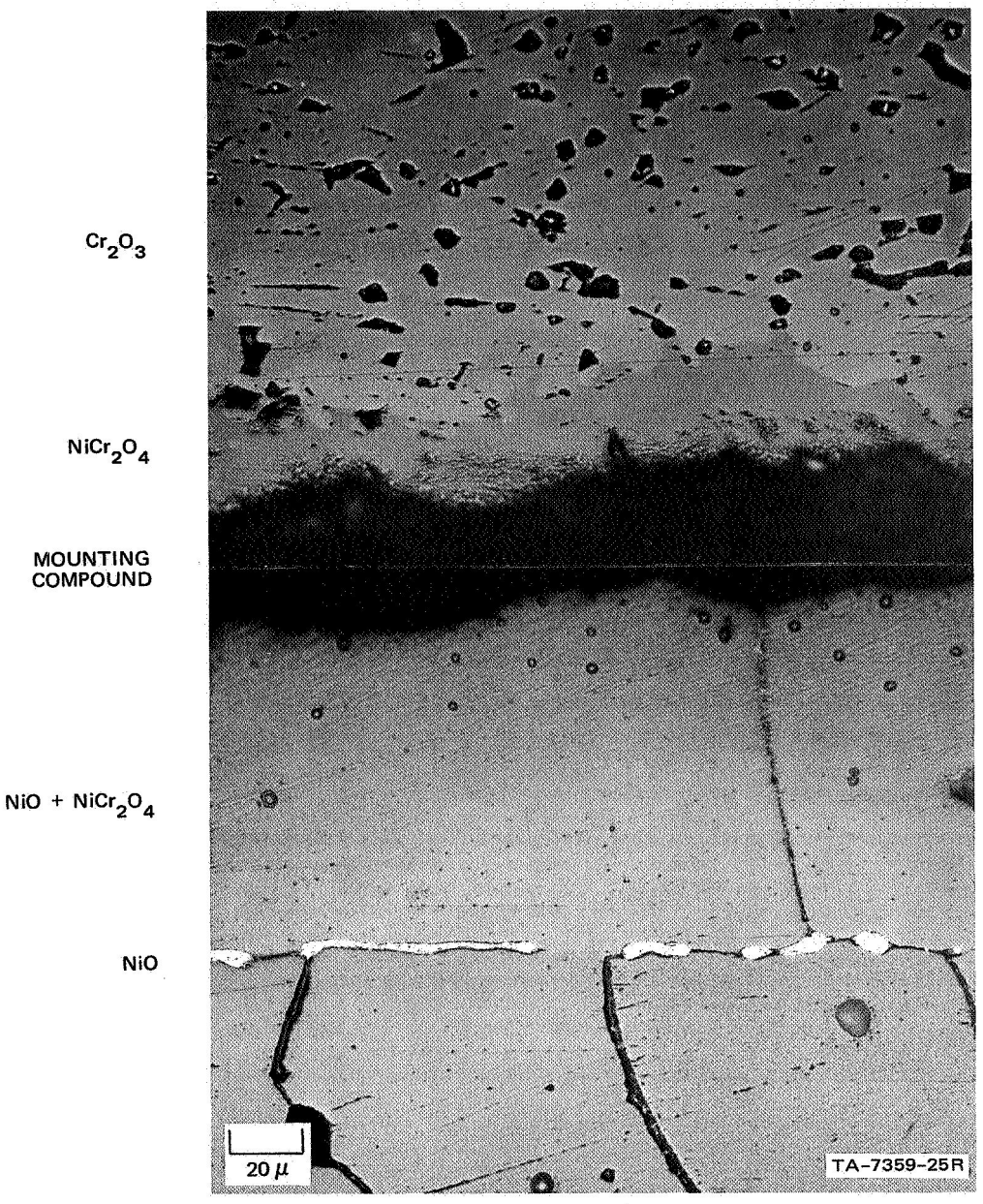

FIGURE 27 MICROSTRUCTURE OF VAPOR-TRANSPORT SPECIMENS. Spinel is bonded to chromium oxide, and platinum markers are buried in nickel oxide.

explainable in terms of a solid state reaction mechanism. Any explanation of the experimental observations must include a rational explanation for the depressions on the nickel oxide and the elevations on the chromium oxide at the former marker locations.

It was obvious that these topological features could not be explained on the basis of oxide displacement by the platinum marker, because the marker was very thin and, more importantly, because the marker was buried under a depression.

However, the observed effects could readily be explained in terms of effects observed and explained in the previous section on marker behavior.

A schematic drawing of the proposed sequence of events which formed the specimens is shown in Fig. 28. At the first stage of reaction, ideal contact occurred between the two pellets by a combination of deformation of the markers and the oxides. Reaction to form nickel chromite then proceeded with simultaneous chromium dissolution by the nickel oxide. The dissolution of the spinel at the marker, however, was inhibited by the presence of the markers. In the third stage, the spinel/nickel oxide interface continued to move away from the original interface, and intrusions of nickel oxide began to form as defects formed in the marker by surface tension forces. In stage four the marker had agglomerated enough that the spinel dissolution could no longer be inhibited, and the spinel/nickel oxide interface moved away from the marker. The discontinuity in the reaction interface at the prior marker location remained, however, because the starting time for the dissolution reaction was delayed by the presence of the marker. At stage five, the specimen was cooled and separted at the spinel/nickel oxide interface by the formation of interfacial cracks. This mechanism leaves the spinel bonded to the chromium oxide, elevations on the chromium oxide at the former marker location, and depressions

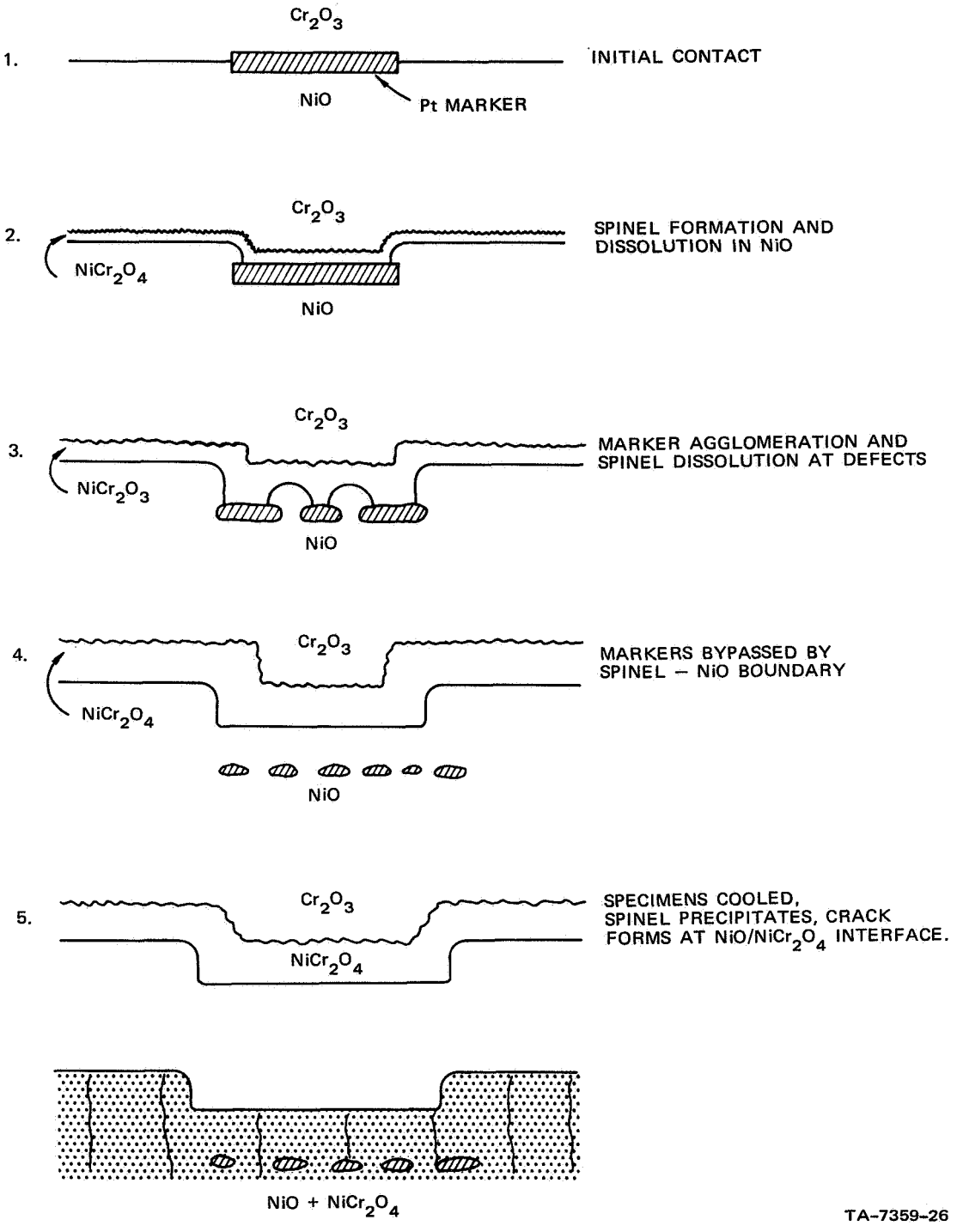

FIGURE 28 SCHEMATIC REPRESENTATION OF REACTION MECHANISM IN VAPOR-TRANSPORT EXPERIMENT

in the nickel oxide at the former marker location as observed experimentally. No other sequence has been developed by the author which can explain the observed microstructural and topological features so easily.

7. Presaturated NiO Experiment

In the previous experiments the platinum markers were always buried in the nickel oxide after extended reaction at all temperatures from 1200 to 1550°C. The markers were buried in the nickel oxide whether or not the reactions were done under conditions of ideal contack or non-ideal contact. Because nickel chromite precipitation was generally observed in the nickel oxide, the burial of the marker could be attributed to dissolution of the spinel by the nickel oxide. Consequently if the nickel oxide were presaturated with chromium oxide, one would expect the position of the marker and the reaction layer to represent the true mechanism of nickel chromite formation.

Figures 19a and 23 show significant precipitation of spinel in the nickel oxide adjacent to the reaction layer. Simple straight line extrapolations and Cr $K\alpha$ intensity ratios were used to determine the chromium concentrations in the nickel oxide adjacent to the spinel. These values were equivalent to 12 wt % chromium oxide and 14 wt % chromium oxide for Fig. 19a and 23, respectively.

A presaturated pellet of nickel oxide containing 13 wt % chromium oxide was prepared by blending the high-purity nickel oxide with reagent grade chromium oxide, cold pressing, and firing at 1400°C for 100 hours. After reaction the specimen was approximately 80% of the expected density. This was the least dense of all the specimens used in this study. A polished section (Fig. 29) revealed, however, that the specimen contained some regions of high density, and that all the chromium oxide had dissolved and precipitated on cooling as nickel chromite. This structure was identical to those formed during the

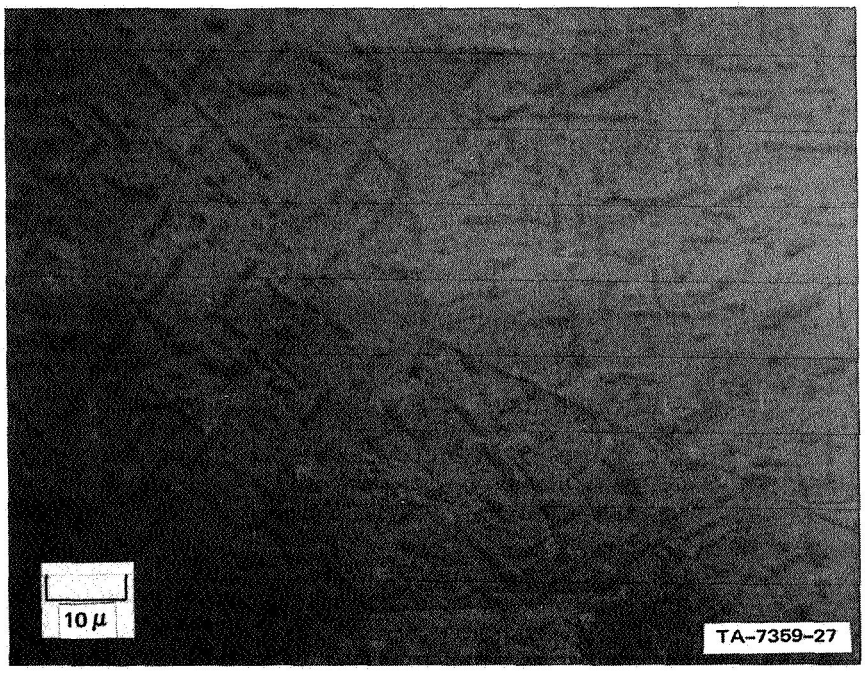

FIGURE 29 STRUCTURE OF NICKEL OXIDE, 13 wt % CHROMIUM OXIDE AFTER REACTION AT 1400°C. All chromium oxide dissolved and precipitated as nickel chromite on cooling.

reaction of Nickel oxide and chromium oxide pellets (Figs. 4b, 13b, 14, 15, 16, 21, and 22). There was no evidence of any undissolved chromium oxide in the presaturated pellet. The pellet was then ground flat and reacted with a fully dense chromium oxide pellet at 1360°C for 137 hours and furnace cooled.

Preparation of the sample for micrographic examination was difficult because of the porosity, but there was good evidence that the platinum marker, which was originally at the nickel oxide/chromium oxide interface was buried in the spinel after the reaction (Fig. 30). The ratio of the spinel layer thickness on the nickel oxide side of the marker to the thickness on the chromium oxide side was approximately 1:1 rather than the 1:3 which would be expected for the Wagner mechanism. However, this ratio could easily have been affected by errors in the exact solubility required at the reaction temperature, and by preferred growth of spinel on the nickel oxide side of the marker during the slow furnace cooling. This experiment confirms the Wagner inverse cation diffusion mechanism for nickel chromite.

C. Nickel Chromite Formation from Doped Oxides

Various experiments were performed with diffusion couples in which the nickel oxide was doped with either 1 mole % manganese oxide or with 1.5 mole % silicon oxide. In general the spinel formation reaction with the manganese-doped nickel oxide was the same structurally and kinetically as the spinel formation reaction with the pure oxide. The same macro and microstructural features were observed, including the rapid surface spinel formation, the slow spinel formation at internal, crack-free locations, and the inhibited spinel dissolution at thick platinum markers. The only significant difference between the spinel formed from the pure and the manganese-doped nickel oxide was the manganese enrichment of the spinel phase when formed from the latter oxide. This enrichment at a thin spinel layer is shown in

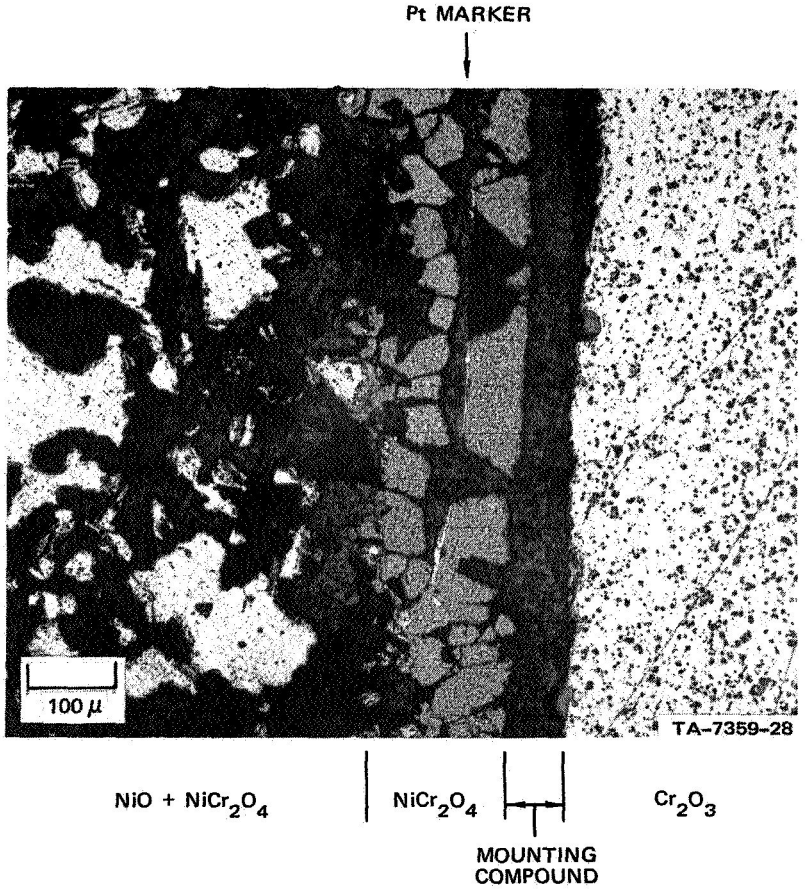

FIGURE 30 STRUCTURE OF SPINEL REACTION INTERFACE FORMED BETWEEN CHROMIUM-SATURATED NICKEL OXIDE AND CHROMIUM OXIDE. Platinum marker buried in spinel supports Wagner mechanism.

Fig. 31. In the Mn $K\alpha$ X-ray image photograph, the spinel layer is richer in manganese than either the manganese-doped nickel oxide or the undoped chromium oxide. No unusual chromium or nickel distributions are produced by this enrichment. A quantitative estimate of the degree of manganese enrichment in the spinel is given by the X-ray scans shown in Fig. 32. These scans show that the manganese concentration in the spinel is approximately 4 times greater than in the doped nickel oxide.

The spinel reaction in nickel oxide doped with 1.5 mole % silicon oxide was completely different from the reactions in pure or manganese-doped nickel oxide. With the silicon-doped specimens, the reaction product consisted of a two-phase chromium oxide-nickel chromite layer. The two-phase layer (Fig. 33) was dense, and appeared to contain only chromium oxide and spinel. No evidence of silicate formation was seen in the spinel layer, and some evidence of silicon rejection from the nickel oxide was shown by the absence of nickel silicate from the nickel oxide adjacent to the two-phase reaction product.

D. Kinetics of Nickel Chromite Spinel Formation

To confirm the previously reported observations that spinel formation was diffusion controlled,[9,21,28] the thickness of the spinel surface layer was determined as a function of $t^{\frac{1}{2}}$ for two reaction temperatures. These measurements (Fig. 34) showed that the spinel thickness was indeed a linear function of $t^{\frac{1}{2}}$, and therefore controlled by diffusion processes. As Fig. 34 shows, there was scatter in the data, resulting partly from the nonplanar reaction interface between the spinel and the chromium oxide and partly from the influence of oxygen on the rates of spinel formation. Wherever oxygen was available, the reaction rate was rapid, but wherever oxygen was unavailable (as in the dense, crack-free parts of the specimens), the reaction rate was slower. Once it had been determined that the reaction was

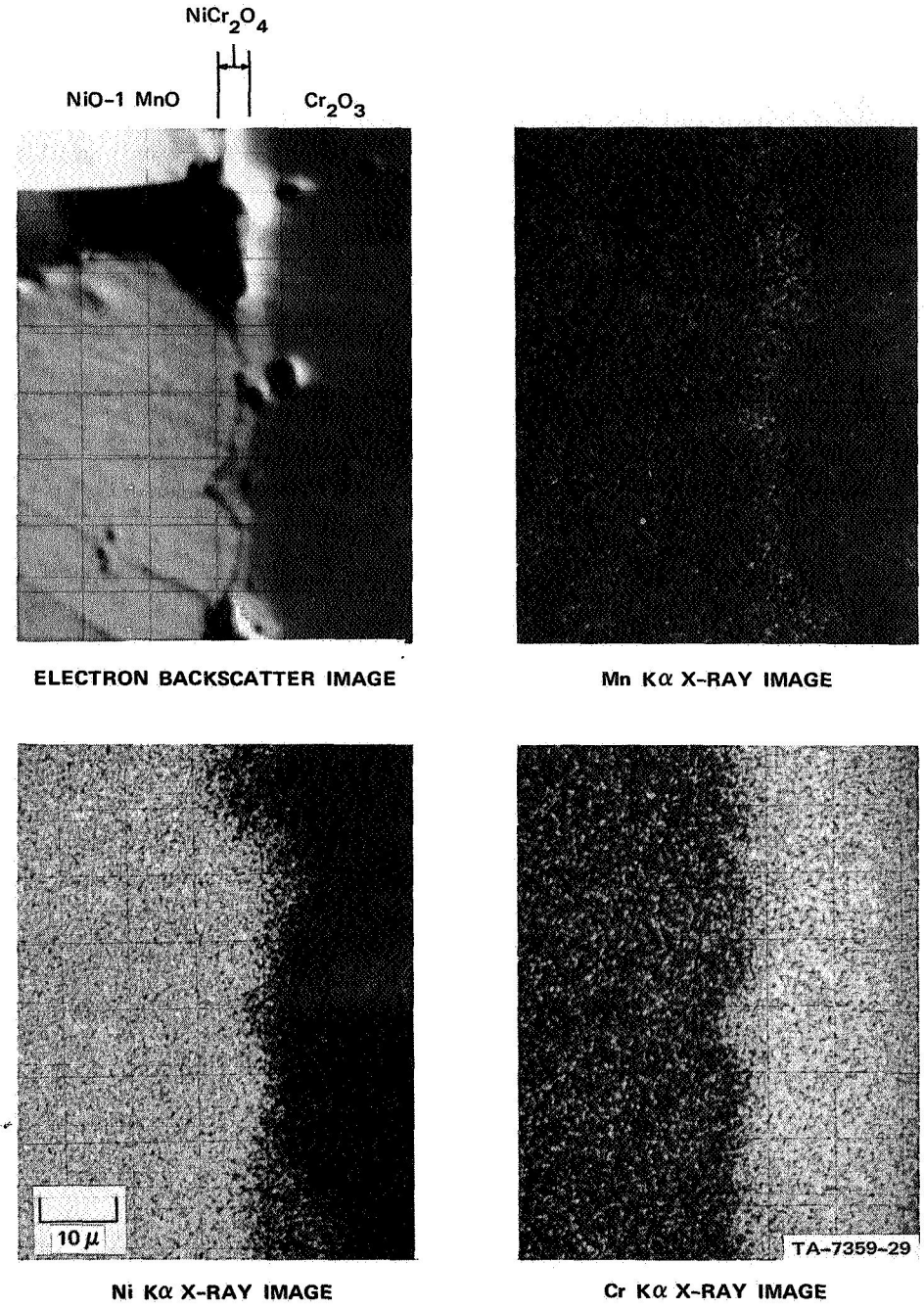

FIGURE 31 THIN SPINEL LAYER FORMATION. Manganese enrichment in the spinel is shown qualitatively by the X-ray image photographs.

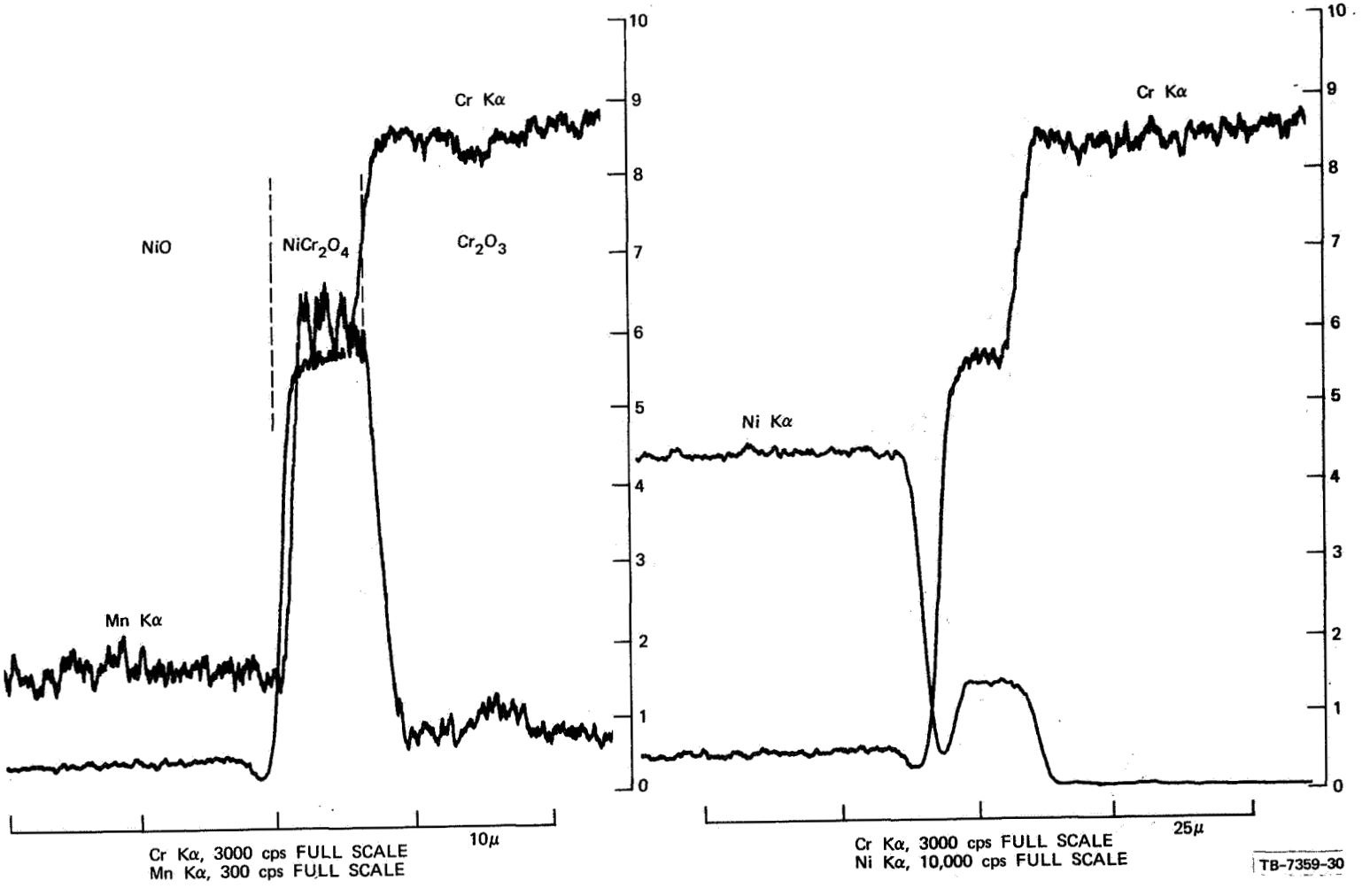

FIGURE 32 COMPOSITION PROFILES ACROSS A NICKEL CHROMITE REACTION INTERFACE. Manganese enrichment of the spinel layer from the manganese-doped nickel oxide is clearly evident.

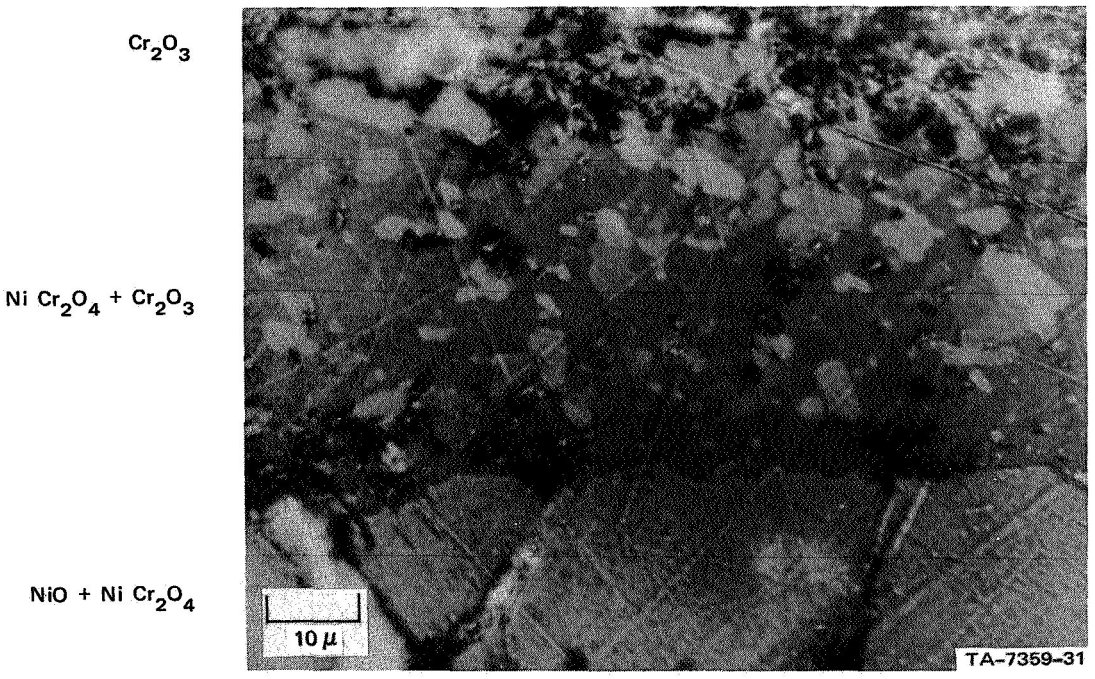

FIGURE 33 TWO-PHASE SPINEL-CHROMIUM OXIDE LAYER FORMED BY THE REACTION OF SILICON-DOPED NICKEL OXIDE WITH PURE CHROMIUM OXIDE

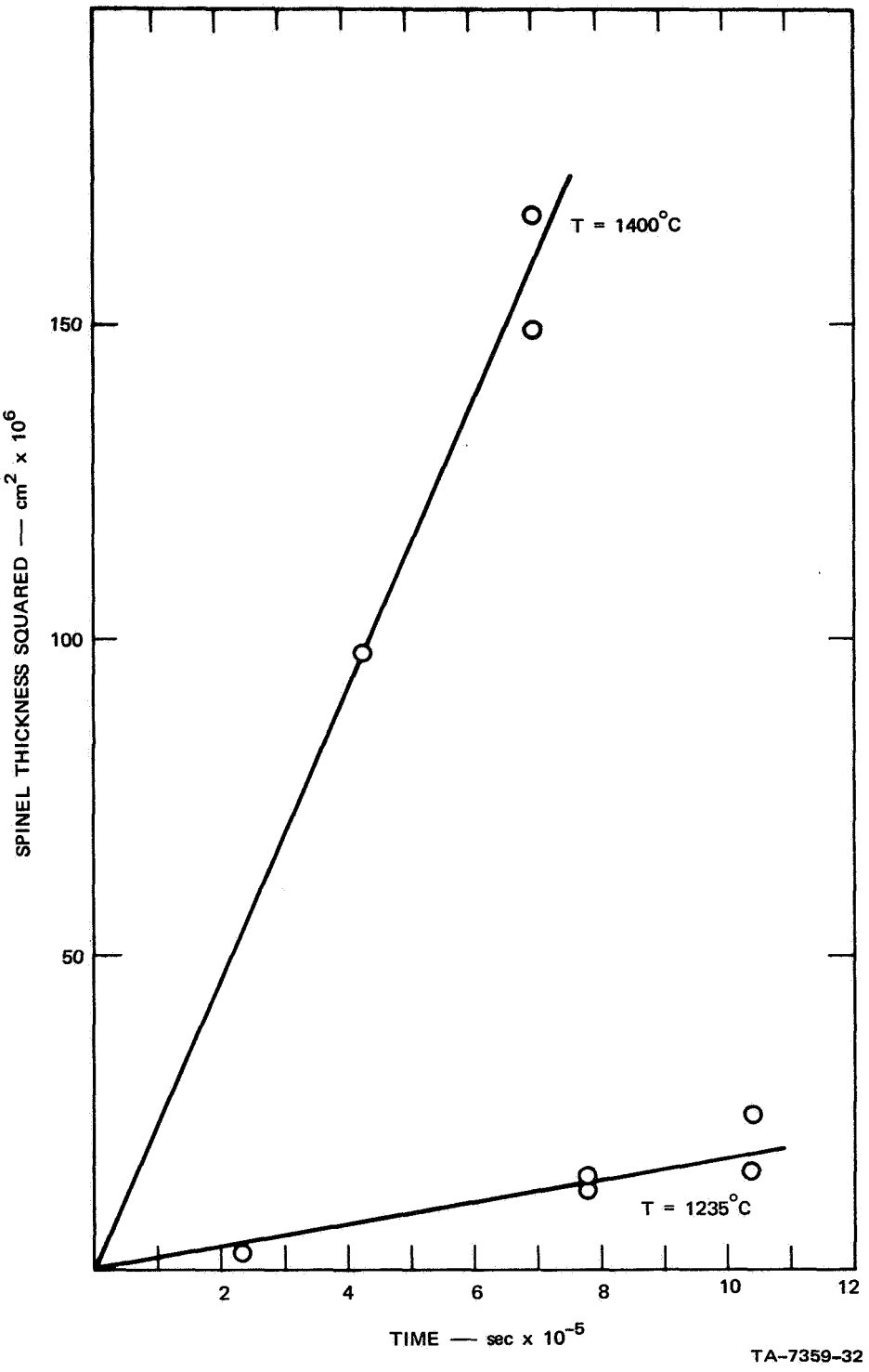

FIGURE 34 TIME DEPENDENCE OF NICKEL CHROMITE THICKNESS

diffusion controlled, a series of experiments were performed over a temperature range from 1200 to 1550°C in which high purity chromium oxide was reacted with high purity and commercial purity nickel oxide, and with nickel oxide doped with nominally 1 mole % silicon oxide and with 1 mole % manganese oxide. The reaction constant (k_p) for each experiment was calculated from the measured thickness (Δx) and the reaction time (t) using equation 11. In those experiments in which the pellets had been prebonded at one temperature and then reacted at a higher temperature, the reaction rate constant was calculated from the equation

$$K_p = (\Delta x_f^2 - \Delta x_i^2)/2t_f \qquad (40)$$

where Δx_f is the final spinel thickness, Δx_i the initial spinel thickness, and t_f the final reaction time. As was mentioned earlier the final layer was generally 2 to 3 times thicker than the initial reaction layer. Consequently the final reaction rate constant was calculated on the basis of the difference between a large number (Δx_f^2) and a number (Δx_i^2) 4 to 10 times smaller. These corrections resulting from the limited number of experiments in which pre-bonded specimens were used were consequently very small. In view of the considerable scatter in the rate constants, it will be seen that these corrections were generally negligible.

Since the spinel at the surface of the specimen was much thicker than the spinel inside the dense, crack-free regions of the specimen, the reaction rates at these two locations were considerably different. The spinel thicknesses at the specimen surface, within the dense interior of the specimen, and at cracks in the dense interior of the specimen were measured and used to calculate rate constants by equation 11 or 40. In addition, the distance from the spinel/nickel oxide interface to the platinum or iridium markers buried in the nickel oxide was measured and used to calculate a rate constant. It is proposed that each of these rate constants represent different reactions.

The influence of temperature on the reaction rate constants for surface spinel and internal spinel formation is shown in Fig. 35. There was a difference of 2 orders of magnitude between the reaction rate constant for spinel formed at the surface of the specimens and for spinel formed inside the dense, crack-free parts of the specimen. Even though there is considerable scatter in these data, the extreme difference in these rates clearly shows that two different mechanisms are operating.

Also apparent from Fig. 35 is the absence of any impurity effects in either the surface or internal reaction rate constants. The rates are essentially the same (within experimental scatter) for nickel chromite formed from pure chromium oxide and high purity, commercial purity, and manganese-doped nickel oxide. In addition, it is apparent that the rates of surface and internal spinel formation are the same for single crystal specimens as for dense polycrystalline specimens. No data for the reaction of silicon-doped nickel oxide with chromium oxide are shown, because the reaction layers consisted entirely of two-phase mixtures of nickel chromite and chromium oxide. Since this type of structure was significantly different from those observed with other specimens, a reaction rate constant was not determined. Also shown in Fig. 35 is the parabolic reaction rate constant determined for the formation of nickel chromite from chromium-saturated nickel oxide. This rate is considerably greater than the surface reaction rates, as would be expected. It is apparent from Fig. 35 that the temperature dependence of the internal and surface spinel reaction constants are similar. A least squares fit through the data reveals that the temperature dependences are:

$$k_p \text{ (surface)} = 1.04 \exp(-76.4 \times 10^3/RT)$$

$$k_p \text{ (internal)} = 3.26 \times 10^{-4} \exp(-68.3 \times 10^3/RT)$$

Measurements of the internal spinel formed at cracks were not used to calculate rate constants, because the thickness of the layer

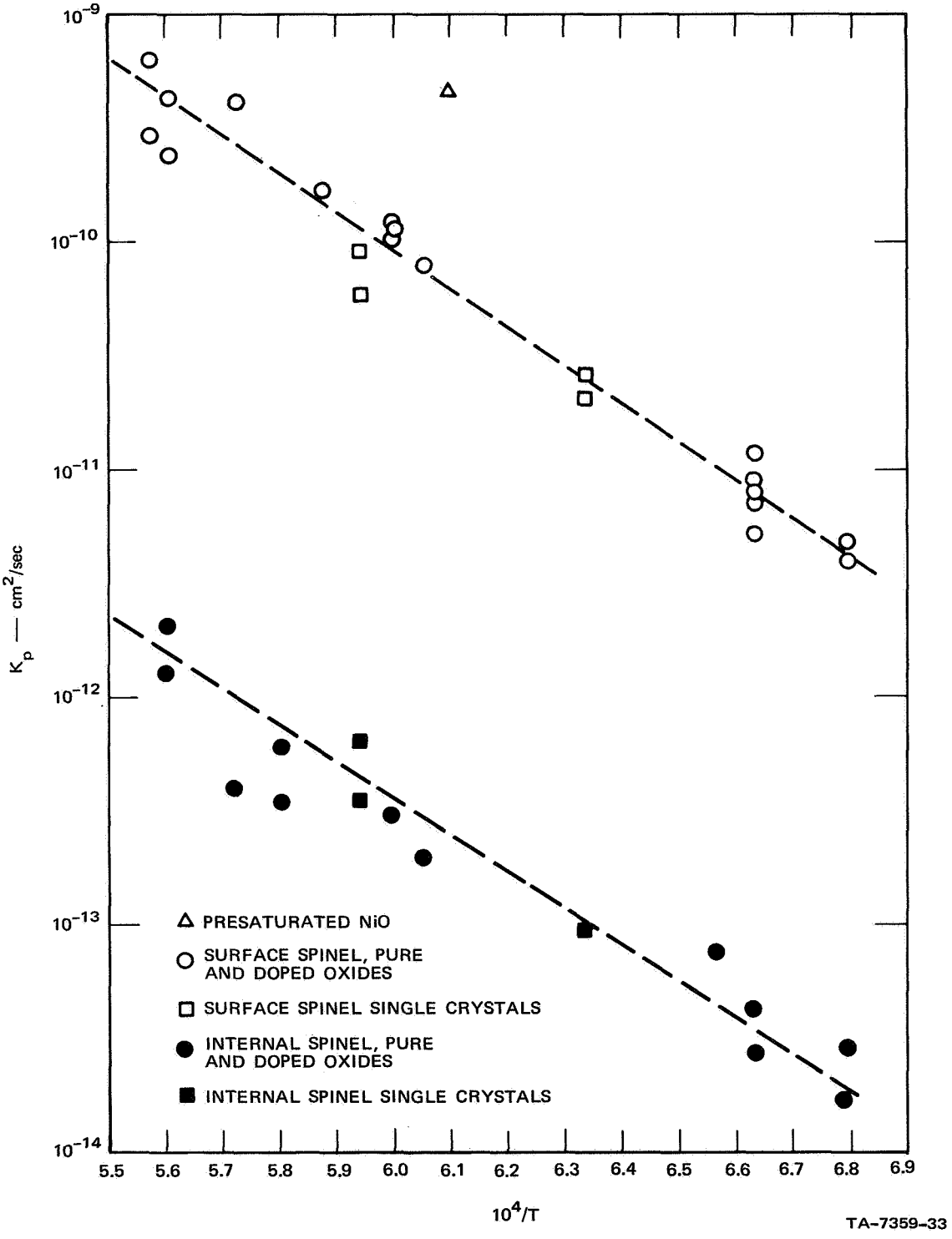

FIGURE 35 PARABOLIC RATE CONSTANTS FOR NICKEL CHROMITE FORMATION

was very dependent on the geometry of the crack. In general, however, the spinel layers formed at cracks were the same order of magnitude as the spinel layers formed at the surfaces. In addition, the thicknesses of the spinel layers formed at thick platinum markers were not used to calculate rate constants, since these thicknesses were highly dependent on the thickness of the marker and its freedom from defects. Qualitatively, however, the rate constants (or thicknesses) were intermediate between the rate constants for surface spinel formation and for internal spinel formation.

The temperature dependence of the rate constants for interface motion with respect to the markers is shown in Fig. 36, and is functionally described by

$$k_{marker} = 2.20 \times 10^{-2} \exp(-67.5 \times 10^{3}/RT)$$

This equation was determined by a least squares fit through the data. The activation energy for the nickel oxide/nickel chromite interface motion is identical to that for internal spinel formation, and does not appear to be significantly affected by oxide composition or by the crystalline structure of the starting material.

E. Cobalt Chromite Formation from Pure Oxides

1. Surface Features

The surface structures observed in cobalt chromite diffusion couples were identical to those observed in the nickel chromite specimens: non-uniform shrinkage of the chromium oxide half of the diffusion couple at the reaction interface, expansion of the cobalt oxide half of the diffusion couple, formation of octahedral crystals of cobalt chromite from the vapor phase, and formation of small crystallites of cobalt chromite on the cobalt oxide far from the reaction interface (Fig. 37). In addition, the frequency of cracking of the cobalt chromite specimens and the locations of cooling cracks, i.e., in the chromium oxide and in the spinel, were the same as in the nickel chromite specimens.

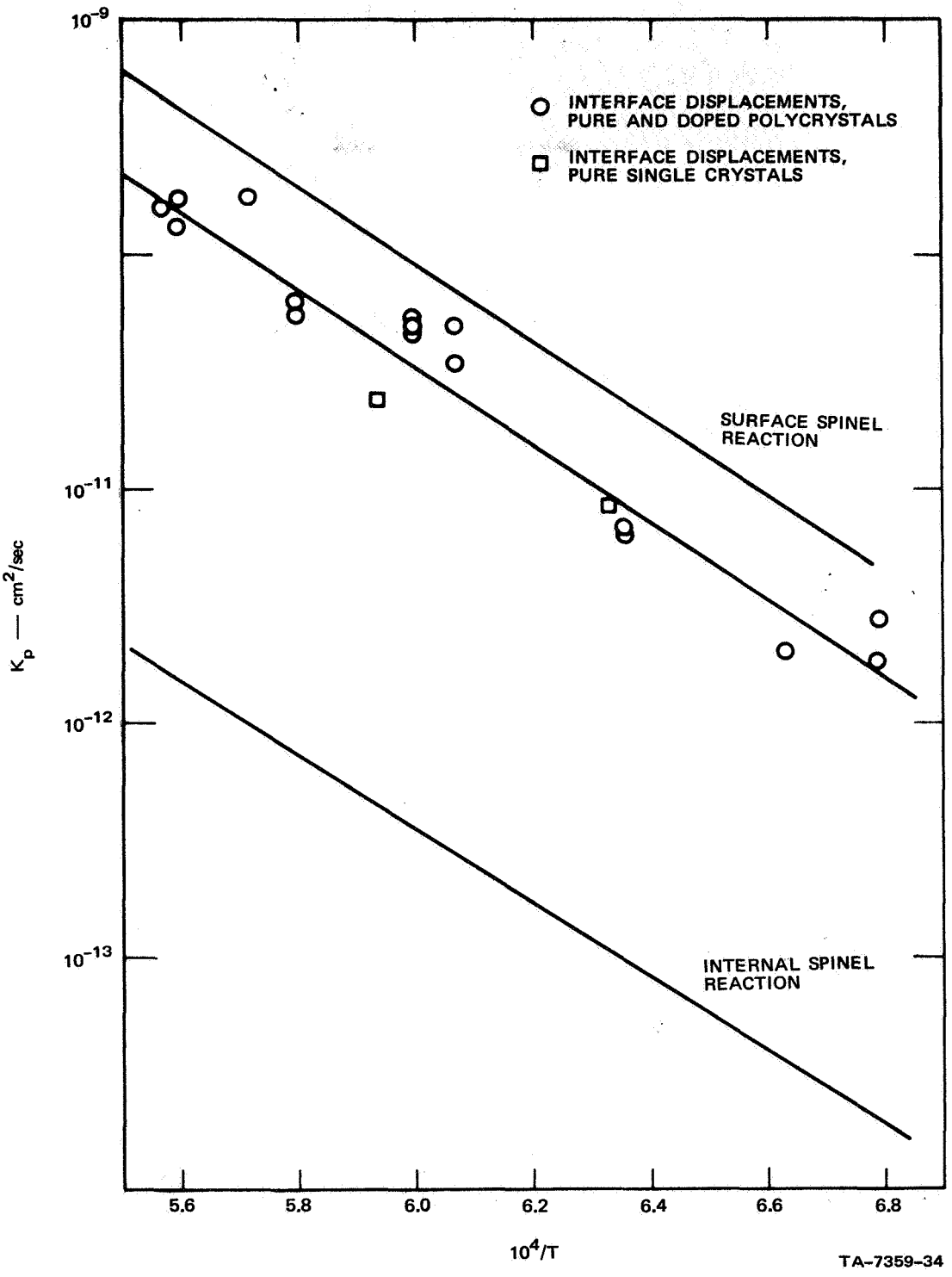

FIGURE 36 INFLUENCE OF TEMPERATURE ON NICKEL OXIDE/NICKEL CHROMITE INTERFACE MOTION DURING SPINEL FORMATION

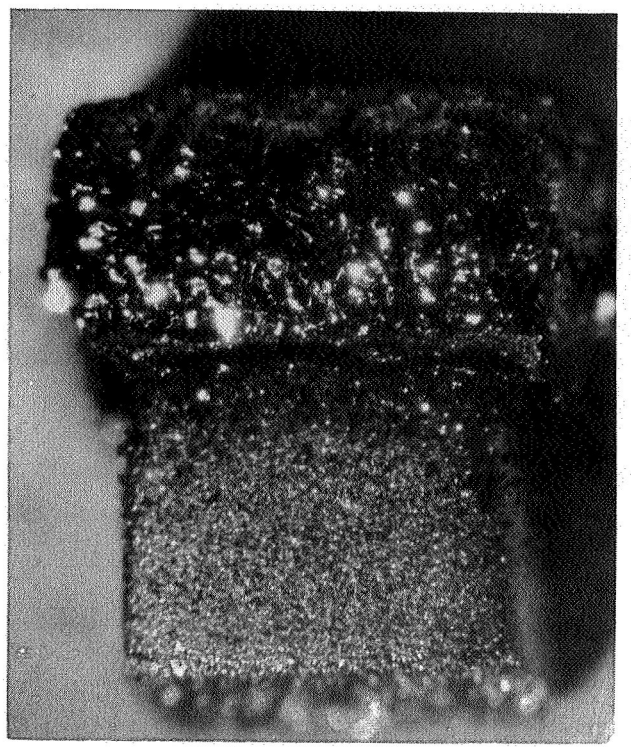

(a)

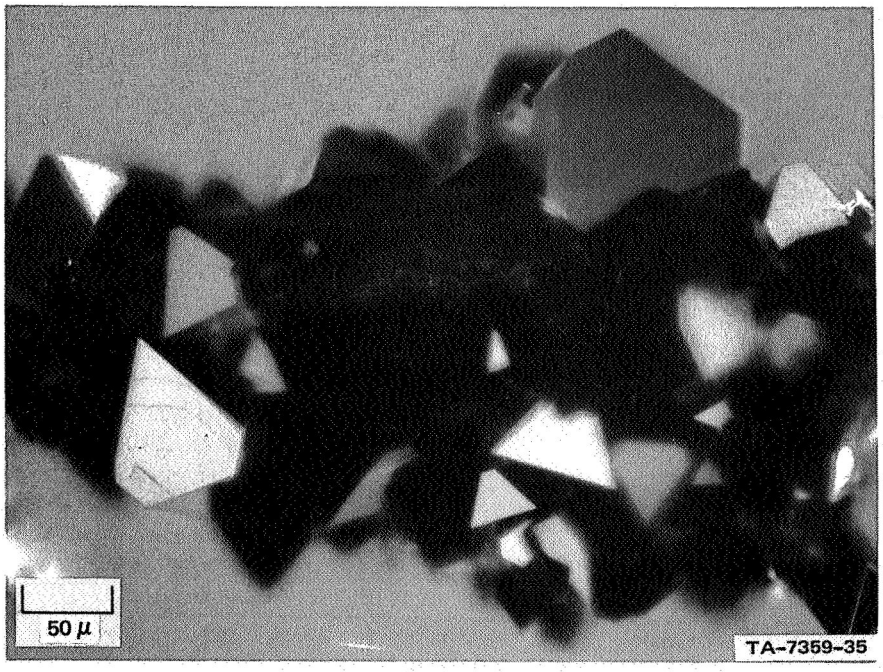

(b)

FIGURE 37 SURFACE STRUCTURE OF COBALT OXIDE/CHROMIUM OXIDE SPECIMEN AFTER REACTION: (a) Nonuniform shrinkage; (b) granular surface crystals are cobalt chromite

2. Internal Features

The internal structures produced in the cobalt chromite experiments were generally similar to the internal structures produced in the nickel chromite experiments. However, there were significant differences. For example, the thickness of the cobalt chromite layer was the same at the surface and within the dense, crack-free region of the pellets (Fig. 38). This structure contrasts with the rapid change in thickness from the surface to the inside of the nickel chromite specimens (see Fig. 12). The measured thicknesses of the cobalt chromite specimens were of the same order of magnitude as the thicknesses that would have formed at the surfaces of the nickel chromite specimens (for the same times and temperatures of reaction), but were 1 to 2 orders of magnitude greater than the internal spinel layers formed in the nickel chromites.

In the cobalt chromite specimens, there was no evidence of thin spinel layer formation at dense, crack-free regions of the pellets. It is also evident from Fig. 38 that the major cracks (parallel to the reaction interface) formed in the two-phase chromium oxide/cobalt chromite layer. In general, cracks observed at this location or within the single phase spinel layer were parallel to the reaction interface. Cracks in the cobalt oxide were generally perpendicular to the reaction interface. A more detailed structure of the internal reaction interface is shown in Fig. 39. All three phases, cobalt oxide, cobalt chromite, and chromium oxide, are dense and pore-free after the reaction. The cobalt oxide contains a high concentration of fine (approximately 1 μ) precipitate particles that will later be shown to be cobalt chromite. The interface between the cobalt oxide and the spinel is scalloped (but planar to ± 3 μ). The spinel layer itself is dense (with the exception of apparent porosity caused by polishing damage) and can clearly be seen to be polycrystalline. Although not evident in Fig. 39, the grain sizes of the spinel and

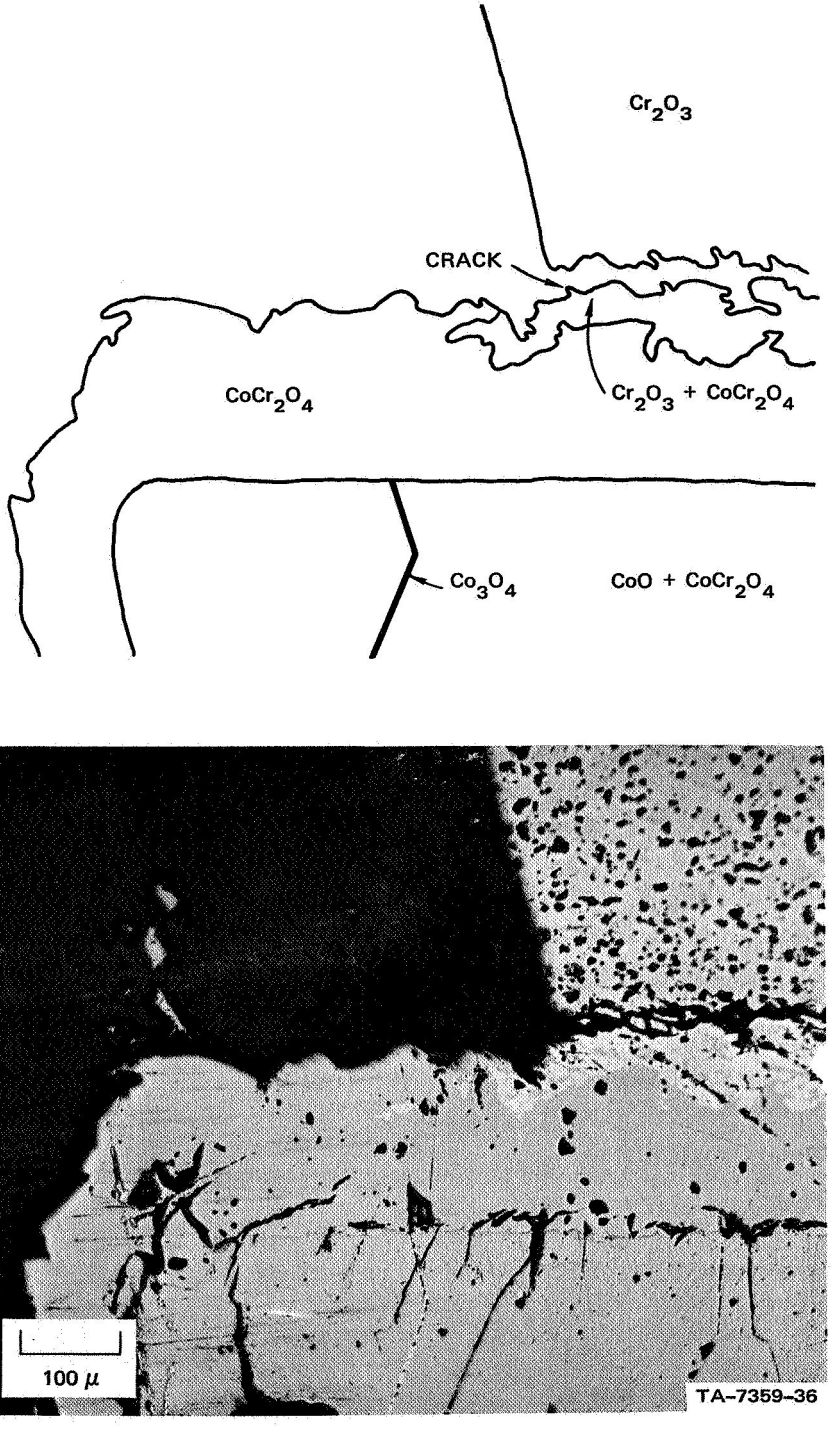

FIGURE 38 SURFACE AND INTERNAL COBAL CHROMITE SPINEL FORMATION

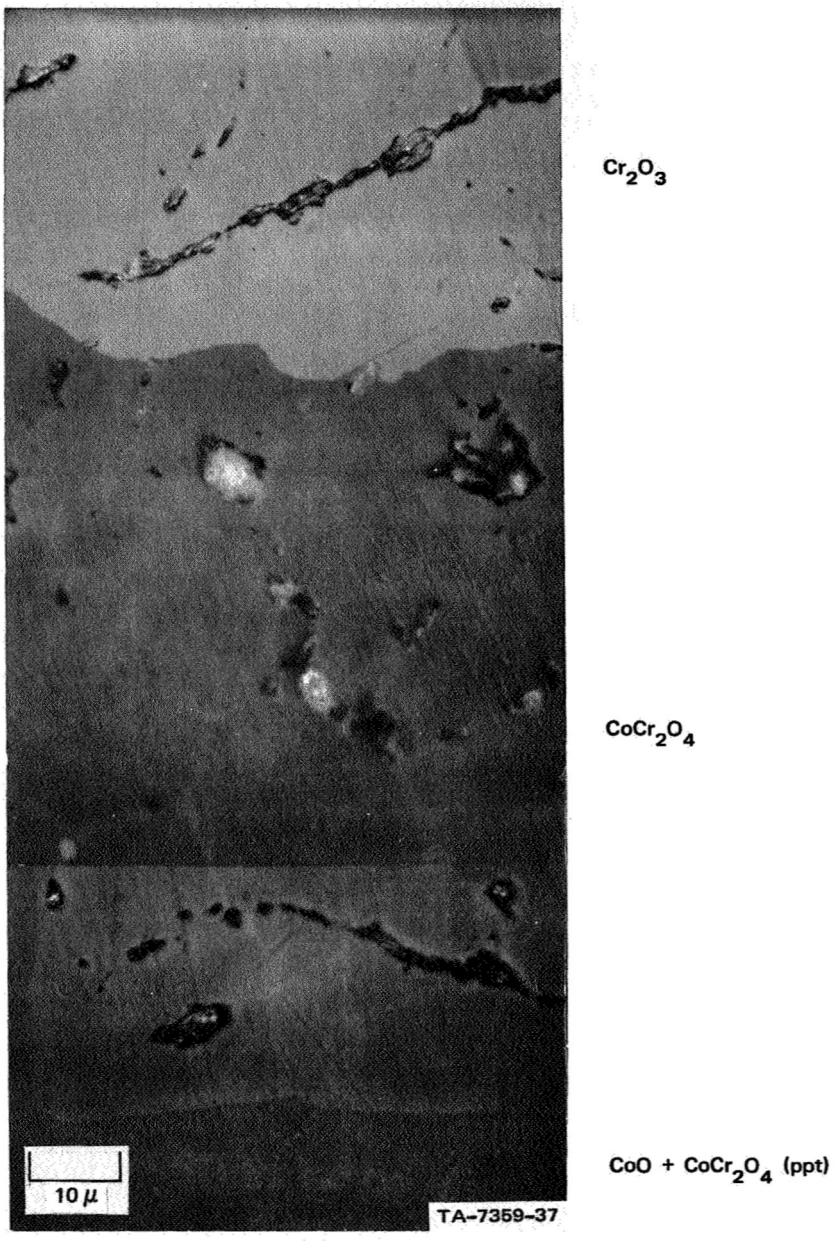

FIGURE 39 REACTION INTERFACE FORMED AT LOW TEMPERATURE (1300°C)

the chromium oxide were the same. The interface between the spinel and the chromium oxide is nonplanar; in other areas of the specimen, intergranular penetrations of cobalt chromite in the chromium oxide were 40 μ deep. In specimens formed at higher temperatures (1500 versus 1300°C), the reaction interface was different only in degree. Figure 40 shows that the interface between the cobalt oxide and the spinel is strictly planar, and the precipitates in the cobalt oxide are larger (approximately 2-4 μ in diameter). The greatest structural difference, however, is the extensive intergranular penetration of the spinel into the chromium oxide. The penetrations by the spinel are totally intergranular, and the chromium oxide is slowly being reacted to form spinel. At the highest temperatures used in these studies, the depth of penetration of the two-phase (spinel plus chromium oxide) layer was equal to the thickness of the single-phase spinel layer.

3. Phase Analysis and Identification

The preliminary identifications of the various phases present after the reaction of cobalt oxide and chromium oxide pellets were confirmed by a combination of X-ray diffraction and electron microprobe techniques. The results of the X-ray diffraction measurements (see Fig. 41) proved that the dark layer between the starting oxides was cobalt chromite. The X-ray data did not show strong evidence that the precipitates in the cobalt oxide were cobalt chromite, but did show that the apparent spinel thickness was about 80 μ greater than that measured optically. This thickness indicates that the precipitates in the cobalt oxide were chromite. However, the conclusion was tentative because of the limitations of the experimental technique. Qualitative electron microprobe examination with X-ray image photographs (Fig. 42) revealed the chromium and nickel distribution across the reaction interface. These photographs emphasized the irregular nature of the spinel/chromium oxide interface, but did

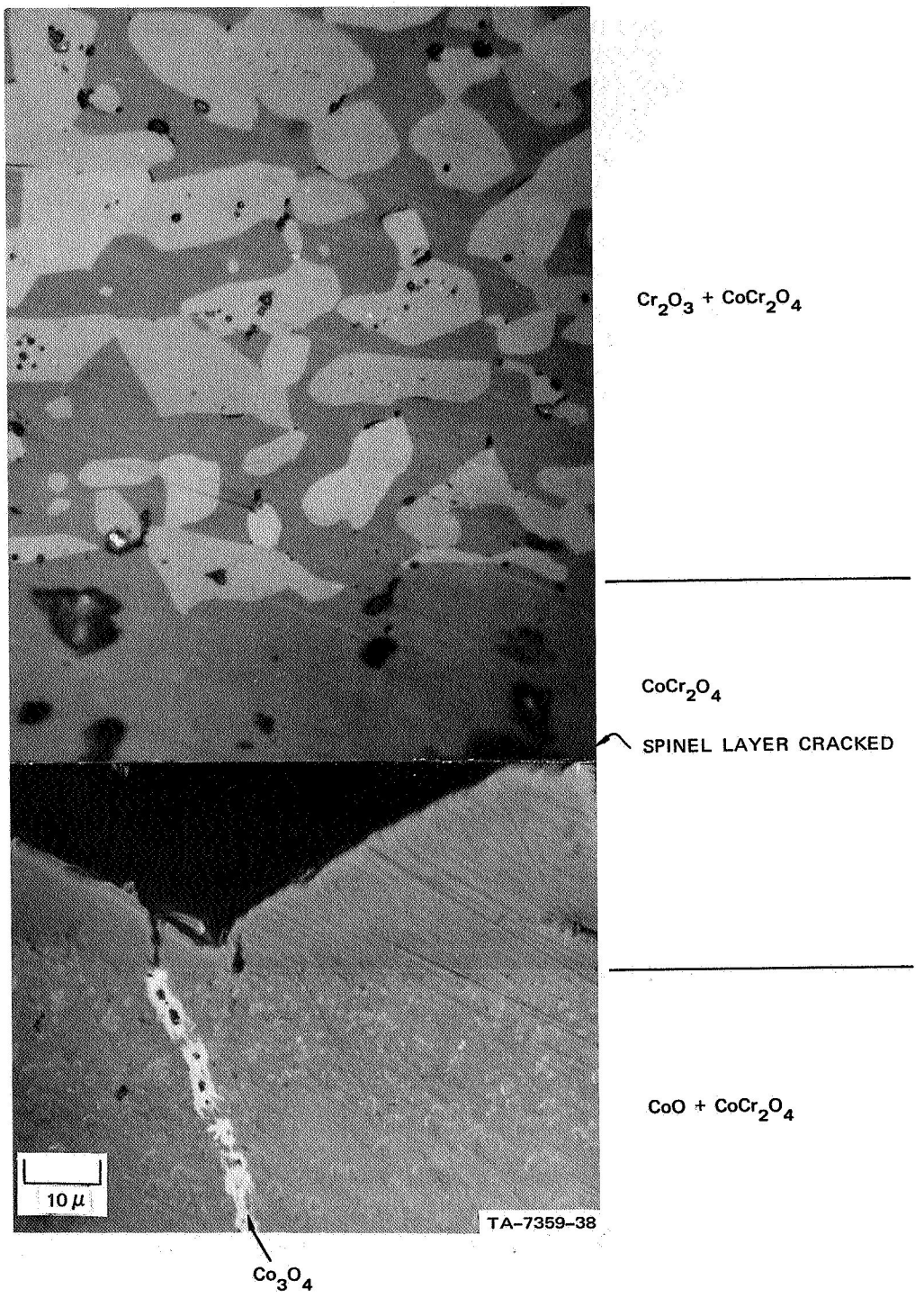

FIGURE 40 REACTION INTERFACE FORMED AT HIGH TEMPERATURE (1475°C)

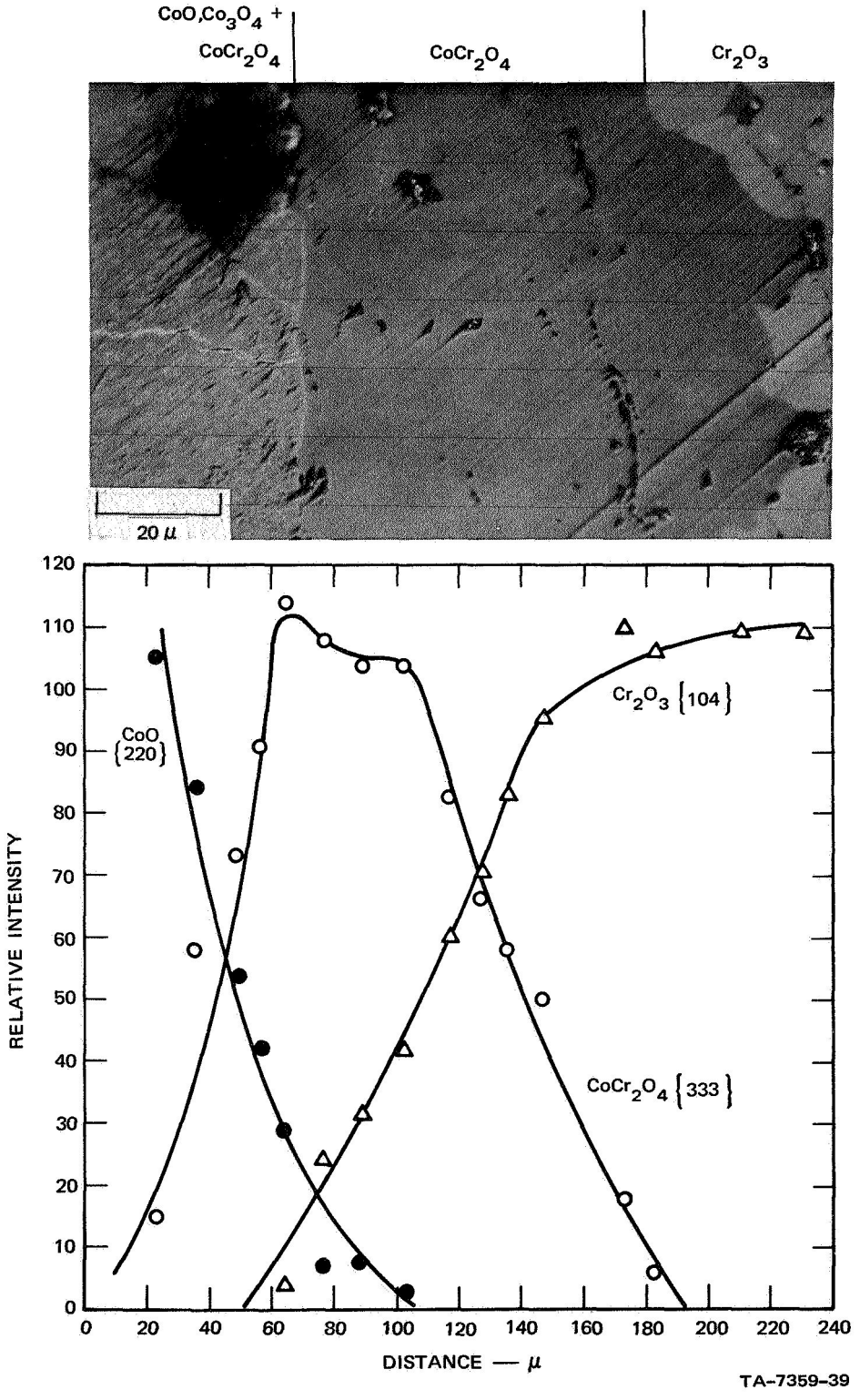

FIGURE 41 STRUCTURE AND PHASE ANALYSIS OF REACTION ZONE FORMED AT INTERFACE DURING COBALT CHROMITE FORMATION

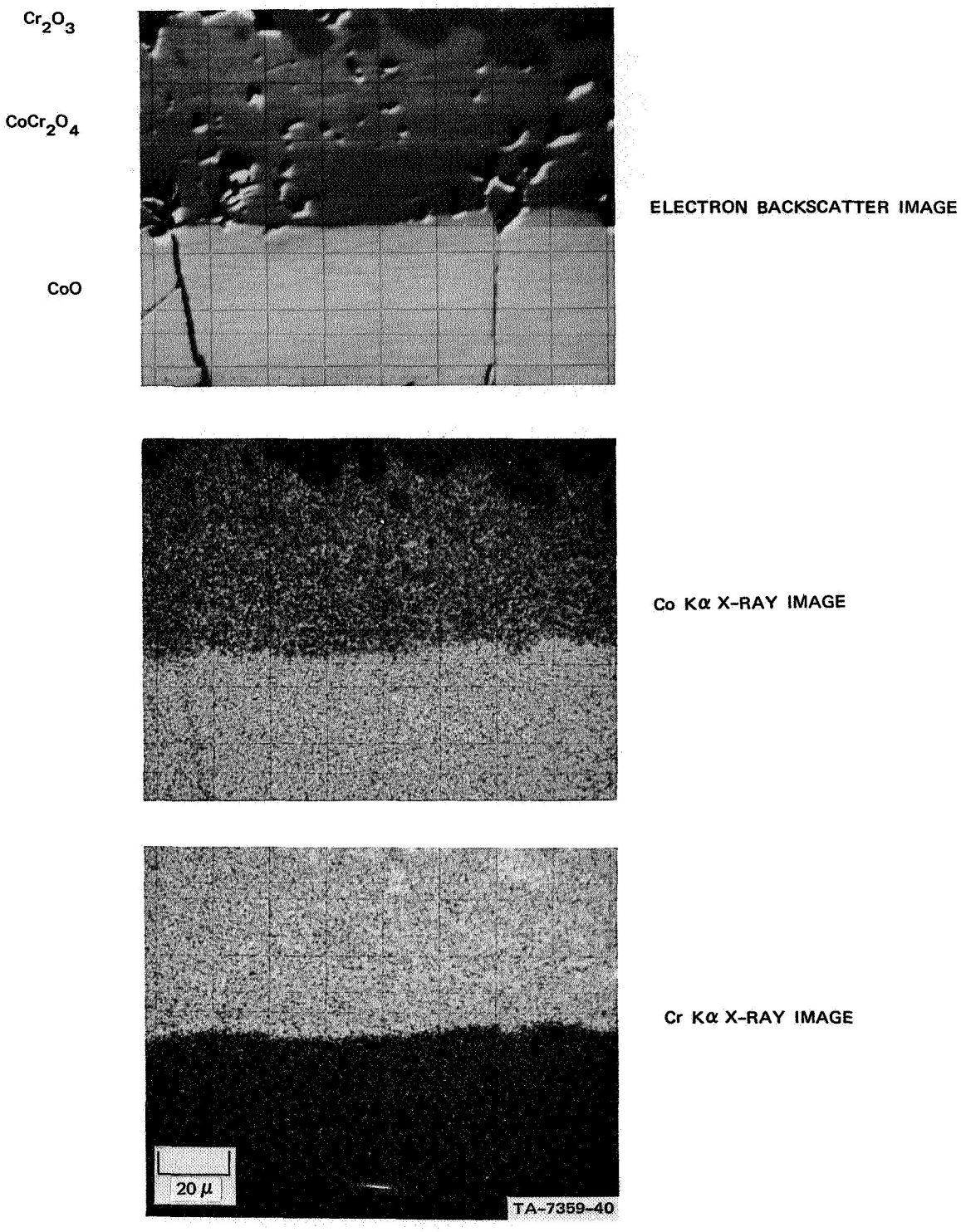

FIGURE 42 STRUCTURE AND COMPOSITION OF COBALT CHROMITE REACTION INTERFACE

not resolve any chromium-rich regions in the cobalt oxide. Since the specimens for these examinations had been formed at relatively low temperatures (1235°C), the sizes of the precipitates would have been near the resolution limits of the X-ray image technique. Line profile scans across the reaction layer (Fig. 43) did show that there was slight chromium enrichment of the cobalt oxide adjacent to the spinel layer.

These results, along with the data to be presented in the following sections, proved that the precipitates in the cobalt oxide were cobalt chromite. The X-ray line profiles of Fig. 43 also revealed concentration gradients of chromium and cobalt in the spinels. These concentrations will be required for the comparison of theoretically and experimentally determined parabolic rate constants.

4. Single Crystal Experiments and Marker Behavior

As with the nickel chromite studies, experiments with single crystals of cobalt oxide and chromium oxide were performed for comparison with the behavior observed in dense, polycrystalline specimens. In these reactions, single crystals of cobalt oxide were sandwiched between and simultaneously reacted with dense polycrystals and single crystals of chromium oxide. The structure of the reaction interface between dense polycrystalline chromium oxide and a single crystal of cobalt oxide is shown in Fig. 44. From the backscattered electron and the X-ray image photographs, it is evident that the reaction interface between the spinel and the chromium oxide is highly irregular, and the reaction interface between the cobalt oxide and the spinel is planar. It is also evident that the precipitates in the cobalt oxide single crystal are chromium rich. X-ray line profile measurements (Fig. 45) reveal that the large precipitates extend 200 μ into the cobalt oxide, and that small precipitates extend another 100 μ. Since these specimens were formed at 1410°C,

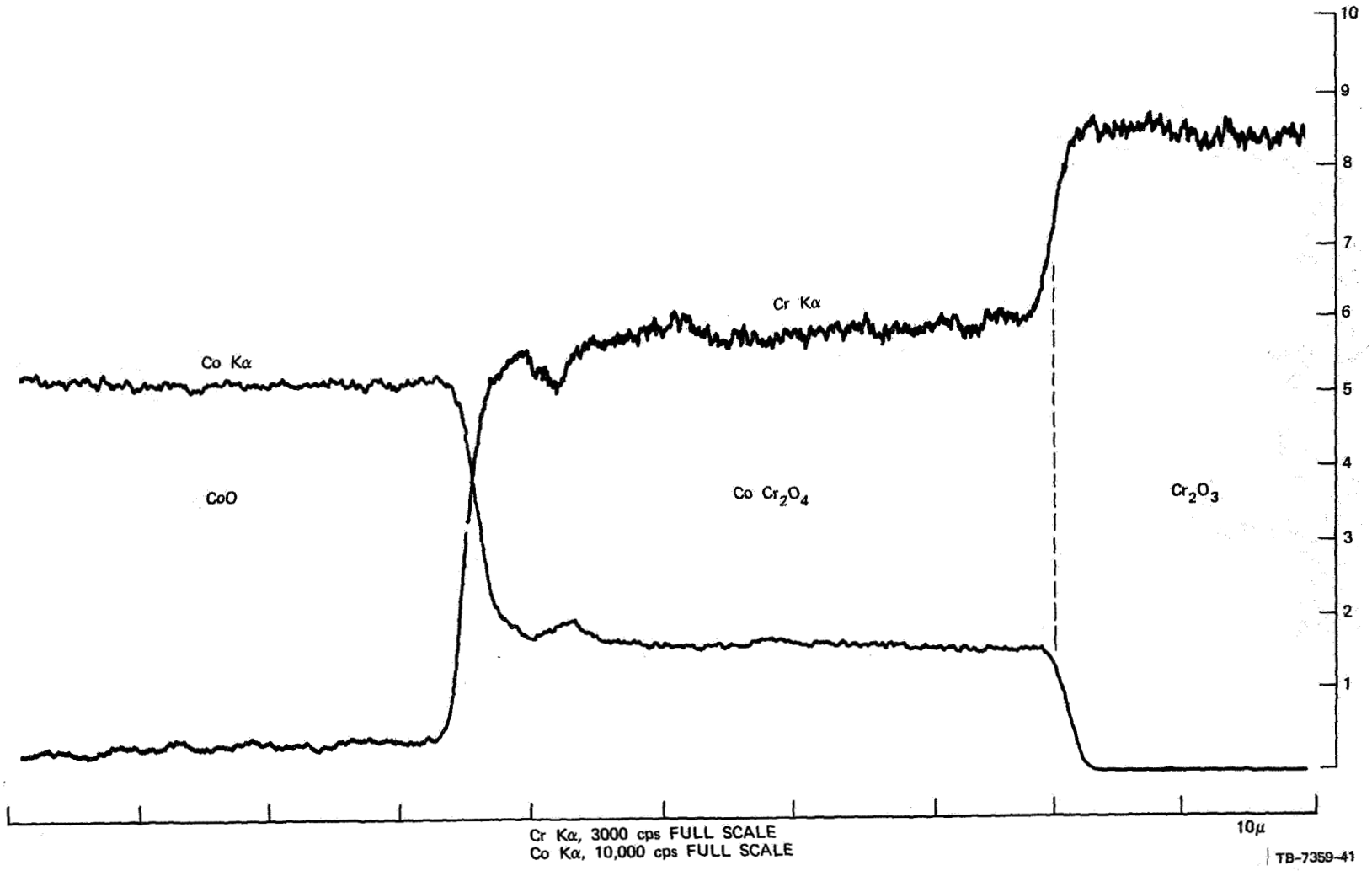

FIGURE 43 COMPOSITION PROFILE ACROSS COBALT CHROMITE REACTION INTERFACE PROFILE ACROSS LAYER SHOWS A LINEAR COMPOSITION GRADIENT AND EVIDENCE OF FINE SPINEL PRECIPITATES IN COBALT OXIDE.

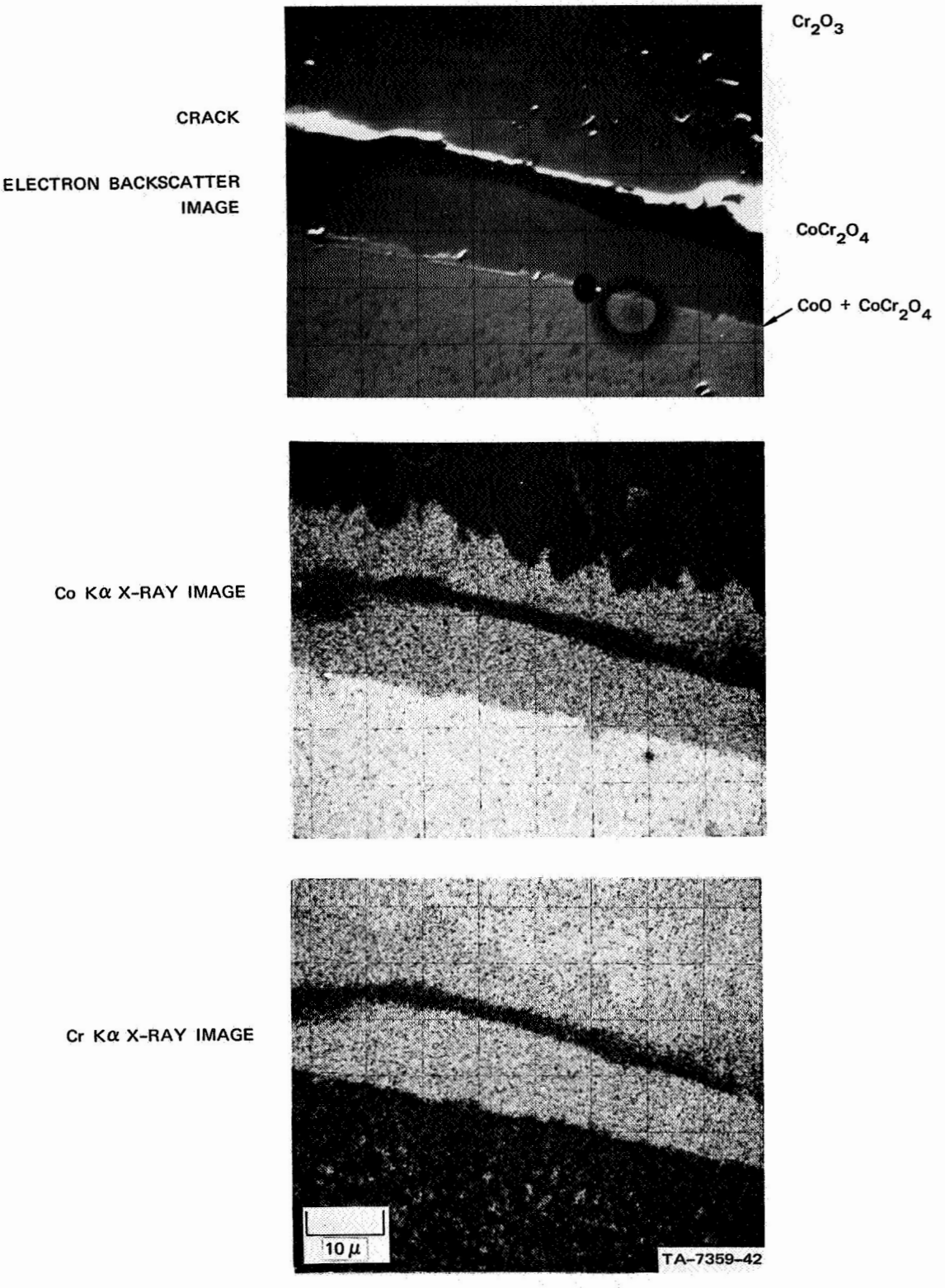

FIGURE 44 COMPOSITION PROFILE ACROSS SPINEL AND COBALT OXIDE (Single Crystal) REACTION INTERFACE SHOWING EVIDENCE OF COARSE COBALT CHROMITE PRECIPITATION IN COBALT OXIDE

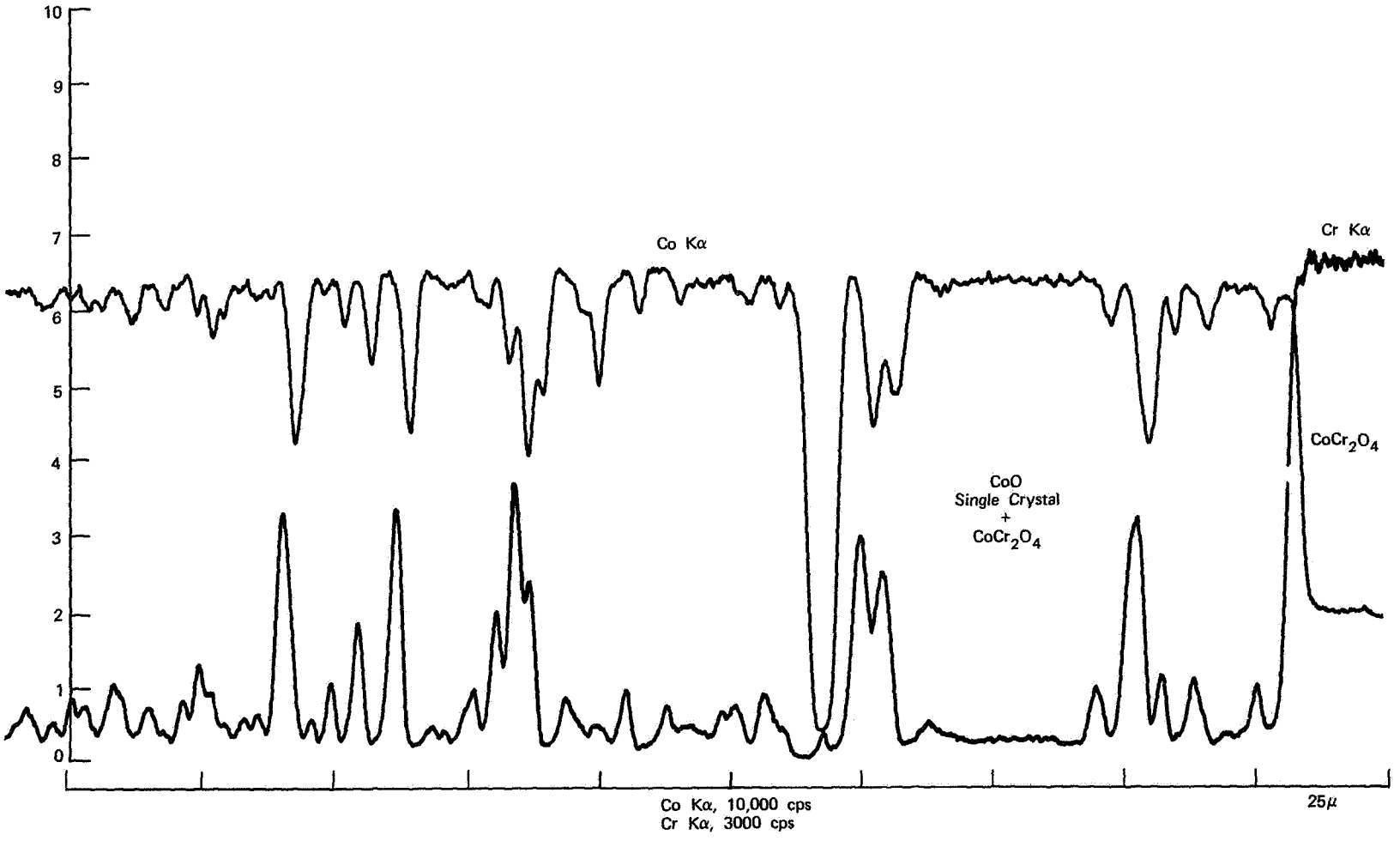

FIGURE 45 COMPOSITION PROFILE ACROSS SPINEL AND COBALT OXIDE (*single crystal*) REACTION INTERFACE SHOWING EVIDENCE OF COARSE COBALT CHROMITE PRECIPITATION IN COBALT OXIDE.

the size of the precipitates and their depth of penetration into the cobalt oxide were greater than observed in Figs. 39, 41, and 42. The apparent chromium content of the precipitates shown in Fig. 45 is only half that of the spinel, since the small size of the precipitate would minimize the probability that the beam would fully rest on a single cobalt chromite particle during the scan.

The reactions of single crystals of cobalt and chromium oxide produced the same features as the reactions of polycrystalline specimens. The significant difference was the formation of a planar reaction interface between the spinel and the chromium oxide single crystal. In these experiments the spinel layer tended to be single crystalline (as evidenced by observation under polarized light). However, some large spinel crystals were observed, particularly in regions near markers.

Careful examination of the single crystal specimens revealed a number of other structural features. Figure 46 shows a distinct difference in the size of the precipitates in the cobalt oxide immediately adjacent to the spinel layer and in the bulk of the cobalt oxide crystal. This 20 μ wide fine-precipitate region next to the spinel is indicative of chromium transport from the cobalt oxide back toward the spinel during cooling and before precipitation.

Figure 46 also shows the influence of a thick platinum marker on the spinel/cobalt oxide interface. It is apparent that the marker has remained planar during the reaction in which it was buried in the cobalt oxide single crystal, and that precipitates have formed on both sides of the marker. The observed shape of the cobalt oxide/spinel reaction interface at the defected markers can readily be explained by the same mechanism proposed for nickel chromite formation (see Fig. 26). It is evident from such an explanation that the greatest distance between the spinel interface and the marker occurs

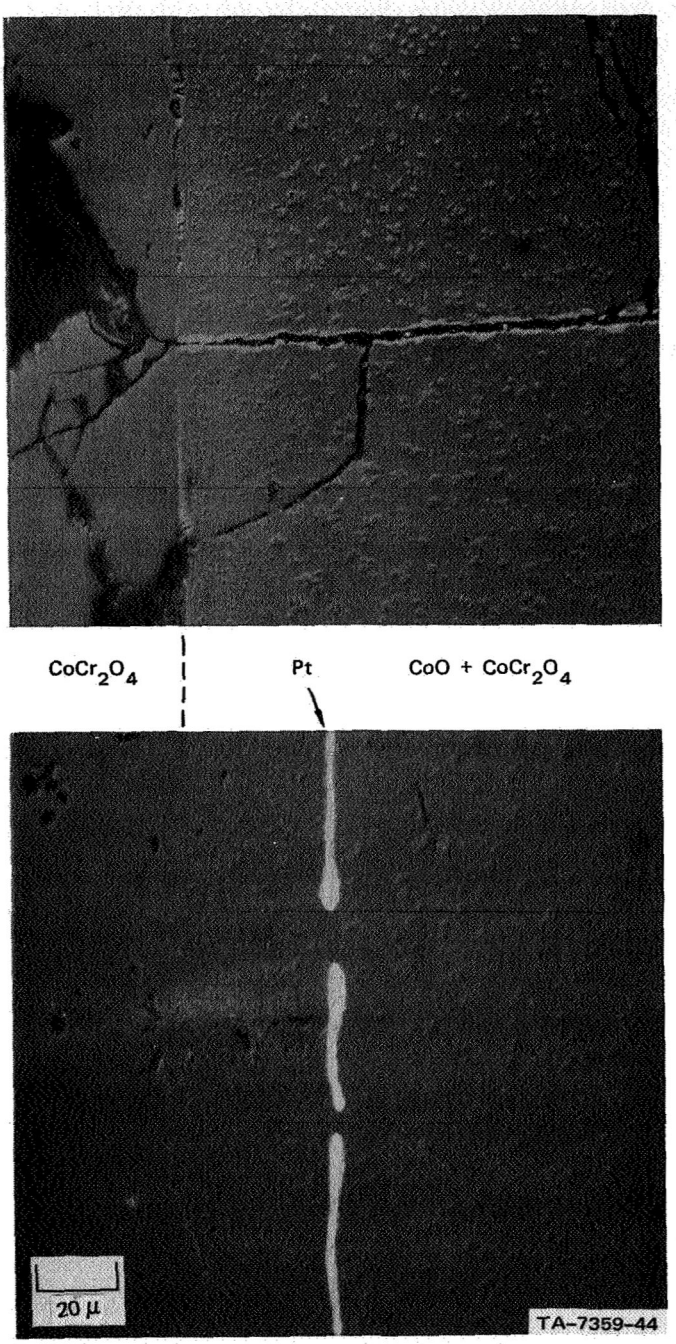

FIGURE 46 MICROSTRUCTURE OF COBALT CHROMITE/COBALT OXIDE (Single Crystal) REACTION INTERFACE. Platinum marker produces a nonplanar interface.

where the earliest defect appeared in the marker. As with the nickel chromite experiments, no dissolution or disappearance of the markers was observed.

A qualitative proof that there is little or no marker dissolution is given by the X-ray image photographs of Fig. 47. Further evidence that the marker behavior in cobalt chromites was the same as in the nickel chromites is furnished by Fig. 48. Early stages in the reaction of dense, polycrystalline specimens are shown in which intrusions of cobalt oxide into the spinel have formed at marker defects. These intrusions prove that chromium is soluble in cobalt oxide at high temperatures, and that countercurrent diffusion of cations has occurred in the cobalt oxide during the reaction to form cobalt chromite. Further, the absence of porosity in the reactants or products in single or polycrystalline specimens shows that all observations should be explainable in terms of cation and perhaps anion transport.

F. Cobalt Chromite Formation from Doped Oxides

A series of experiments were performed with manganese- and silicon-doped cobalt oxides that were reacted with pure chromium oxides. In these experiments, significant impurity effects both on the structure and kinetics of the spinel reactions were observed. In contrast to nickel chromite experiments, impurity effects were easy to separate.

1. Manganese-Doped Cobalt Oxide

The appearance of specimens formed from cobalt oxide doped with 1 mole % manganese oxide was qualitatively the same as the structure formed with pure cobalt oxide. Generally nonplanar interfaces were observed between the spinel and the chromium oxide and planar or semi-planar interfaces between the spinel and the cobalt oxide. The composition of the spinel formed from manganese-doped cobalt oxide

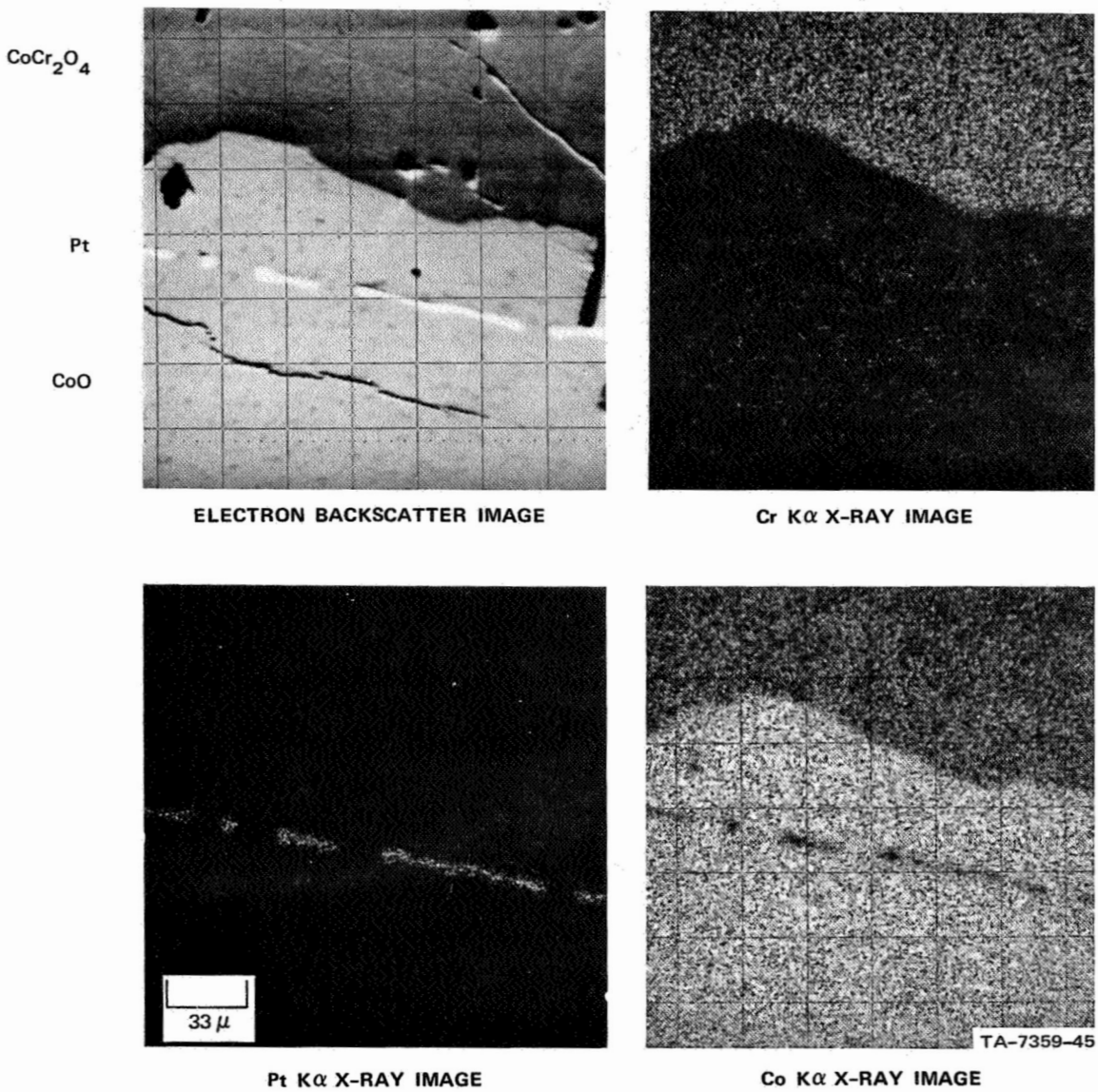

FIGURE 47 SPINEL/COBALT OXIDE (Single Crystal) REACTION INTERFACE

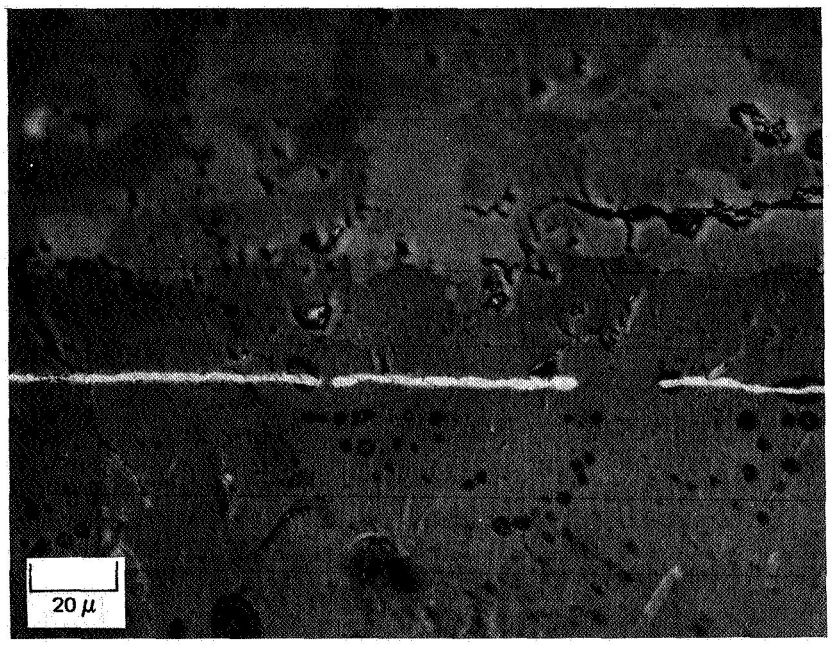

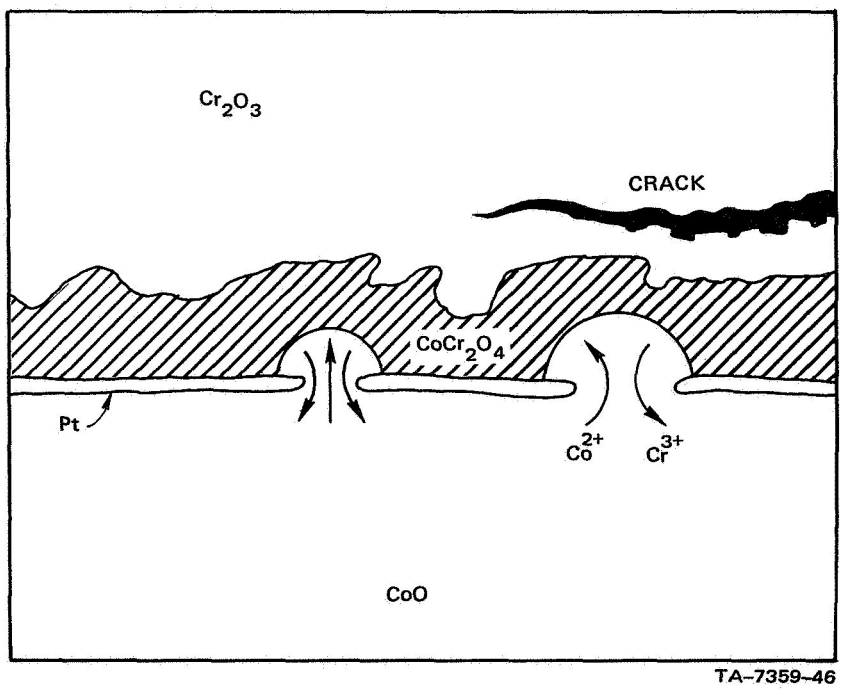

FIGURE 48 EARLY STAGES OF SPINEL DISSOLUTION AT MARKER DEFECTS DURING COBALT CHROMITE FORMATION. The dark circular spots are surface contamination.

is shown in Fig. 49. The electron backscatter image in this figure shows a badly fractured spinel layer. This fracturing is the result of grinding and polishing damage, and is not representative of the general appearance of specimens formed from the manganese-doped cobalt oxide. The X-ray image photographs show that qualitative distributions of chromium and cobalt are the same as in previous spinels, but there appears to be manganese both in the cobalt oxide and in the spinel.

Quantitative X-ray line profile scans across the reaction interface shown in Fig. 50 reveal that there are linear concentration gradients of chromium and cobalt across the spinel layer, and that the precipitates in the cobalt oxide are chromium rich. Also evident in Fig. 50a is the presence of spinel in the chromium oxide. This spinel is the result of intergranular penetrations into the chromium oxide. Figure 50b shows that there is a relatively flat manganese distribution across the spinel layer, and that there is manganese in the spinel formed on both sides of the reaction layer. For example, there is manganese in the spinel penetrations in the chromium oxide (of roughly the same concentration as in the spinel layer itself), and there is a very high concentration of manganese in the spinel precipitates in the cobalt oxide.

In view of the influence of geometry in reducing the apparent concentrations of constituents in the small precipitates, it is probable that the true enrichment of manganese in the precipitates is 2 to 4 times greater than in the single-phase spinel layer. This type of composition profile is significantly different from that produced in the nickel chromites (Fig. 32) and indicates that manganese in the cobalt oxide segregates to and reacts with the incoming chromium ions to form manganese-rich islands. These composition gradients will be considered in the explanation of the influence of the effects of manganese on the spinel reaction kinetics to be described later.

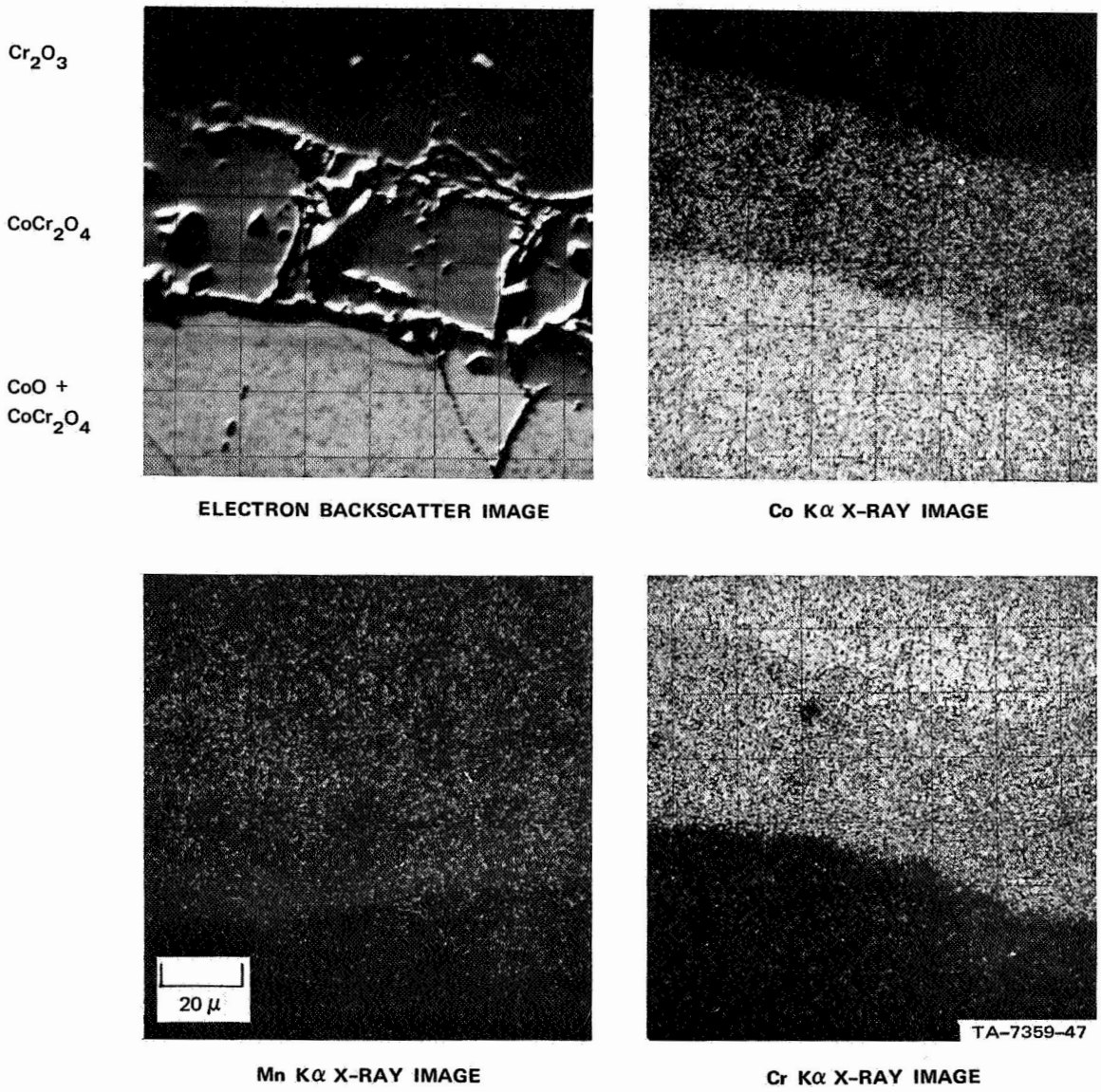

FIGURE 49 STRUCTURE AND COMPOSITION OF COBALT CHROMITES FORMED FROM COBALT OXIDE DOPED WITH ONE MOLE % MANGANESE OXIDE

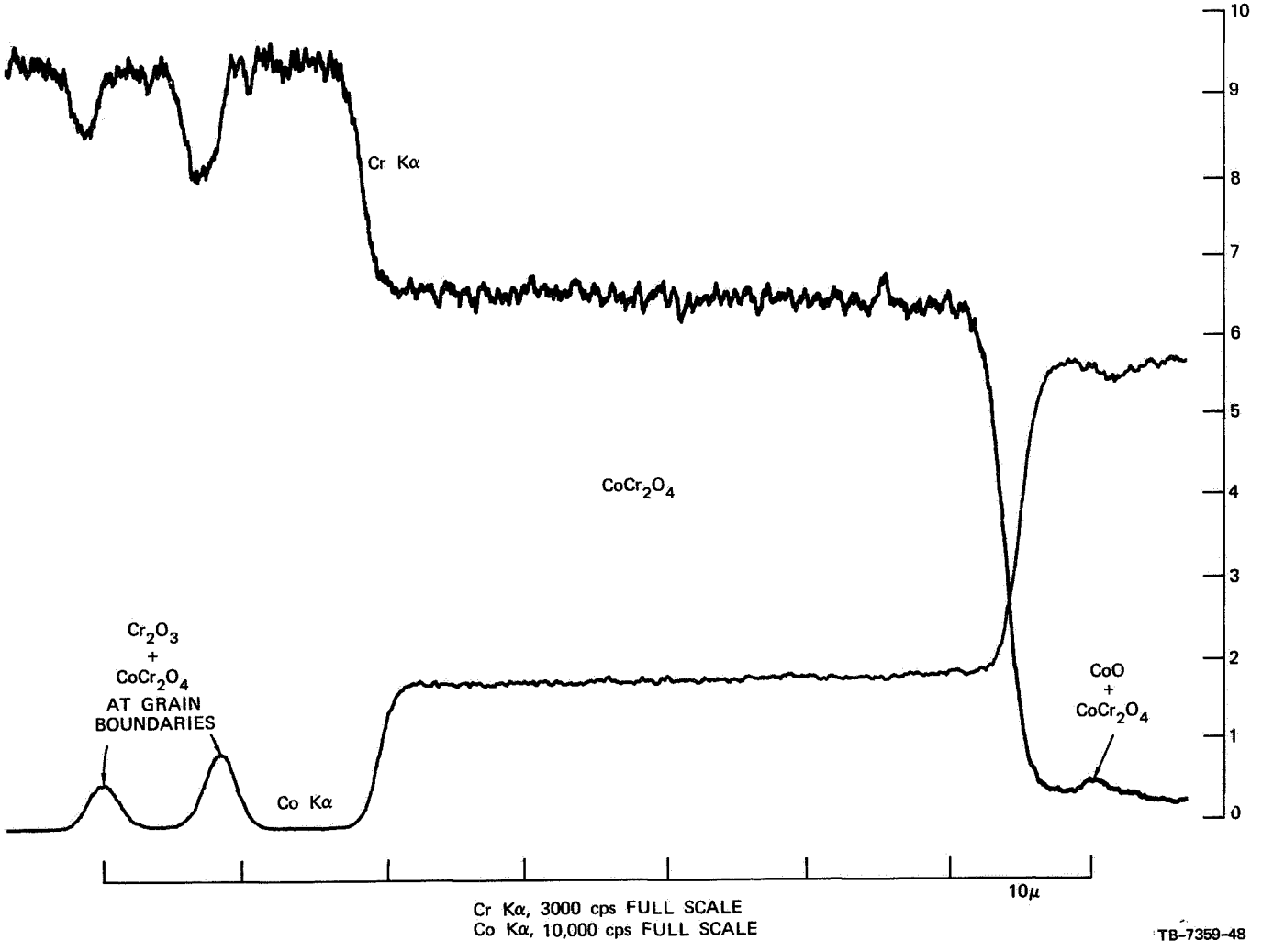

FIGURE 50a CHROMIUM, COBALT, AND MANGANESE COMPOSITION PROFILES ACROSS SPINEL REACTION LAYER:
Spinel precipitation in chromium oxide and cobalt oxide

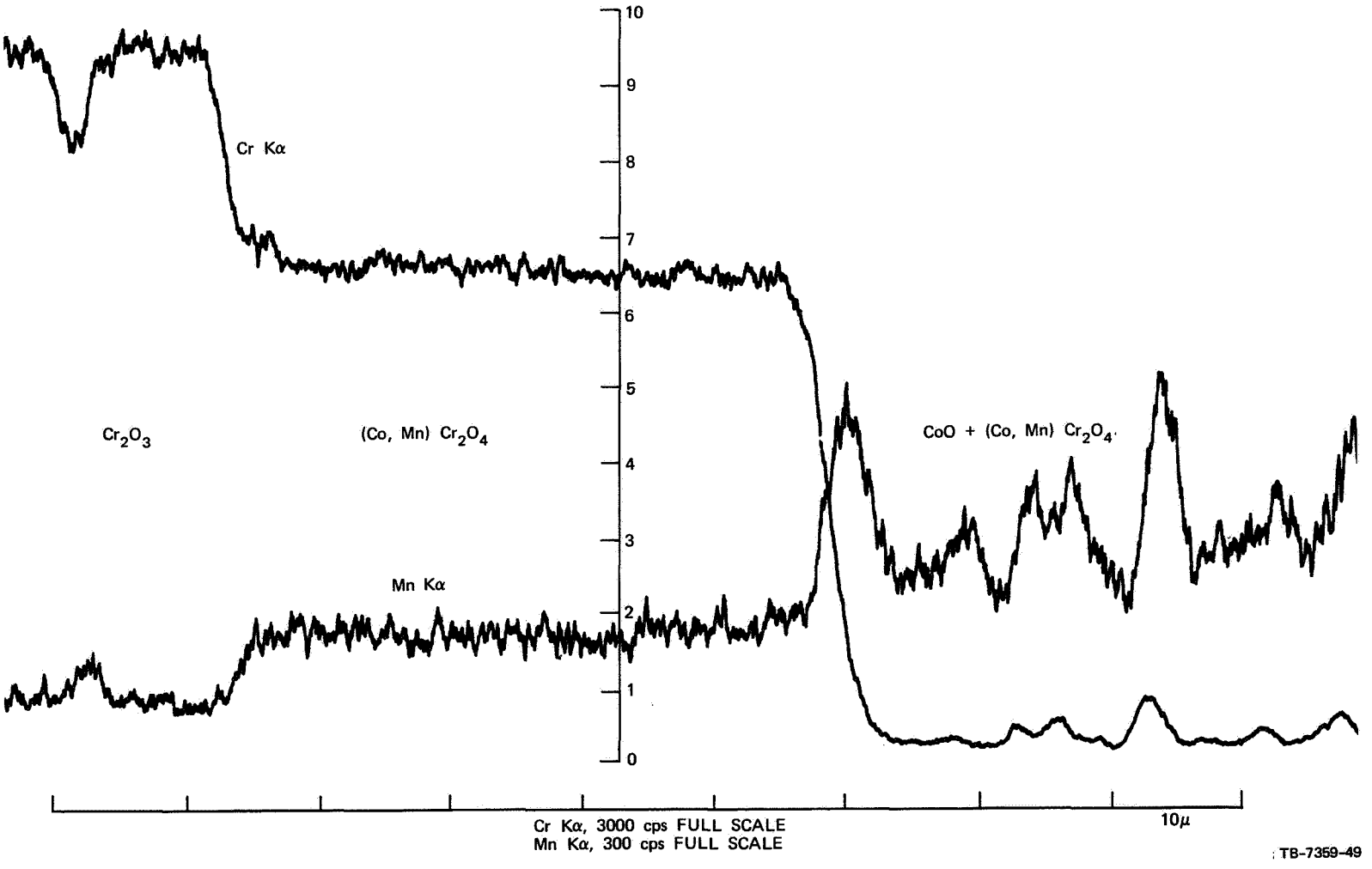

FIGURE 50b CHROMIUM, COBALT, AND MANGANESE COMPOSITION PROFILES ACROSS SPINEL REACTION LAYER:
Manganese enrichment in spinel precipitates in cobalt oxide

2. Silicon-Doped Cobalt Oxide

The influence of silicon additions on the kinetics and structures of spinels formed by the reaction of doped cobalt oxides and chromium oxides was the most dramatic of the impurity effects observed in these studies. The additions of silicon (at the $1\frac{1}{2}$ mole % SiO_2 level) not only increased the reaction rates by about 1 to 2 orders of magnitude, but they also produced unusual structures that were not observed in any of the other specimens.

The structure of a spinel layer formed by the reaction of silicon-doped cobalt oxide with pure chromium oxide is compared in Fig. 51 with the structure produced by the Reaction of manganese-doped cobalt oxide with pure chromium oxides. It is evident that there is a great difference in thickness of the two layers, which were grown simultaneously. More important, however, it is evident that the spinel layer is distinctly two-phase. The layer appears to consist of large crystals of spinel and porosity. This porosity is not real, however; it is the result of the optical properties of a glassy phase in the layer.

It is also evident from Fig. 51 that the interfaces between the spinel layer and the chromium oxide and cobalt oxide are essentially planar. The planarity of the reaction front at the chromium oxide is greater than at the cobalt oxide, indicating that the spinel is growing by penetration of chromium into the cobalt oxide. At higher magnification (Fig. 52), the structure of the large spinel crystals in a dark matrix phase is clearly evident. The very sharp crystal faces of the spinels and the apparent wetting by the matrix phase suggest that the crystals are growing in a liquid or semiliquid phase.

Qualitative X-ray image photographs of the silicon-doped cobalt oxides (Fig. 53) show that there is little or no silicon in the chromium oxide, but there is a high concentration of silicon in the two-phase spinel layer. This silicon is concentrated at the boundaries

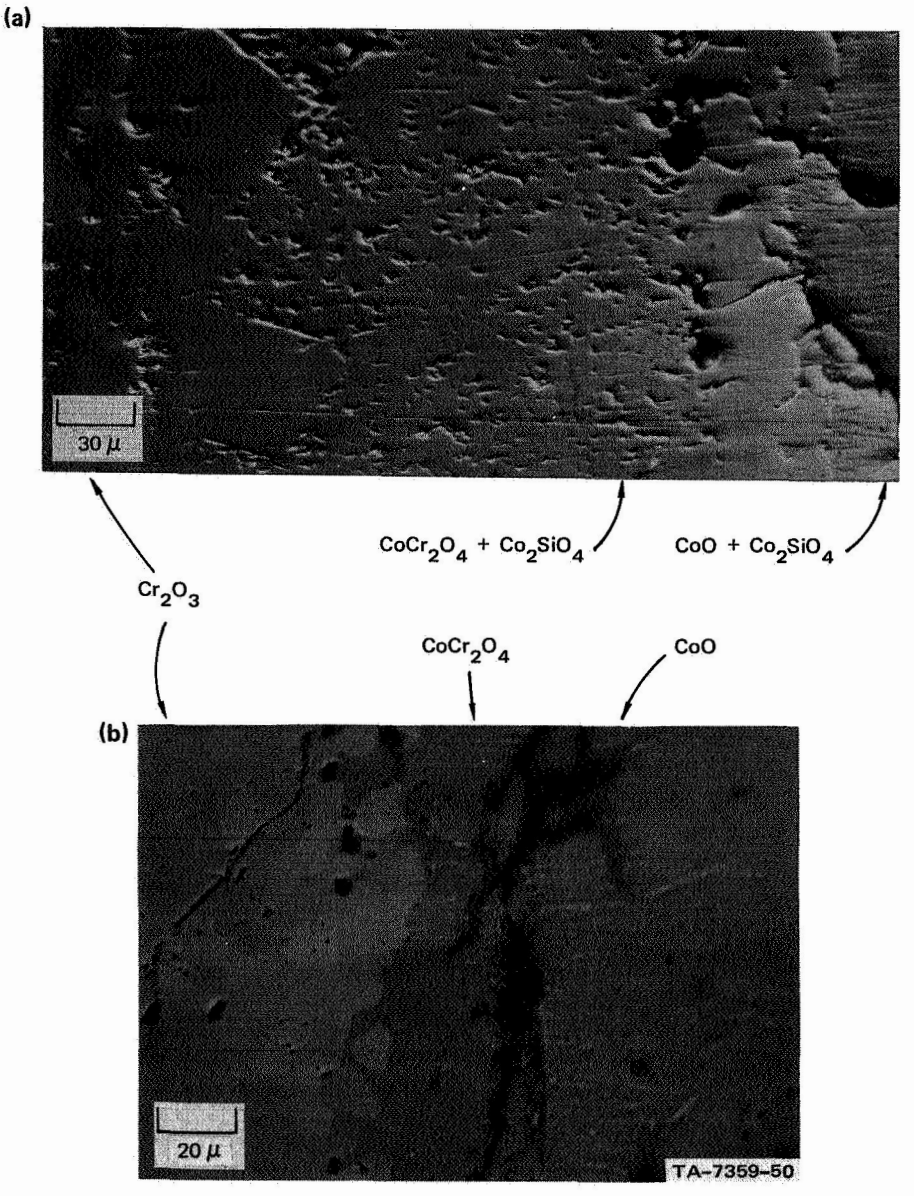

FIGURE 51 STRUCTURE OF COBALT CHROMITE (a) FORMED FROM SILICON-DOPED COBALT OXIDE AND (b) FORMED FROM MANGANESE-DOPED COBALT OXIDE

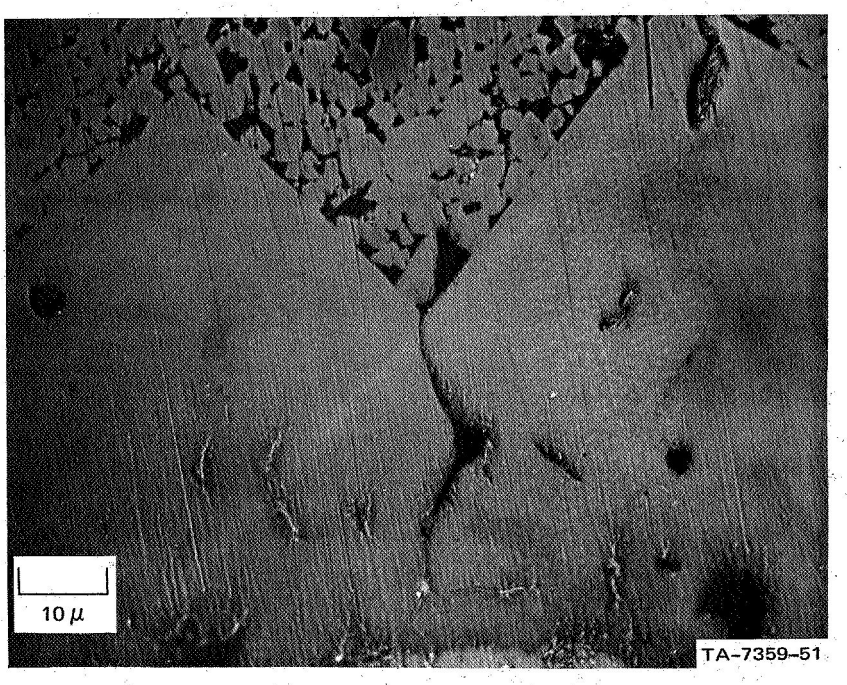

FIGURE 52 DETAILED STRUCTURE OF COBALT CHROMITE CRYSTALS IN COBALT ORTHOSILICATE MATRIX

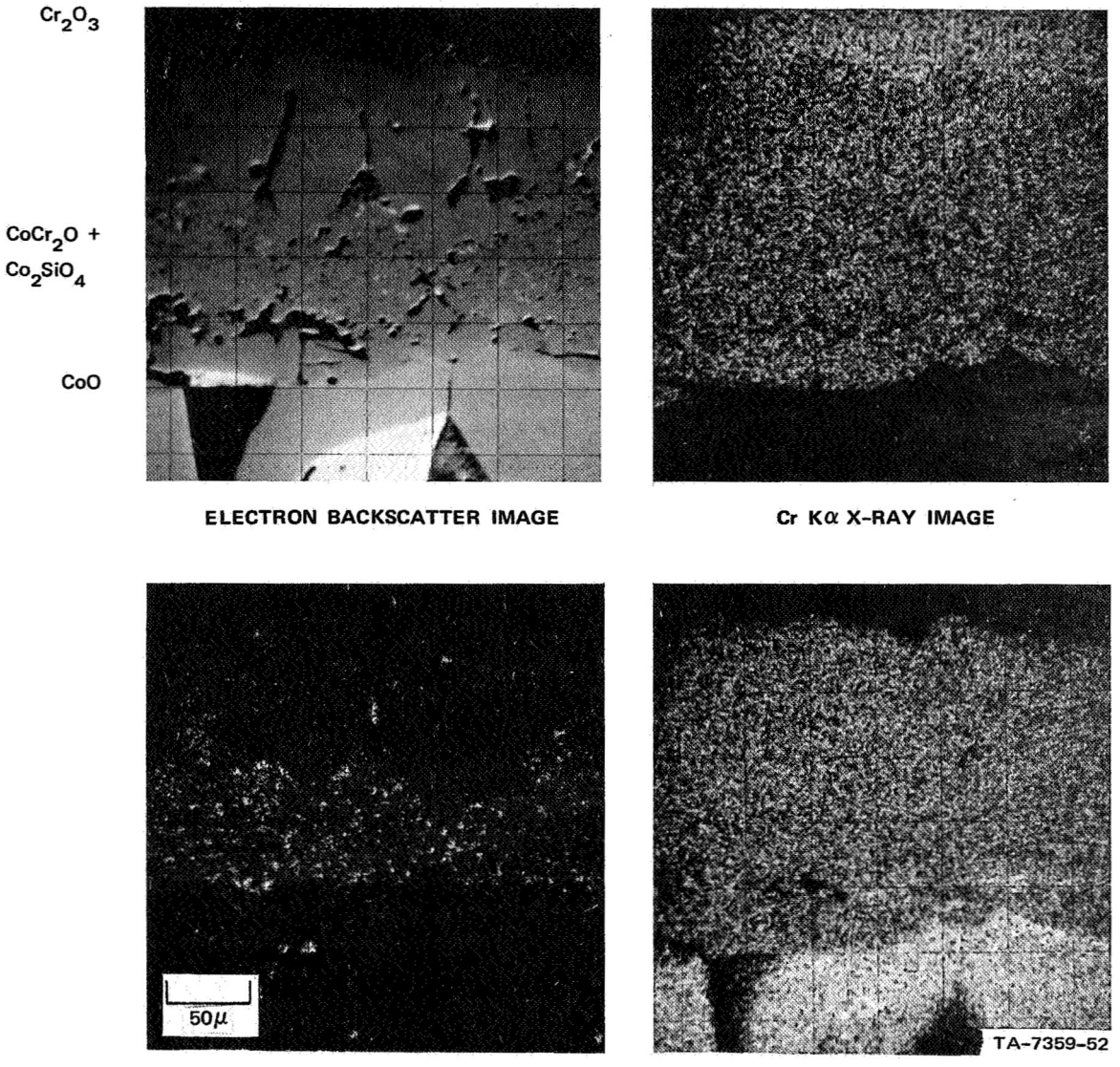

FIGURE 53 STRUCTURE AND COMPOSITION OF COBALT CHROMITE FORMED FROM SILICON-DOPED COBALT OXIDE

of the large spinel crystals, and not within the crystals themselves. The matrix phase in the spinel layer appeared to be the same as the cobalt silicate phase in the cobalt oxide. Samples of the two-phase spinel layer were carefully removed and examined by X-ray diffraction; the results of these measurements showed that only cobalt chromite ($CoCr_2O_4$) and cobalt orthosilicate (Co_2SiO_4) were present.

G. Kinetics of Cobalt Chromite Formation

Preliminary measurements were made of the influence of time at temperature on the thickness of cobalt chromite layers. Figure 54 shows that there is a linear relation between the square of the spinel thickness and time. These observations confirmed earlier reported results that the cobalt chromite reaction rate was diffusion controlled and was described by a parabolic rate constant. As with the nickel chromite reactions, the cobalt chromite rate constants were calculated from measured data and equations 11 or 40. In addition the data of Fig. 54 revealed a significant difference between the reaction rate of the cobalt chromite spinel formed from pure cobalt oxide and the spinel formed from manganese-doped cobalt oxide. This difference in rate constant was observed at all reaction temperatures. As was stated earlier, there were no significant differences in the reaction rates for cobalt chromite at the surface of the specimen or within the bulk of the specimen. Therefore, only data from which rate constants could be determined were the average thickness of the spinel layer and the distance of the cobalt chromite/cobalt oxide interface from the marker. These measurements were sparse, but they were sufficient to establish an important trend.

The temperature dependence of the parabolic rate constants for cobalt chromite formation are shown in Fig. 55. It is immediately evident from this figure that there was much less scatter in the data than for nickel chromite. In addition, it is evident that there was

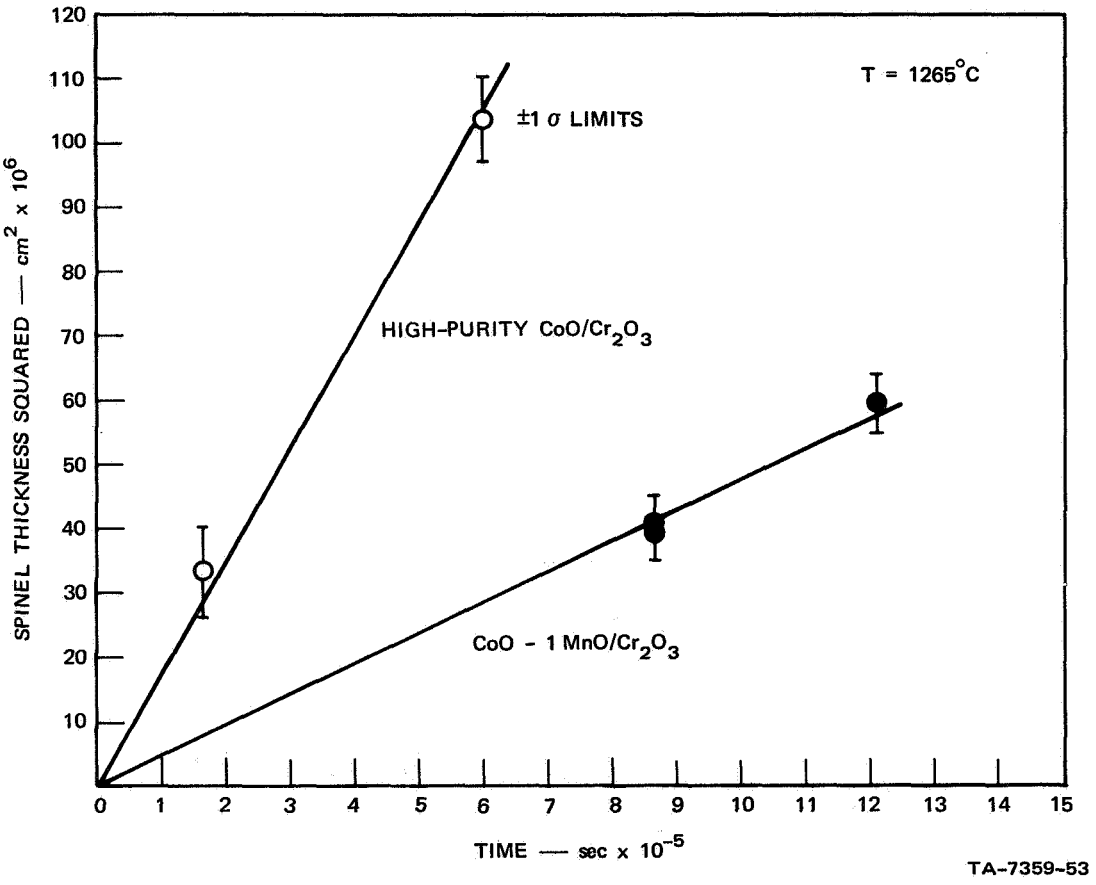

FIGURE 54 COBALT CHROMITE THICKNESS MEASUREMENTS SHOWING PARABOLIC REACTION RATES AND INFLUENCE OF MANGANESE DOPING

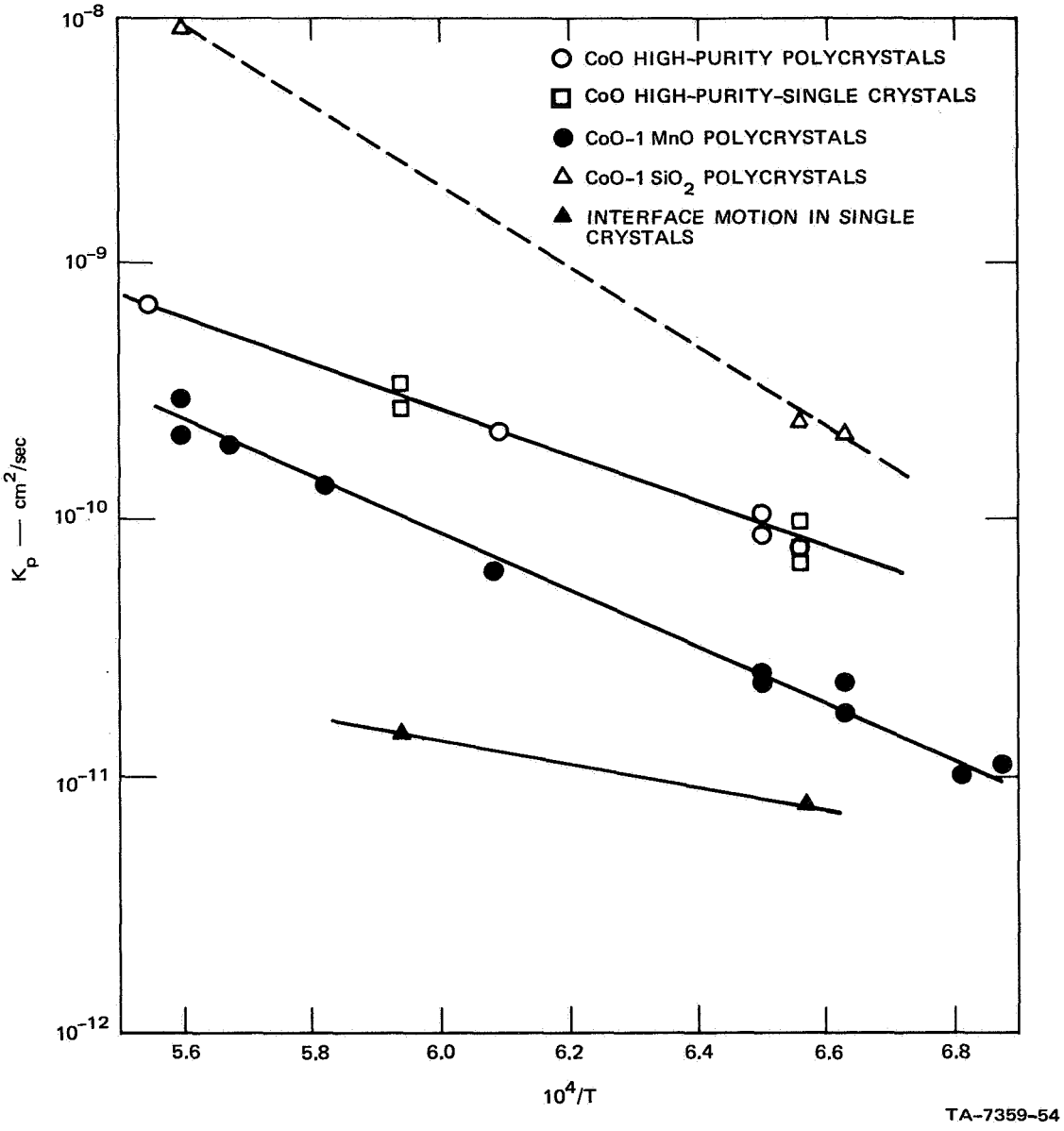

FIGURE 55 INFLUENCE OF TEMPERATURE AND COMPOSITION ON COBALT CHROMITE REACTION RATE CONSTANT

a significant impurity effect, the high purity specimens having rate constants intermediate between the rate constants for manganese-doped specimens and rate constants for silicon-doped specimens.

The spinel formation rate from silicon-doped specimens can be from 10 to 20 times greater than that from manganese-doped specimens. In addition, the rate constants determined from the reactions of high-purity single crystalline specimens were consistent with the rate constants determined from dense polycrystalline specimens. These data show that the experiments are representative of true solid-state reactions rather than vapor-phase reactions. Also shown in Fig. 55 are the rate constants determined from the motion of the interface with respect to the markers from the single crystal experiments. The rate of interface migration is an order of magnitude slower than the rate of spinel formation. These results point to a difference between the mechanisms of spinel formation of cobalt chromites and the nickel chromites.

Least squares fits through the plots of Fig. 55 resulted in the following Arrhenius equations for cobalt chromite formation and interface migration:

CoO (high purity)

$$k_p = 1.03 \times 10^{-4} \exp(-42.6 \times 10^3/RT)$$

CoO-1MnO

$$k_p = 2.96 \times 10^{-4} \exp(-49.8 \times 10^3/RT)$$

CoO-1SiO_2

$$k_p = 4.87 \exp(-71.5 \times 10^3/RT)$$

Interface migration, high-purity single crystals

$$k_p = 4.59 \exp(-19.3 \times 10^3/RT)$$

V DISCUSSION

A. Nickel Chromite Formation

A number of effects have been observed in this work that have not been reported previously, and that help describe the mechanism of nickel-chromite formation. These effects are: marker behavior, spinel dissolution and precipitation in nickel oxide, and spinel growth as a function of location within the specimen. The explanations for these effects and their influence on the mechanisms and kinetics of nickel chromite will be discussed.

1. Marker Behavior

In the present experiments the platinum or iridium markers were always found at the nickel oxide/spinel interface or buried within the nickel oxide. This was true for dense polycrystalline or single crystalline or single crystalline specimens. The only exception to this behavior was the location of platinum marker within the spinel layer when the spinel was grown from chromium-saturated nickel oxide. The observed effects are explained as follows.

Thick platinum markers ($\simeq$ 6 μm) were generally found at the nickel oxide/spinel interface. After extended reaction times, defects would appear in the marker that would lead to the formation of chromium-rich nickel oxide intrusions into the chromium oxide (Figs. 17-19). Similarly, the nickel oxide/spinel interface always moved toward the chromium oxide half of the diffusion couple with respect to the thick marker (Fig. 20). Thin markers ($\simeq$ 2 μm) in the initial forms of foils or powder were observed to remain in alignment after the reaction. The thin foils agglomerated to form discrete particles, but did not become misaligned during the reactions (Figs. 14, 15). Since all the discrete particles do not form from the thin markers at the

same time, their alignment indicates that there is little (if any) marker motion, and that the nickel oxide/nickel chromite interface moves with respect to the markers.

In these studies there was no evidence of marker "attack" or dissolution (Fig. 17) even after prolonged exposures at high temperatures (150 hours at 1520°C). Oxidation or loss of markers was observed when the markers were exposed to air (i.e., were sticking out from the interfaces of stacked pellets). These observations, therefore, suggest that the marker attack reported by Lindner and Akerstrom[9] and by Schmalzried[21] was the result of oxidation and volatilization of the platinum markers by air through their porous specimens. When air is excluded by dense specimens, marker attack or dissolution will not occur.

2. Nickel Chromite Precipitation

Throughout these experiments there was evidence of second-phase precipitation in nickel oxide after spinel reactions. This precipitation occurred in high-purity, commercial-purity, or manganese-doped nickel oxide (Figs. 4, 13, 14, 15, 16, 21) and in dense polycrystalline or single crystalline specimens (Figs. 22, 24). These precipitates were found to be nickel chromite by a combination of X-ray diffraction (Fig. 16) and electron microprobe (Figs. 24 and 25) techniques. Further, the same Widmanstatten precipitate structure could be duplicated by reacting a powder mixture of NiO-13 wt % Cr_2O_3 at 1400°C and cooling to room temperature (Fig. 29). These data, therefore, show that there is extensive solubility of chromium (of the order of 10%) in nickel oxide at temperatures greater than 1200°C, and explain the non-uniform shrinkage of chromium oxide pellets at the reaction interface (Fig. 8a).

This solubility has not been reported previously. However, analogous solubility and precipitation of $FeCr_2O_4$ in FeO (in oxide scales formed on iron chromium alloys) has been reported by Moreau.[37]

The precipitation of nickel chromite therefore results from the dissolution of Cr^{3+} from the nickel chromite reaction layer and diffusion into the nickel oxide. As can be seen in Figs. 23 and 25, the diffusion of Cr^{3+} in nickel oxide is fast: at 1410°C the chemical diffusion coefficient for Cr^{3+} is of the order of 10^{-9} cm^2/sec, which is similar to the self-diffusion coefficient of 3×10^{-9} cm^2/sec for Ni^{2+} in nickel oxide.[3,35,36] It should be noted that diffusivity of Cr^{3+} in nickel oxide is of the same order of magnitude as in nickel chromite.[9,10,12] Consequently the growth of the spinel layer will be strongly influenced by chromium dissolution in nickel oxide. This will be discussed in more detail.

3. Spinel Growth Mechanisms and Kinetics

As was shown in section IV (Fig. 11), the thickness of the nickel chromite reaction product is highly dependent on local environmental and structural variables in the reacting pellets. At pellet corners or cracks (which are exposed to air) the spinel layer is very thick (Figs. 12, 21, 24), while at dense, crack-free regions, the spinel is very thin (Figs. 12, 13, 21, 22). At dense, crack-free locations that contain thick platinum markers, the spinel layer is intermediate in thickness (Fig. 13a). The latter pheonomenon has been explained on the basis of inhibited dissolution of the nickel chromite layer by nickel oxide (see Section IV-B-4). The nickel chromite layer in Fig. 13a therefore represents spinel formation by Ni^{2+} transport through the platinum marker and through the spinel layer and reaction at the chromium oxide interface. This transport may be balanced by countercurrent diffusion of Cr^{3+} through the spinel and dissolution in nickel oxide

The mechanism of nickel chromite formation at dense, crack-free regions of the specimen can be determined from the electron microprobe data of Fig. 23. As is shown in Fig. 22, the spinel

layer thickness formed between single crystal nickel oxide and chromium oxide is approximately 6 μ. In addition, the marker was buried in the nickel oxide single crystal at a distance of 56 μ from the nickel oxide/nickel chromite interface. By measuring the area under Cr Kα penetration curve in the nickel oxide, and dividing by the Cr Kα intensity for nickel chromite (determined by comparison with Fig. 32), a dissolved spinel layer thickness of 75 μ was determined. From these measurements (Fig. 56), the ratio of the spinel thickness on the nickel oxide side of the markers to the spinel thickness on the chromium oxide side was determined to be 1:3.06, in excellent agreement with the Wagner mechanism of countercurrent diffusion of Cr^{3+} and Ni^{2+}. This result also supports other data (described previously) that the markers remain stationary, and that the nickel oxide/nickel chromite reaction interface moves toward the chromium oxide half of the diffusion couple.

The validity of the Wagner mechanism in nickel chromite formation was also confirmed by the experiment with the chromium-saturated nickel oxide (see section IV-B-6). As was shown in Fig. 30, the marker position was approximately centered in the nickel chromite layer when the chromium-saturated nickel oxide was reacted with dense chromium oxide. The exact position of the marker (1/2 rather than 1/4 the distance from the nickel oxide to the chromium oxide) can be explained on the basis of the porosity of the nickel oxide. Vaporization of chromium oxide through pores in the nickel oxide could have grown some spinel from both sides of the marker, until the spinel layer became dense enough to prevent further vapor transport. This experiment shows that the reaction mechanism can be determined by markers if solubility problems are compensated.

If these experiments did indeed prove that the Wagner mechanism was operative, the kinetic data determined in this study (Fig. 35 and 36) should compare well with the theoretical treatments and other measurements. The rate data determined in this study and the rate

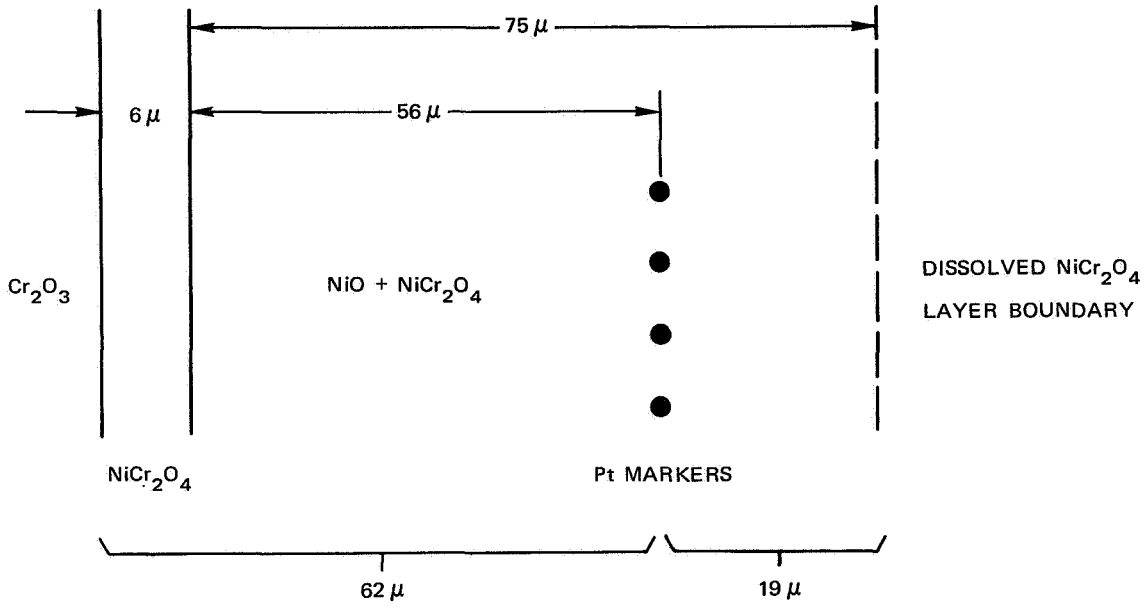

FIGURE 56 CONFIRMATION OF WAGNER MECHANISMS IN FORMATION OF NICKEL CHROMITE FROM SINGLE CRYSTAL NICKEL OXIDE AND CHROMIUM OXIDE

data of Sockel[26] and Lindner and Akerstrom[9] are compared in Fig. 57. It is apparent that their data are in excellent agreement with the least squares fit of the data in this study. However, their data agree with surface spinel growth rates (position A, Fig. 11) and not the internal spinel growth rates. This agreement is further proof of the porosity of their specimens, and the influence of vapor-phase transport on their measurements.

Comparisons of the measured spinel formation rates with the Wagner-Schmalzried theory were made by using equation 39. Data used for this comparison (and for subsequent comparison of cobalt chromite formation with theory) are shown in Table 11. The free energies of formation were taken from Tretjakow and Schmalzried,[23] and values of Z_A and N_A were chosen on the basis that the diffusion rates of Ni^{2+} and Co^{2+} control spinel formation in their respective spinels. This is basically correct, because the diffusivities of Ni^{2+} and Co^{2+} are less than that of Cr^{3+} over the temperature range of interest. Values of $\tilde{c}_A$ (the equivalent concentration) were calculated by multiplying the molar concentration (in gram moles per cubic centimeter) of Ni^{2+} or Co^{2+} by 2. Equivalent volumes were calculated by dividing the molar volume of each spinel by 2. This equivalent volume is equal to the volume of spinel that would form when 1 gm equivalent of the ion (which controls the reaction rate) is transported through the reaction layer. Consequently, when 1 gm mole of Ni^{2+} (2 gm equivalents reacts, it forms 1 molar volume (2 equivalent volumes) of spinel. This discussion may belabor the definitions, but it is necessary since there is confusion in the calculation and use of these terms.[25] The preferred values for the diffusivities of Ni^{2+} in nickel chromite are those of Lindner and Akerstrom;[11] however, the same authors have also reported diffusion coefficients 1 order of magnitude smaller.[9,12] As would be expected, the values of the diffusion coefficients totally control the values of k_p. For example, at

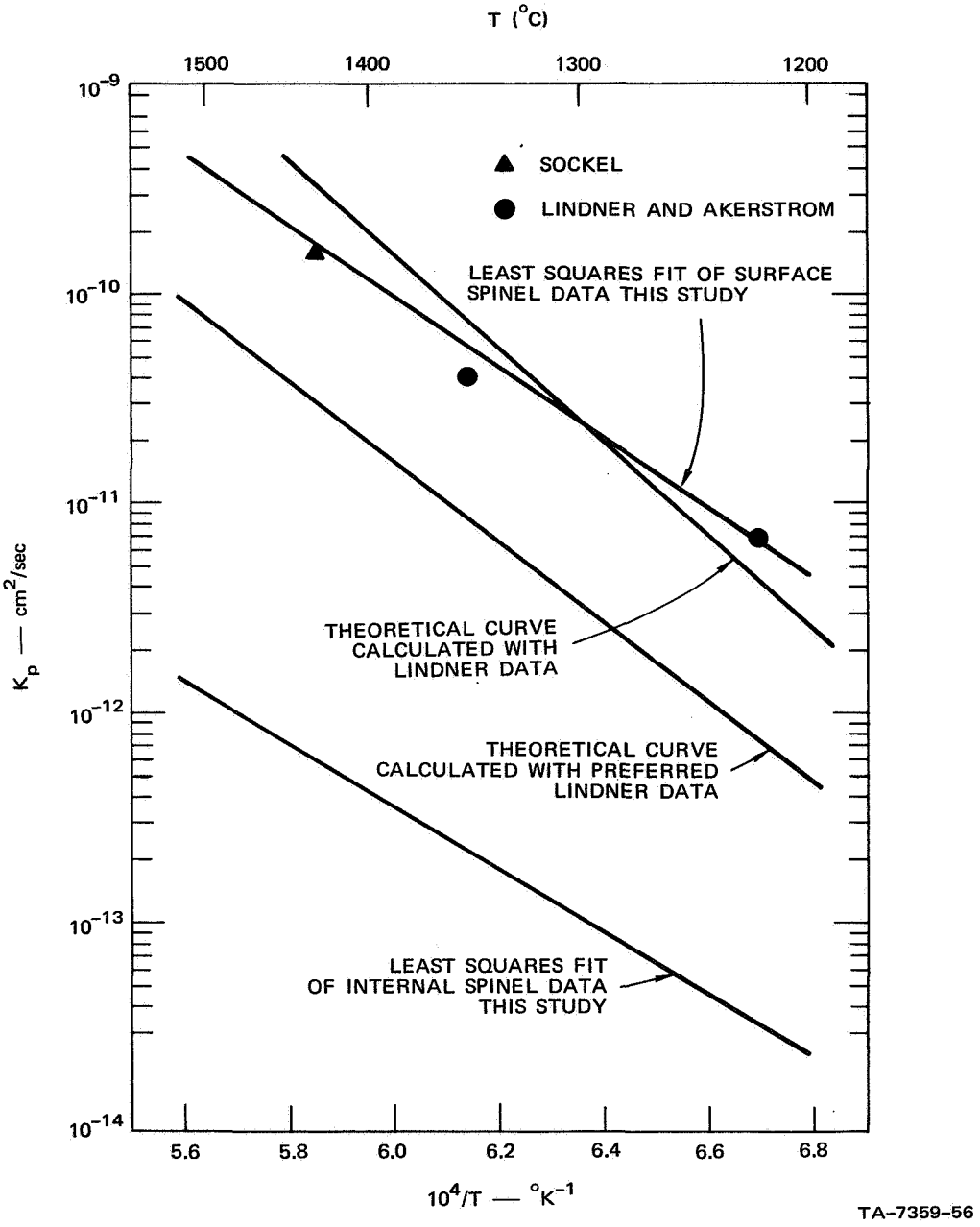

FIGURE 57 COMPARISON OF MEASURED AND THEORETICAL[9, 11, 12, 26] PARABOLIC REACTION RATE CONSTANTS FOR NICKEL CHROMITE

TABLE 11

DATA USED FOR CALCULATING THEORETICAL SPINEL FORMATION RATES

Spinel	ΔG^{o}(1000-1500°K), Kcal/mole	N_A	Z_A	ρ, gm/cm/^{3}	$\tilde{C}_A$, equiv/cm^3	$\tilde{V}$, cm^3/equiv
$NiCr_2O_4$	$-12.93 + 5.17 \times 10^{-3}T$	4/5	2	5.16	4.5×10^{-2}	22
$CoCr_2O_4$	$-19.36 + 5.77 \times 10^{-3}T$	4/5	2	5.14	4.5×10^{-2}	22

($T \simeq 1400^{o}C$) the parabolic rates constant equals 1.2 D_{Ni}. At lower temperatures ($1200^{o}C$), k_p equals 0.45 D_{Ni}. The theoretical values for the parabolic reaction rates using both sets of Lindner diffusion data are also shown in Fig. 57. The theoretical rates determined by using one set of data[9,12] from Table 2 compare reasonably well with the data obtained in this study and by others.[9,26] The theoretical curve determined by using later data (therefore listed as preferred data in Table 2) is lower than the experimental curve by a factor of 7. Although Lindner reported this earlier set of data several times,[9,12,40] it is likely that the more reliable Ni^{2+} diffusion data for nickel chromite are the later data of Lindner and Akerstrom.[11]

Consequently, the apparent agreement between the experimental and theoretical nickel chromite formation rates are fortuitous. This statement is supported by the following facts. The theory was developed to apply to the formation of dense, defect-free reaction product layers, while the experimental measurements were made with porous specimens or dense specimens whose surfaces were exposed to air (as in this study). The formation of these layers was therefore influenced by vapor transport through pores in the starting oxides. In addition, the experimental rates for surface spinel formation are significantly less than they should be, because of chromium dissolution in the nickel oxide. If chromium dissolution is prevented by doping the nickel oxide with chromium (as shown in Fig. 35), the spinel layer is 5 times thicker than the normal experimental rate for surface spinel formation. Consequently, the true surface reaction rates should be (and are) significantly faster than the measured rates. Therefore, the theory, which does not account for vapor transport through pores and dissolution of one component of the spinel by the other reactant, should not agree with the measured rates in which these effects prevail. If such agreement is found, it is fortuitous and misleading.

This same reasoning explains the very slow formation rates of the internal spinel observed in this study. As can be seen in Fig. 57, even the lower of the two theoretically determined curves is about two orders of magnitude greater than the curve for internal spinel formation. This means that the growth of the internal spinel layer is controlled by a mechanism other than diffusion across the spinel layer. This mechanism is probably countercurrent diffusion of Ni^{2+} and Cr^{3+} in the nickel oxide.

However, since the internal spinel layers only form in dense, crack-free regions of the specimen, their rates of growth should compare well with the correct theoretical rates. This statement only applies if the chromium dissolution in the specimen is accounted for in the calculation of the rate constant. For example, in Fig. 22 it was shown that the apparent spinel layer formed between single crystals of nickel oxide and chromium oxide was only 6 μ thick. However, microprobe traverses showed that the equivalent of 75 μ of spinel had dissolved in the nickel oxide crystal (Fig. 56). Consequently, the true rate of spinel formation should be calculated on the basis of a total spinel thickness of 81 μ. If this is done, the parabolic reaction rate constant is increased from 3.5×10^{-13} to 4.3×10^{-11} cm^2/sec, and is in reasonable agreement with the theoretical rate calculated from the preferred diffusion data.

These arguments form the basis for the following model of nickel chromite spinel formation. The model is simple, and is supported by the experimental data.

Internal, or solid-state, nickel chromite formation occurs by the countercurrent diffusion of Ni^{2+} and Cr^{3+} through the spinel, and more importantly, through the nickel oxide. The rate of spinel growth is controlled by the rate of chromium dissolution and diffusion in the nickel oxide. This model explains (a) spinel precipitation in NiO;

(b) marker effects, including intrusion formation at marker defects, and thick spinel formation at thick markers; (c) internal spinel thickness; and (d) the motion of the spinel layer with respect to the markers. With respect to the spinel motion, it should be emphasized that the identical activation energies for interface migration and internal spinel growth indicate that both processes are controlled by the same mechanism, which is Cr^{3+} and Ni^{2+} diffusion in nickel oxide.

Surface spinel formation also occurs by a modified Wagner mechanism in which spinel dissolution is operative. The high growth rates, however, suggest that another process, such as rapid transport of Cr^{3+} through the spinel layer and oxygen transport through the gas phase, could also be operative. This type of effect, when combined with the Wagner mechanism, will explain (a) thick spinel formation at specimen surfaces or within porous specimens, (b) thick spinel formation at cracks in the chromium oxide, and (c) the location of the platinum marker halfway in the spinel layer after the reaction of chromium-saturated nickel oxide with chromium oxide (Fig. 30). This mechanism may also partially explain the nonplanar diffusion interfaces at the spinel/chromium oxide boundaries. In this case, accelerated formation of spinel at chromium oxide grain boundaries may be favored by the higher diffusivities of O^{2-} at these sites.

4. Impurity Effects

Only qualitative statements will be made concerning the influence of impurities on the mechanism of spinel formation. There are two reasons for this. First, this is the first experimental study in which these effects have been considered. Second, the systems studied are more complex than normal spinels with respect to phase structure, defect structure, and thermodynamic definition.[18] Consequently at this stage of understanding, only qualitative discussion is justified.

As Fig. 35 shows the addition of 1 mole % manganese oxide to nickel oxide did not significantly affect the rate of formation of nickel chromite. This conclusion must be qualified, however, by the fact that experimental scatter would obscure small differences in parabolic rate constants. Although no effects were observed in the rate constants, significant manganese enrichment in the spinel was observed (Fig. 32). The concentration ratio (by weight) of manganese in the chromite to manganese in the nickel oxide was $\simeq$ 3.5:1. That is, the weight percentage of manganese oxide in nickel chromite was $\sim$ 3.5 times the weight percentage of manganese oxide in the starting nickel oxide. This higher concentration (by weight) is equivalent to a molar concentration of $\sim$ 1 mole % manganese oxide per mole of nickel chromite. It is concluded that manganese diffusion occurred from the nickel oxide into the nickel chromite sufficient to enrich the spinel to the level of 1 mole % manganese oxide. Since the activity of manganese oxide in nickel oxide and nickel chromite at the nickel oxide/nickel chromite interface must be the same, and since the mole fractions of manganese oxide in both phases are the same, the activity coefficient of manganese oxide in nickel oxide must be the same as in nickel chromite.

A qualitative explanation for the enrichment of manganese in the spinel can be based on the poly-valent characteristics of the ions. Manganese can esist either as $MnO(Mn^{2+})$ or $Mn_2O_3(Mn^{3+})$ and can form its own spinel Mn_3O_4 in which it exists in two valence states.[41,42] Consequently, the manganese ions can comfortably fit in both octahedral and tetrahedral sites in the spinel lattice. Therefore, the reaction of 1 mole of nickel oxide to form 1 mole of nickel chromite produces three times the initial number of sites in which the manganese ion can fit. The observed manganese enrichment can thus be explained by the filling of these new sites.

The influence of silicon on the mechanism of nickel chromite formation was difficult to assess. The only statements that can be made regarding these experiments are: (a) the reaction interface consisted of two phases, chromium oxide and nickel chromite; (b) there was no evidence of nickel orthosilicate in this layer; and (c) if the spinel layer thickness was corrected for chromium oxide content, the parabolic reaction rate constant would be essentially the same as for spinel formation from pure or manganese-doped nickel oxide.

B. Cobalt Chromite Formation

A number of effects were observed in the formation of cobalt chromite which have not been reported previously. Many of these effects (including marker behavior and spinel dissolution) were the same as those observed in nickel chromite formation, while other effects (spinel growth as a function of location in the specimen and influence of impurities) were significantly different.

1. Marker Behavior

In these studies, platinum markers were always buried in the cobalt oxide (Figs. 46,47) or at the cobalt oxide/cobalt chromite reaction interface (Fig. 48) after reaction. This was true for the reaction of 92% dense (polycrystaline) cobalt oxide and 100% dense (single crystalline) cobalt oxide with 100% dense (polycrystalline) chromium oxide. Further, the markers remained aligned during the spinel reaction, and were not attacked (Figs. 46, 47) or dissolved as reported earlier.[21]

The cobalt chromite dissolution and cobalt oxide intrusion formation at marker defects clearly explains the formation of nonplanar cobalt oxide/cobalt chromite interfaces at marker locations, and shows that the markers remain stationary while the interface moves toward the chromium oxide half of the diffusion couple.

2. Cobalt Chromite Precipitation

The marker studies proved that chromium dissolved in the cobalt oxide, while a combination of X-ray diffraction, electron microprobe, and microscopy techniques (Figs. 41, 44-47) proved that this dissolved chromium precipitated as cobalt chromite in the cobalt oxide on cooling. These data showed that there is solid solubility of Cr^{3+} in cobalt oxide, although it is not as extensive as the chromium solubility in nickel oxide: at temperatures of 1300°C, it is of the order of 5 wt % chromium oxide. This solubility also explains the non-uniform shrinkage of the chromium oxide at the reaction interface Figs. 37a, 38).

3. Spinel Growth Mechanisms and Kinetics

The thickness of the cobalt chromite reaction layer was not dependent on the local environmental and structural features in the reactions zone (Fig. 38). The thickness of the spinel layer at the center of the pellets and at the pellet surfaces was constant. This could be interpreted to mean that vapor transport effects influenced the reaction at the specimen surface and inside the specimen. However, the very good agreement between the parabolic reaction rate constant for polycrystalline and single crystalline specimens (Fig. 55) suggests that this interpretation is not correct. Further, the fully dense structure in the two-phase cobalt chromite + chromium oxide part of Fig. 40* conclusively proves that vapor transport effects are not necessary for rapid spinel formation, and emphasizes the need for a solid-state reaction mechanism.

The true marker position for cobalt oxide (single crystal)/chromium oxide experiments was determined by measuring the amounts of

---

* Structure of starting chromium oxide is shown in Fig. 3.

dissolved spinel in the cobalt oxide (Fig. 44). This mass balance revealed that the marker would be at the cobalt oxide/cobalt chromite reaction interface even if spinel dissolution was accounted for. The only mechanism that can explain this marker location (in the absence of vapor transport effects) is parallel diffusion of Co^{2+} and O^{2-} through the spinel layer. It should be noted that the limited spinel dissolution is confirmed by the (order of magnitude) slower interface migration rates as compared to the spinel formation rates shown in Fig. 55. This mechanism, while not generally propular, is consistent with, and explains the following experimental observations:

(a) Deep intergranular cobalt chromite formation along chromium grain boundaries.

(b) Dense, pore-free, two-phase (chromium oxide + cobalt chromite) reaction layers (Fig 40); if parallel diffusion of Cr^{3+} and O^{2-} occurred, the chromium oxide islands would develop porosity.

(c) Marker positions at the cobalt oxide/cobalt chromite interface reported in this dissertation and by others.[21]

(d) Formation of a polycrystalline spinel layer of grain size equal to the cobalt oxide grain size (Fig. 39).

(e) Formation of a polycrystalline spinel layer when single crystal cobalt oxide is reacted with polycrystalline chromium oxide.[26]

The reaction mechanisms that explains most, if not all, observations for cobalt chromite formation is the parallel diffusion of Co^{2+} and O^{2-} through the spinel layer. Countercurrent diffusion of Co^{2+} and electron holes through the spinel layer and oxygen transport through the gas phase (as concluded by Schmalzried[21] and Sockel[26]) will not explain observed effects. Countercurrent diffusion of Cr^{3+} and Co^{2+} is not consistent with the marker measurements in which spinel dissolution effects have been accounted for.

The data obtained in this study are compared with those determined by Schmalzried[21] and with theoretical rates in Fig. 58. There is poor agreement between the data measured in this study and the data of Schmalzried. The present data were determined by reacting 92 to 100% dense polycrystal and single crystal specimens over a wide temperature range (1287-1527°C), while Schmalzried's data were obtained from porous* specimens reacted over a shorter (1367-1500°C) temperature range. Theoretical rates were determined by assuming countercurrent diffusion of Co^{2+} and electron holes through the reaction layer and oxygen transport through the vapor phase. Reasonable agreement exists between the present data and theoretical rates determined from Sun's[8] diffusion data. Not surprisingly, reasonable agreement exists between Schmalzried's[21] experimental data and the theoretical rates determined from Morkel and Schmalzried's[4] diffusion data.

The data presented here cannot be explained on the basis of solid-state countercurrent diffusion of Co^{2+} ions and electron holes and oxygen vapor transport. Consequently, the agreement with the theoretical rate obtained by using Sun's diffusion data is not meaningful. For a good comparison of the proposed mechanism with theory, it is necessary to know the diffusion rates of oxygen in cobalt chromite. These rates have not been measured, but rates of oxygen diffusion through nickel chromite have been measured.[43] If these rates of oxygen diffusion in nickel chromite are assumed to be valid for cobalt chromite, the theoretical rate constants are in good agreement (within a factor of 4) with the experimental rate constants measured in this study. It is apparent from these studies, and the studies on nickel chromite formation, that any set of experimental rate constants can

---

* Specimen densities were not reported. Estimated densities based on Schmalzried's photomicrographs[21] are ~ 80% of theoretical values.

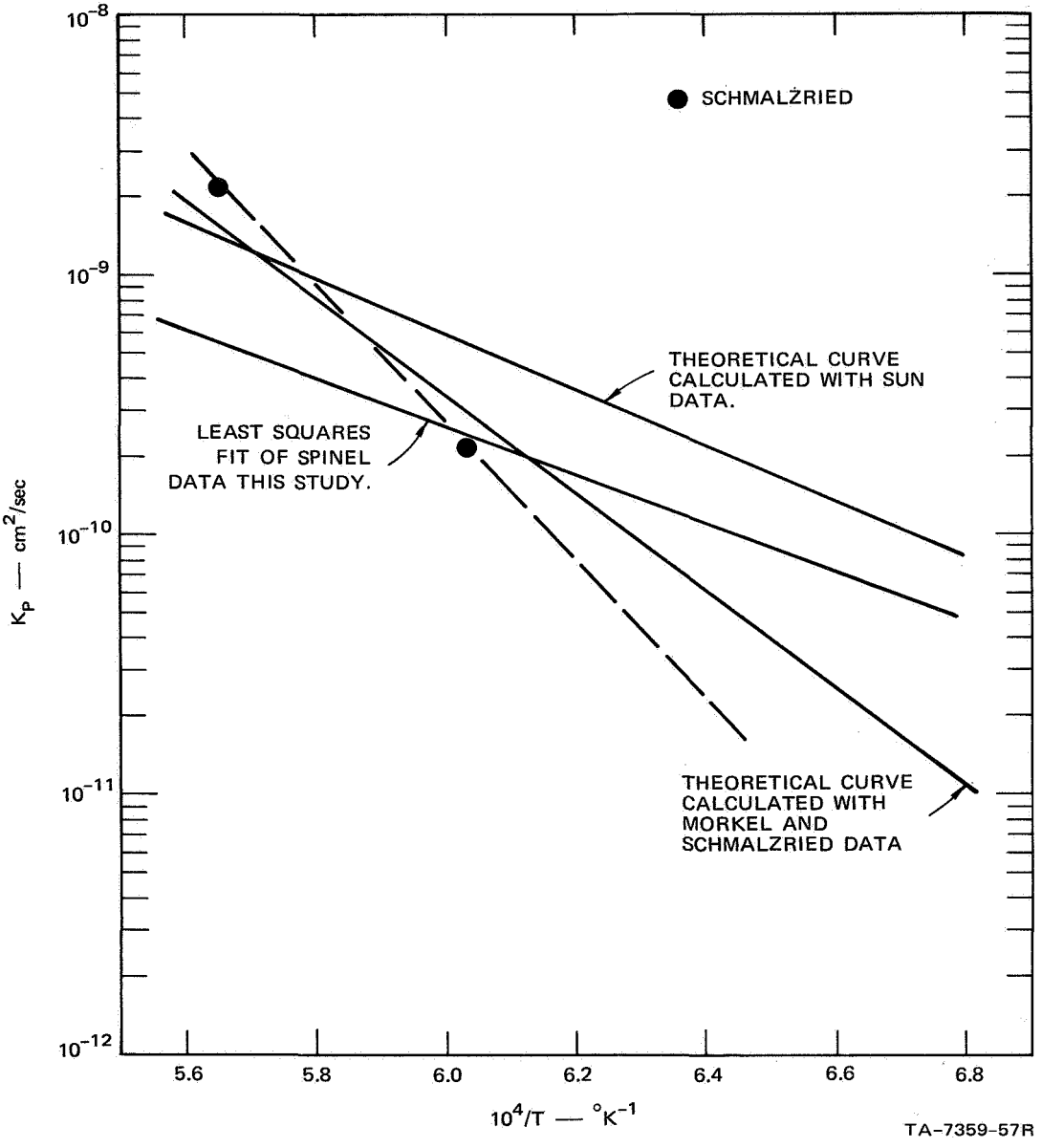

FIGURE 58 COMPARISON OF MEASURED AND THEORETICAL[8, 10, 21] PARABOLIC REACTION RATE CONSTANTS FOR COBALT CHROMITE

be found to agree with theoretical rate constants by the proper choice of available diffusion data. This problem simply emphasizes the importance of other techniques in the identification of reaction mechanisms.

4. Impurity Effects

Measurable impurity effects were observed in the formation of cobalt chromites from manganese-doped and silicon-doped cobalt oxides. Manganese doping reduced the chromite formation by factors of 2 to 4, while silicon doping increased the chromite formation rates by factors of 3 to 13 (Fig. 55).

Electron microprobe data (Figs. 49, 50b) show that there was some manganese in the cobalt chromite spinel, but that large quantities of manganese were associated with cobalt chromite precipitates in the cobalt oxide. By comparing the intensity ratios for Co $K\alpha$ and Mn $K\alpha$ in the cobalt oxide and in the spinel, one can conclude that there is little or no enrichment or depletion of manganese in either phase during spinel formation. For example, the manganese to cobalt intensity ratio in the cobalt oxide (taking an average value of I_{MnO}) is approximately 0.014, while the same ratio in the spinel is 0.016. This result qualitatively shows that manganese is incorporated into the spinel in direct proportion to the amount present in the cobalt oxide. This result contrasts strongly with the observed manganese enrichment in nickel chromite formation. The observed uniform incorporation of manganese into the cobalt chromite spinel can be explained on the basis of similar properties of cobalt and manganese oxides. Both form monoxide and spinel (AO and A_3O_4) structures in which the cations may be doubly or triply ionized. Consequently there should be little or no preferential partitioning of either cation to octahedral or tetrahedral sites in the spinel.

Several reasons could be given for the observed decrease in spinel formation rates with manganese-doped cobalt oxide. These explanations could include higher chromium dissolution rates in the manganese-doped cobalt oxide, or lower cobalt diffusion rates in the spinel. Either of these effects would reduce the net spinel thickness after a given reaction time and thus decrease the rate constant. The correct explanation of the effect, however, will require much more study.

The presence of 1 mole % SiO_2 (chiefly as Co_2SiO_4) in cobalt oxide greatly increased the rates of cobalt chromite formation. This effect occurred by the formation of spinel crystals (Fig. 52) in a cobalt orthosilicate matrix. There was no evidence of silicon or cobalt penetration into the chromium oxide (Fig. 53). Since spinel crystals were nucleated and grew from both cobalt oxide and chromium oxide sides of the spinel layer, and since there was no evidence of cobalt chromite penetration into the chromium oxide (Figs. 51 and 53), it is likely that the mechanism of spinel formation was countercurrent diffusion of Co^{2+} and Cr^{3+} through the reaction layer. This change in mechanism would account for the observed rate increases, since the rate would be controlled by the diffusion of the slower of the two cations. In addition, it is evident that the mechanism must occur by rapid transport of both cations through the continuous cobalt orthosilicate phase. Since this phase forms a eutectic with cobalt oxide at 1377°C,[44] the transport through the liquid phase at higher temperatures should produce a change of slope in Fig. 55. It is probable that the increased rate of cobalt chromite formation from silicon-doped cobalt oxides can be explained by rapid countercurrent diffusion of Co^{2+} and Co^{3+} through the orthosilicate phase.

VI CONCLUSIONS

There are a number of general conclusions from this work which have application to previous and future spinel studies. These conclusions are associated with the three major experimental observations of this study: density effects, spinel dissolution effects, and impurity effects. First, and perhaps most important, it has been shown that experimental results obtained from the reactions of high-density oxides are significantly different from those obtained from the reactions of porous oxides. Spinel formation rates in dense oxides can be orders of magnitude slower than rates in porous oxides. Mechanisms of spinel formation in porous oxides can be affected, or controlled, by vapor-phase transport phenomena, while reaction mechanisms in dense oxides cannot. Simple marker experiments can be interpreted when dense oxides are used, whereas these markers are often destroyed (by oxidation) when porous oxides are used. The present study therefore casts serious doubts on the significance of most previous experimental studies of spinel formation in which porous oxides were used. Correct definitions of the mechanisms of spinel formation on the basis of studies utilizing porous oxides are an indication of theoretical insight rather than experimental verification.

Dissolution effects, of the spinel in the reactants or the reactants in the spinel, must be accounted for in future studies. As has been shown in this work, such effects can control both the mechanism and kinetics of spinel formation. It is recognized that dissolution effects would be accounted for if observed. However, the observations of these effects requires the use of dense starting oxides and careful specimen preparation and examination.

Impurities can produce measurable changes in the rates of spinel formation. These changes can occur with or without the formation of

new phases. Since measurable effects can be produced by impurity concentrations of the order of 1 mole %, it is important that purity levels of reactants in future studies be documented. In addition, it is apparent that impurity additions to oxides or metals may be useful in accelerating or decelerating the rates of spinel formation and thus partially controlling oxidation behavior.

Another general conclusion from this work is that reaction mechanisms must be determined by direct experimental techniques. Determination of reaction mechanisms by comparison of experimental and theoretical reaction-rate constants is totally dependent on measured rates of diffusion of cations through their respective spinels. There is sufficient variability in the diffusion data for these systems that nearly any experimental measurement will fit within an order of magnitude of a theoretical value. Any true test of the validity of a theoretically determined rate constant must be based on precise diffusion data through fully dense polycrystalline or single crystalline spinels, and theoretical data must be compared with experimental kinetic data determined from similar oxides.

A. Nickel Chromite Formation

1. The mechanisms of nickel chromite formation from pure, dense, crack-free reactants is countercurrent diffusion of Ni^{2+} and Cr^{3+} through the spinel layer.

2. The mechanism of nickel chromite formation from porous reactants or at the surfaces of dense reactants is a combination of vapor phase transport of volatile oxides and oxygen, and solid state diffusion of Cr^{3+} and Ni^{2+} through the spinel layer.

3. The rate of nickel chromite formation in dense, crack-free oxides is 2 orders of magnitude less than the rates of formation at surfaces, and is controlled by the rate of chromium dissolution in nickel oxide.

4. Dissolution of Cr^{3+} in nickel oxide occurs at high (> 1200°C) temperatures. The solubility of chromium oxide in nickel oxide is of the order of 10 wt %. On cooling to room temperature, the Cr^{3+} precipitates as nickel chromite in the nickel oxide.

5. After nickel chromite formation, thin inert markers are found to be buried in the nickel oxide as a result of chromium dissolution and countercurrent diffusion of Ni^{2+} and Cr^{3+} in nickel oxide. If dissolution effects are accounted for, the marker will be found in the spinel layer, and confirm the Wagner reaction mechanism for this system.

6. Spinel solubilities should be accounted for in any mechanistic study. Other systems in which such effects will be found can be determined by examination of available phase diagrams. Particular spinels which will exibit this effect include magnesium chromite[45] and magnesium aluminate.[46,47]

7. Measured reaction rate constants agree well with theoretical values determined from the Wagner-Schmalzried theory and available thermodynamic and diffusion data. However, because of variability in the diffusion data, this agreement should be accepted with caution.

8. Additions of manganese or silicon impurities (at the level of 1 mole %) to nickel oxide will not affect the rate of nickel chromite growth. However, manganese enrichment of the chromite layer will occur when the spinel is formed from manganese-doped oxides. A two-phase nickel chromite + chromium oxide layer will form from the reaction of silicon-doped nickel oxide.

B. Cobalt Chromite Formation

1. The mechanism of cobalt chromite formation in pure, dense crack-free oxides or at oxide surfaces is unidirectional diffusion of Co^{2+} and O^{2-} through the spinel layer.

2. Dissolution of Cr^{3+} in cobalt oxide occurs at high temperatures ($> 1200^{o}C$). The solubility of chromium oxide in cobalt oxide at these temperatures is of the order of 5 wt %. On cooling to room temperature, the dissolved Cr^{3+} precipitates as cobalt chromite in the cobalt oxide.

3. After cobalt chromite formation, thin inert markers are found buried in the cobalt oxide as the result of chromium dissolution and countercurrent Co^{2+} and Cr^{3+} diffusion in the cobalt oxide. If dissolution effects are accounted for, the marker will be found at the cobalt oxide/cobalt chromite interface, and will confirm the reaction mechanism (unidirectional diffusion of Co^{2+} and O^{2-} through the spinel).

4. Formation of cobalt chromite from cobalt oxide doped with 1 mole % manganese oxide results in a slower spinel growth rate. The concentration (by weight) of manganese in the monoxide and the spinel remains constant during this reaction.

5. Formation of cobalt chromite from cobalt oxide doped with 1 mole % silicon oxide results in very fast spinel growth rates. Growth occurs by countercurrent diffusion of Co^{2+} and Cr^{3+} through a continuous phase cobalt orthosilicate to form large spinel crystals.

REFERENCES

1. C. E. Birchenall, The Role of Spinel Oxide in the Oxidation of Iron and Its Alloys, Zeitschr. Elektrochem., 63, 790 (1959).

2. J. W. Hickman and E. A. Gulbransen, An Electron Diffraction Study of Oxide Films Formed on Nickel-Chromium Alloys, Trans. AIME, 180, 519 (1949).

3. D. L. Douglass, unpublished research.

4. F. C. Romeijn, Physical and Crystallographic Properties of Some Spinels, I, General Properties, Phillips Res. Rept., 8, 304 (1953).

5. L. V. Azaroff, Introduction to Solids, McGraw-Hill, New York (1960).

6. J. B. Goodenough, Direct Cation-Cation Interactions in Several Oxides, Phys. Rev., 117, 1442 (1960).

7. R. R Dilo, Cation Interdiffusion in the Chromia-Alumina System, Ph.D. Dissertation, Stanford University (1965).

8. R. Sun, Diffusion of Cobalt and Chromium in Chromite Spinel, J. Chem. Phys., 28, 290 (1958).

9. R. Lindner and A. Akerstrom, Self-Diffusion and Reaction in Oxide and Spinel Systems, Z. Phys. Chem. (N.F.), 6, 162 (1956).

10. A. Morkel and H. Schmalzried, Self-Diffusion and Defect Structure in Spinels, Z.Phys. Chem. (N.F.), 32, 76 (1962).

11. R. Lindner and A. Akerstrom, Diffusion of Ni-36 in Nickel Spinels, Z. Phys. Chem. (N.F.), 18, 303 (1958).

12. R. Lindner, Self-Diffusion in Oxide Systems, Naturforsch., 10a, 1027 (1955).

13. J. A. Hedvall, C. Brisi, and R. Lindner, Self-Diffusion in Monocalcium Ferrite, Arkiv. Kemi., 4, 377 (1952).

14. R. Lindner, D. Campbell, and A. Akerstrom, The Diffusion of Radioactive Zinc in $ZnOFe_2O_3$ (Spinel) and Zinc Oxide, Acta Chem. Scand., 6, 457 (1952).

15. R. Lindner, Diffusion of Radioactive Iron in Iron (III) Oxide and Zinc-Iron Spinel, Arkiv. Kemi., 4, 381 (1952).

16. N. S. Gorbunov and V. I. Izvekov, The Study of Diffusion in Metal Oxides with the Aid of Radioactive Isotopes, Uspekhi Fiz. Nauk, 72, 273 (1960).

17. H. Schmalzried and C. Wagner, Defect Structures in Ternary Ionic Crystals, Z. Phys. Chem. (N.F.), 31, 198 (1962).

18. H. Schmalzried, Point Defects in Ternary Ionic Crystals, Progr. Chem. Solid State, 2, 265 (1965).

19. F. A. Kroger and H. J. Vink, Relations between the Concentrations of Imperfections in Crystalline Solids, Solid State Physics, 3, 307, Academic Press (1963).

20. C. Wagner, On the Mechanism of Formation of Ionically Bonded Higher Order (Double Salts, Spinels, Silicates), Z. Phys. Chem., 34, 309 (1936).

21. H. Schmalzried, Reaction Mechanisms of Spinel Formation in the Solid State, Z. Phys. Chem. (N.F.), 33, 111 (1962).

22. H. Schmalzried, Solid State Reactions, Ber. Deut. Keram. Ges., 42, 11 (1965).

23. J. D. Tretjakow and H. Schmalzried, The Thermodynamics of Spinel Phases, Ber. Bunsenges. Phys. Chem., 69, 396 (1965).

24. B. Bengston and R. Jagitsch, Kinetic Studies on Formation of Spinel from Zinc Oxide and Alumina, Arkiv. Kemi, 24A, 1 (1947).

25. F. S. Pettit, E. H. Randklev, and E. J. Felton, Formation of $NiAl_2O_4$ by Solid State Reaction, J. Am. Ceram. Soc., 49, 199 (1966).

26. H. G. Sockel, Morphology and Kinetics of Spinel Formation, Thesis, University of Goettingen (1965).

27. R. E. Carter, Mechanism of Solid State Reaction between Magnesium Oxide and Aluminum Oxide and between Magnesium Oxide and Ferric Oxide, J. Am Ceram. Soc., 44, 116 (1961).

28. K. Hauffe and K. Pschera, On the Mechanism of Spinel Formation at Elevated Temperatures, Z. Anorg. Allg. Chem., 262, 147 (1950).

29. H. Schmalzried, Ionic and Electronic Defect Structure in $CoCr_2O_4$ and $CoAl_2O_4$, Zeitschr. Elektrochem., 67, 93 (1963).

30. Y. Iida, Sintering of High-Purity Nickel Oxide, J. Am. Ceram. Soc., 41, 397 (1958).

31. Y. Iida and S. Ozaki, Sintering of High-Purity Nickel Oxide, II, J. Am. Ceram. Soc., 42, 219 (1959).

32. R. M. Spriggs, L. A. Brissette, and T. Vasilos, Pressure Sintered Nickel Oxide, Am. Ceram. Soc. Bull., 43, 572 (1964).

33. R. A. Brown, Sintering in Very Pure Magnesium Oxide and Magnesium Oxide Containing Vanadium, Am. Ceram. Soc. Bull., 44 483 (1965).

34. R. A. Brown, Sintering in Calcium Oxide and Calcium Oxide Containing Strontium, Am. Ceram. Soc. Bull., 44, 693 (1965).

35. R. Dils, Modification of a Coslett-Nixon Microfocus X-ray Tube for Use as an X-Ray Microanalyzer, Rev. Sci. Instr., 32, 1044 (1961).

36. L. Thomassen, An X-ray Investigation of the System Cr_2O_3-NiO, J. Am. Chem. Soc., 62, 1134 (1940).

37. J. Moreau, Study of the High-Temperature Oxidation Mechanism of Binary Iron-Chromium Alloys, Compt. Rend., 236, 85 (1953).

38. R. Lindner and A. Akerstrom, Diffusion of Ni-63 in Nickel Oxide (NiO), Disc. Faraday Soc., 23, 133 (1957).

39. J. S. Choi and W. J. Moore, Diffusion of Nickel in Single Crystals of Nickel Oxide, J. Phys. Chem., 65, 1438 (1961).

40. R. Lindner, Formation of Spinels and Silicates during Solid State Reactions, Studies by the Radioactive Tracer Method, Zeitschr. Elektrochem., 59, 967 (1955).

41. R. S. Gurnick and W. M. Baldwin, Jr., The High-Temperature Oxidation of Manganese, Trans. ASM, 42, 308 (1950).

42. E. B. Evans, C. A. Phalnikar, and W. M. Baldwin, Jr., High Temperature Scaling of Nickel-Manganese Alloys, J. Electrochem. Soc., 103, 367 (1956).

43. W. D. Kingery, D. C. Hill, and R. P. Nelson, Oxygen Mobility in Polycrystalline $NiCr_2O_4$ and α Fe_2O_3, J. Am. Ceram. Soc., 43, 473 (1960).

44. P. Asanti and E. J. Kohlmeyer, On the Thermal Properties of Compounds of Cobalt with Oxygen and Sulfur, Z. Anorg. Chem. 265, 96 (1951).

45. A. M. Alper, R. N. McNally, R. C. Doman, and F. G. Keihn, Phase Equilibria in the System $MgO-MgCr_2O_4$, J. Am. Ceram. Soc., 47, 30 (1964).

46. A. M. Alper, R. N. McNally, P. G. Ribbe, and R. C. Doman, The System $MgO-MgAl_2O_4$, J. Am. Ceram. Soc., 45, 264 (1962).

47. D. M. Roy, R. Roy and E. F. Osborn, The System $MgO-Al_2O_3-SiO_2$ and Influence of Carbonate and Nitrate Ions on the Phase Equilibria, J. Am. Ceram. Soc., 36, 149 (1953).

APPENDIX I

SUMMARY OF EXPERIMENTAL DATA

Expt. No.	Reactants	Previous Bond	Reaction Temperature ^{o}C	Reaction Time sec	Reaction Layer	Layer Thickness cm	Rate Constant cm/sec
1	NiO (cp)/Cr_2O_3	none	1235	2.3×10^{5}	surface	1.58×10^{-3}	5.4×10^{-12}
2	NiO (cp)/Cr_2O_3	expt. 1	1430	2.3×10^{5}	surface	9.5×10^{-3}	1.7×10^{-10}
3	NiO (cp)/Cr_2O_3	none	1200	1.3×10^{6}	internal	2.1×10^{-4}	1.7×10^{-14}
4	NiO (cp)/Cr_2O_3	none	1475	3.2×10^{5}	surface	16.3×10^{-3}	4.2×10^{-10}
4	NiO (cp)/Cr_2O_3	none	1475	3.2×10^{5}	internal	5.9×10^{-4}	4.0×10^{-13}
4	NiO (cp)/Cr_2O_3	none	1475	3.2×10^{5}	interface displacement	11.4×10^{-3}	2.0×10^{-10}
5A	NiO (hp)/Cr_2O_3	none	1372	1.5×10^{5}	surface	4.9×10^{-3}	8.0×10^{-11}
5A	NiO (hp)/Cr_2O_3	none	1372	1.5×10^{5}	internal	2.5×10^{-4}	2.0×10^{-13}
5A	NiO (hp)/Cr_2O_3	none	1372	1.5×10^{5}	interface displacement	3.9×10^{-3}	5.0×10^{-11}
5B	NiO-1MnO/Cr_2O_3	none	1372	1.5×10^{5}	interface displacement	3.2×10^{-3}	3.5×10^{-11}
6	NiO (cp)/Cr_2O_3	none	1395	4.3×10^{5}	surface	9.9×10^{-3}	1.2×10^{-10}
6	NiO (cp)/Cr_2O_3	none	1395	4.3×10^{5}	internal	5.1×10^{-4}	3.1×10^{-13}
6	NiO (cp)/Cr_2O_3	none	1395	4.3×10^{5}	interface displacement	6.5×10^{-3}	5×10^{-11}
7A	NiO (hp)/Cr_2O_3	none	1200	1.8×10^{6}	surface	3.8×10^{-3}	4.05×10^{-12}
7A	NiO (hp)/Cr_2O_3	none	1200	1.8×10^{6}	internal	3.2×10^{-4}	2.9×10^{-14}

Expt. No.	Reactants	Previous Bond	Reaction Temperature °C	Reaction Time sec	Reaction Layer	Layer Thickness cm	Rate Constant cm/sec
7A	NiO (hp)/Cr_2O_3	none	1200	1.8×10^6	interface displacement	3.2×10^{-3}	2.8×10^{-12}
7B	NiO-1MnO/Cr_2O_3	none	1200	1.8×10^6	surface	4.2×10^{-3}	4.9×10^{-12}
7B	NiO-1MnO/Cr_2O_3	none	1200	1.8×10^6	interface displacement	2.6×10^{-3}	1.85×10^{-12}
8A	NiO-1MnO/Cr_2O_3	none	1400	6.98×10^5	surface	12.2×10^{-3}	1.06×10^{-10}
8A	NiO-1MnO/Cr_2O_3	none	1400	6.98×10^5	interface displacement	8.8×10^{-3}	5.5×10^{-11}
8B	NiO (hp)/Cr_2O_3	none	1400	6.98×10^5	surface	12.9×10^{-3}	1.2×10^{-10}
8B	NiO (hp)/Cr_2O_3	none	1400	6.98×10^5	interface displacement	8.4×10^{-3}	5.0×10^{-11}
9A	NiO-1MnO/Cr_2O_3	none	1520	5.48×10^5	surface	18.2×10^{-3}	3.0×10^{-10}
9A	NiO-1Mno/Cr_2O_3	none	1520	5.48×10^5	interface displacement	13.2×10^{-3}	1.6×10^{-10}
9B	NiO (hp)/Cr_2O_3	none	1520	5.48×10^5	surface	26.7×10^{-3}	6.5×10^{-10}
10A	NiO-1MnO/Cr_2O_3	none	1235	1.04×10^6	surface	4.98×10^{-3}	1.2×10^{-11}
10A	NiO-1MnO/Cr_2O_3	none	1235	1.04×10^6	internal	3.0×10^{-4}	4.3×10^{-14}
10B	NiO (hp)/Cr_2O_3	none	1235	1.04×10^6	surface	3.88×10^{-3}	7.3×10^{-12}
10B	NiO (hp)/Cr_2O_3	none	1235	1.04×10^6	internal	1.4×10^{-4}	2.8×10^{-14}
11A	NiO (hp)/Cr_2O_3	none	1200	7.6×10^5	interface displacement	3.24×10^{-3}	6.9×10^{-12}
11B	NiO-1MnO/Cr_2O_3	none	1200	7.6×10^{-5}	interface displacement	3.07×10^{-3}	6.2×10^{-12}

Expt. No.	Reactants	Previous Bond	Reaction Temperature ^{o}C	Reaction Time sec	Reaction Layer	Layer Thickness cm	Rate Constant cm/sec
12A	NiO (hp)/Cr_2O_3	none	1235	7.8×10^{5}	surface	3.82×10^{-3}	9.3×10^{-12}
12B	NiO-1MnO/Cr_2O_3	none	1235	7.8×10^{5}	surface	3.54×10^{-3}	8.0×10^{-12}
13A	NiO (hp)/Cr_2O_3	none	1450	7.03×10^{5}	internal	7×10^{-4}	3.5×10^{-13}
13B	NiO (hp)/Cr_2O_3	none	1450	7.03×10^{5}	interface displacement	9.51×10^{-3}	6.4×10^{-11}
13B	NiO-1SiO_2/Cr_2O_3	none	1450	7.03×10^{5}	internal	9.4×10^{-4}	6.3×10^{-13}
13A	NiO-1SiO_2/Cr_2O_3	none	1450	7.03×10^{5}	interface displacement	8.9×10^{-3}	5.6×10^{-11}
14	NiO (cp)/Cr_2O_3	expt. 3	1512	8.64×10^{4}	surface	8.7×10^{-3}	4.4×10^{-10}
14	NiO (cp)/Cr_2O_3	expt. 3	1512	8.64×10^{4}	internal	6.5×10^{-4}	2.2×10^{-12}
14	NiO (cp)/Cr_2O_3	expt. 3	1512	8.64×10^{4}	interface displacement	6.3×10^{-3}	1.3×10^{-10}
15	NiO-MnO/Cr_2O_3	none	1512	8.64×10^{4}	surface	6.6×10^{-3}	2.5×10^{-10}
15	NiO-MnO/Cr_2O_3	none	1512	8.64×10^{4}	internal	4.74×10^{-4}	1.3×10^{-12}
15	NiO-MnO/Cr_2O_3	none	1512	8.64×10^{4}	interface displacement	5.42×10^{-3}	1.7×10^{-10}
16A	NiO (cp)/Cr_2O_3 Single Crystal	none	1305	8.65×10^{5}	surface	5.95×10^{-3}	2.04×10^{-11}
16A	NiO (cp)/Cr_2O_3 Single Crystal	none	1305	8.65×10^{5}	internal	4.0×10^{-4}	9.3×10^{-14}
16A	NiO (cp)/Cr_2O_3 Single Crystal	none	1305	8.65×10^{5}	interface displacement	3.94×10^{-3}	8.9×10^{-12}

Expt. No.	Reactants	Previous Bond	Reaction Temperature °C	Reaction Time sec	Reaction Layer	Layer Thickness cm	Rate Constant cm/sec
16B	NiO (Single Crystal)/Cr_2O_3 (Single Crystal)	none	1305	8.65×10^5	surface	6.85×10^{-3}	2.7×10^{-11}
17A	NiO (Single Crystal)/Cr_2O_3	none	1410	7.55×10^5	surface	11.9×10^{-3}	9.4×10^{-11}
17A	NiO (Single Crystal)/Cr_2O_3	none	1410	7.55×10^5	internal	1.0×10^{-3}	6.5×10^{-13}
17A	NiO (Single Crystal)Cr_2O_3	none	1410	7.55×10^5	interface displacement	6.0×10^{-3}	2.4×10^{-11}
17B	NiO (Single Crystal)/Cr_2O_3 (Single Crystal)	none	1410	7.55×10^5	surface	9.6×10^{-3}	6.1×10^{-11}
17B	NiO (Single Crystal)/Cr_2O_3 (Single Crystal)	none	1410	7.55×10^5	internal	7.0×10^{-4}	3.3×10^{-13}
18	NiO-1MnO/Cr_2O_3	none	1250	1.7×10^6	internal	5.08×10^{-4}	7.6×10^{-14}
19	NiO-13Cr_2O_3/Cr_2O_3	none	1370	4.94×10^5	surface	2.2×10^{-2}	4.9×10^{-10}
Co-1	CoO(hp)/Cr_2O_3	none	1265	1.66×10^5	internal	5.82×10^{-3}	1.01×10^{-10}
Co-2	CoO-1MnO/Cr_2O_3	none	1265	8.64×10^5	internal	6.36×10^{-3}	2.34×10^{-11}
Co-3	CoO (hp)/Cr_2O_3	none	1265	6.01×10^5	internal	10.2×10^{-3}	8.65×10^{-11}
Co-4	CoO-1MnO/Cr_2O_3	Co-2	1445	8.72×10^5	internal	16.5×10^{-3}	1.33×10^{-10}
Co-5	CoO-1MnO/Cr_2O_3	none	1195	2.33×10^6	internal	6.8×10^{-3}	1.01×10^{-11}

Expt. No.	Reactants	Previous Bond	Reaction Temperature ^{o}C	Reaction Time sec	Reaction Layer	Layer Thickness cm	Rate Constant cm/sec
Co-6	$CoO-1MnO/Cr_2O_3$	none	1265	8.64×10^{5}	internal	6.3×10^{-3}	2.3×10^{-11}
Co-7	CoO (hp)$/Cr_2O_3$	Co-2	1526	1.59×10^{5}	internal	17.8×10^{-3}	7.0×10^{-10}
Co-8	$CoO-1MnO/Cr_2O_3$	none	1265	1.21×10^{6}	internal	7.7×10^{-3}	2.45×10^{-11}
Co-9	$CoO-1MnO/Cr_2O_3$	none	1187	4.84×10^{6}	internal	10.2×10^{-3}	1.1×10^{-11}
Co-10	$CoO-1MnO/Cr_2O_3$	Co-6	1492	8.63×10^{5}	internal	19.5×10^{-3}	1.97×10^{-10}
Co-11	$CoO-1MnO/Cr_2O_3$	Co-6	1370	8.76×10^{5}	internal	12.2×10^{-3}	6.2×10^{-11}
Co-12A	$CoO-1MnO/Cr_2O_3$	none	1235	9.54×10^{5}	internal	5.8×10^{-3}	1.76×10^{-11}
Co-12B	$CoO-1SiO_2/Cr_2O_3$	none	1235	9.54×10^{5}	internal	20.8×10^{-3}	2.3×10^{-10}
Co-13	$CoO-1MnO/Cr_2O_3$	none	1512	8.65×10^{4}	internal	7.08×10^{-3}	2.9×10^{-10}
Co-14	$CoO-1MnO/Cr_2O_3$	none	1512	8.65×10^{4}	internal	6.1×10^{-3}	2.15×10^{-10}
Co-15A	CoO (Single Crystal)$/Cr_2O_3$ (Single Crystal)	none	1410	7.55×10^{5}	internal	22×10^{-3}	3.34×10^{-10}
Co-15A	CoO (Single Crystal)$/Cr_2O_3$ (Single Crystal)	none	1410	7.55×10^{5}	interface displacement	4.7×10^{-3}	1.45×10^{-11}
Co-15B	CoO (Single Crystal)$/Cr_2O_3$	none	1410	7.55×10^{5}	internal	20.2×10^{-3}	2.7×10^{-10}
Co-16A	CoO (Single Crystal)$/Cr_2O_3$ (Single Crystal)	none	1250	1.7×10^{6}	internal	18.3×10^{-3}	9.8×10^{-11}

Expt. No.	Reactants	Previous Bond	Reaction Temperature ^{o}C	Reaction Time sec	Reaction Layer	Layer Thickness cm	Rate Constant cm/sec
Co-16A	CoO (Single Crystal)/Cr_2O_3 (Single Crystal)	none	1250	1.7×10^{6}	marker displacement	5.2×10^{-3}	7.9×10^{-12}
Co-16B	CoO (Single Crystal)/Cr_2O_3	none	1250	1.7×10^{6}	internal	15.2×10^{-3}	6.8×10^{-11}
C-17	CoO (hp)/Cr_2O_3	none	1250	1.7×10^{6}	internal	16.1×10^{-3}	7.6×10^{-11}
Co-18	CoO-1SiO_2/Cr_2O_3	none	1250	1.7×10^{6}	internal	28.6×10^{-3}	2.4×10^{-10}
Co-19	CoO-1SiO_2/Cr_2O_3	none	1512	1.6×10^{6}	internal	64.8×10^{-3}	8.5×10^{-9}
Co-20	CoO (hp)/Cr_2O_3	none	1370	4.94×10^{5}	internal	15.4×10^{-2}	2.4×10^{-10}

DISTRIBUTION LIST

CONTRACT NAS 3-11165 - STANFORD RESEARCH INSTITUTE

REPORT NO. NASA CR-72537

National Aeronautics and Space Administration		
Washington, D. C. 20546		
Attention:	N. F. Rekos (RAP)	1
	G. C. Deutsch (RRM)	1
	R. H. Raring (RRM)	1
Lewis Research Center		
National Aeronautics and Space Administration		
21000 Brookpark Road		
Cleveland, Ohio 44135		
Attention:	G. M. Ault, MS 105-1	1
	Technology Utilization Office, MS 3-19	1
	R. W. Hall, MS 105-1	1
	Library, MS 60-3	2
	Report Control Office, MS 5-5	1
	S. J. Grisaffe, MS 49-1	1
	Dr. H. B. Probst, MS 49-1	1
	N. T. Saunders, MS 105-1	1
	F. H. Harf, MS 106-1	3
	A. E. Anglin, MS 106-1	1
	C. E. Lowell, MS 49-1	3
	J. C. Freche, MS 49-1	1
	C. A. Barrett, MS 49-1	1
	G. J. Santoro, MS 49-1	1
Langley Research Center		
National Aeronautics and Space Administration		
Langley Station		
Hampton, Virginia 23365		
Attention:	Library	1
	Richard Pride, MS 188A	1
George C. Marshall Space Flight Center		
National Aeronautics and Space Administration		
Marshall Space Flight Center, Alabama 35812		
Attention:	Library	1
NASA Scientific and Technical Information Facility		
P. O. Box 3300		
College Park, Maryland 20740		
Attention:	NASA Representative, RQT-2448	6

Jet Propulsion Laboratory
4800 Oak Grove Drive
Pasadena, California 91103
Attention: Library 1

Ames Research Center
National Aeronautics and Space Administration
Moffett Field, California 94035
Attention: Library 1

Goddard Space Flight Center
National Aeronautics and Space Administration
Greenbelt, Maryland 20771
Attention: Library 1
D. F. Hasson, Code 714 1
C. E. Vest, Code 249.1 1

Manned Spacecraft Center
National Aeronautics and Space Administration
Houston, Texas 77058
Attention: Library 1
N. Chaffee, EB-4 1

Flight Research Center
National Aeronautics and Space Administration
P. O. Box 273
Edwards California 93523
Attention: Library 1

Federal Aviation Agency
800 Independence Avenue, SW
Washington, D. C. 20553
Attention: Brig. Gen. J. C. Maxwell 1
F. B. Howard, SS/210 1

Atomic Energy Commission
Washington, D. C. 20545
Attention: Technical Reports Library 1
Jules Simmons 1

Department of Air Force
Office of Scientific Research
Propulsion Research Division
Washington, D. C. 20525 1

Headquarters
Wright Patterson AFB, Ohio 45433
Attention: MAAM: Technical Library 1
AFSC-FTDS 1
AFML: Dr. A. M. Lovelace 1
SESOS: J. L. Wilkins 1
MAMP: I. Perlmutter 1

Department of the Navy
Office of Naval Research
Code 429
Washington, D. C. 20525
Attention: Dr. R. Roberts 1

Chief, Bureau of Naval Weapons
Department of the Navy
Washington, D. C. 20525
Attention: T. F. Kearns 1

U. S. Army Aviation Materials Laboratory
Fort Eustis, Virginia 23604
Attention: John White, Chief, SMOFE-APG 1

Army Materials Research Agency
Watertown Arsenal
Watertown, Massachusetts 02172
Attention: S. V. Arnold, Director 1

Aerojet-General Corporation
P. O. Box 296
Azusa, California
Attention: I. Petker, Dept. 5127, Bldg. 159 1

American Society for Metals
Metals Park
Novelty, Ohio 44073
Attention: Dr. Taylor Lyman 1

AVCO Lycoming Aircraft
550 South Main Street
Stratford, Connecticut 06497
Attention: W. R. Freeman, Jr. 1

Battelle Memorial Institute
505 King Avenue
Columbus, Ohio 43201
Attention: Defense Metals Information Center 1
Dr. A. Z. Hed 1
Dr. R. I. Jaffee 1
Dr. B. A. Wilcox

Bendix Corporation
Research Laboratories Division
Southfield, Michigan 48075
Attention: C. B. Sung 1

Boeing Company
P. O. Box 733
Renton, Washington 98055
Attention: W. E. Binz, SST Unit Chief 1

Clemson University
College of Engineering
Clemson, South Carolina 29631
Attention: Dr. J. S. Wolf 1

General Electric Company
Advanced Technology Laboratory
Schenectady, New York 12305
Attention: Library 1

General Electric Company
MPTL-AETD
Cincinnati, Ohio 45215
Attention: L. P. Jahnke 1
C. S. Wukusick 1

General Motors Corporation
Allison Division
Indianapolis, Indiana 46206
Attention: K. K. Hanink, Materials Laboratory 1

International Nickel Company
67 Wall Street
New York, New York 10005
Attention: R. R. Dewitt 1

International Nickel Company
P. D. Merica Research Laboratory
Sterling Forest
Suffern, New York 10901
Attention: Dr. F. Decker 1

Lockheed Palo Alto Research Laboratories
Materials and Science Laboratory 52-30
3251 Hanover Street
Palo Alto, California 94304
Attention: E. C. Burke 1

Michigan Technical University
Houghton, Michigan 49931
Attention: Prof. R. W. Guard 1

Ohio State University
Columbus, Ohio 43210
Attention: Dr. A. R. Rapp, Dept. of Metallurgical Engineering 1

Solar Division
International Harvester Corporation
San Diego, California 92112
Attention: J. V. Long, Director of Research 1

Tem-Pres Research, Inc.
1401 South Atherton Street
State College, Pennsylvania 16801 1

United Aircraft Corporation
400 Main Street
East Hartford, Connecticut 06108
Attention: E. F. Bradley, Chief, Materials Engineering 1